Cover Page

The handle http://hdl.handle.net/1887/49240 holds various files of this Leiden University dissertation

Author: Schwarz, Henriette
Title: Spinning worlds
Issue Date: 2017-06-01

Spinning Worlds

Roterende Werelden

Proefschrift

ter verkrijging van
de graad van Doctor aan de Universiteit Leiden,
op gezag van Rector Magnificus prof. mr. C.J.J.M. Stolker,
volgens besluit van het College voor Promoties
te verdedigen op donderdag 1 juni 2017
klokke 11:15 uur

door

Henriette Schwarz
geboren te Hørsholm, Denemarken
in 1986

Promotiecommissie

Promotor: Prof. dr. I. A. G. Snellen
Co-promotor: Dr. M. A. Kenworthy

Overige leden: Prof. dr. H. J. A. Röttgering
                        Prof. dr. C. Keller
                        Prof. dr. E. F. van Dishoeck
                        Dr. J-M. Désert   (University of Amsterdam)
                        Dr. J. L. Birkby   (Harvard University)

"Astronomers, like burglars and jazz musicians, operate best at night."
– Miles Kington

iv

Contents

1 | Introduction

"They say the sky is the limit, but to me, it is only the beginning. I look to the stars, and I count them, imagining every one of them as the centre of a solar system, even more wondrous than our own. We now know they are out there. Planets. Millions of them – just waiting to be discovered. What are they like, these distant spinning worlds? How did they come to be? And finally – before I close my eyes and go to sleep, one question lingers. Like the echo of a whisper : Is anyone out there..."

The study of exoplanets is a quest to understand our place in the universe. How unique is the solar system? How extraordinary is the Earth? Is life on Earth an unfathomable coincidence, or is the galaxy teeming with life? Only 25 years ago the first extrasolar planets were discovered, two of them, orbiting the millisecond pulsar PSR1257+12 (Wolszczan and Frail, 1992), and this was followed three years later by the discovery of the first exoplanet orbiting a solar-type star (51 Pegasi, Mayor and Queloz, 1995). In the subsequent years, multiple techniques were developed to find and study these new worlds. Each detection method has its own advantages, limitations and biases, and they have complimented each other to form the picture of exoplanets that we have today: The galaxy is brimming with planetary systems, and the exoplanets are more diverse, than we could ever have imagined.

The diversity of planets presents a challenge to the theories of formation designed to match the solar system, and any modern theories must strive to explain the full observed range of architectures of planetary systems. In fact, understanding the formation and evolution of planetary systems and exploring their full diversity and complexity is one of the central themes of contemporary astrophysics today. Ultimately, we wish to answer fundamental existential questions about the possible occurrence of extraterrestrial life. The search for life outside the solar system may commence less than a decade from now by searching for atmospheric gases in chemical disequilibrium such as molecular oxygen in the atmosphere of the Earth.

1.1   Star and planet formation

Stars form through the gravitational collapse of prestellar cloud cores, which are gravitationally bound, dense regions within a larger molecular cloud. The continued infall of mass from the outer layers cause the core to become opaque, and the temperature to increase (Larson, 1969; Boss and Yorke, 1995). When the temperature in the core reaches 2000 K, molecular hydrogen is dissociated and hydrogen and helium atoms are ionized, absorbing energy, and allowing the core to contract and accrete further to form a protostar surrounded by an envelope. Due to rotation, a centrifugally supported disk will form (Terebey et al., 1984), and accretion onto the newly formed protostar is mostly continued through this circumstellar disk. At the moment that the accretion stops, the star is considered a pre-main-sequence (PMS) star which is powered by the energy from the gravitational collapse. Hydrogen fusion will occur when the core temperature in the PMS star is high enough, thus entering the star into its main sequence life time.

It is expected that during the phase that the protostar harbours a circumstellar disk (also called a protoplanetary disk) not all material accretes onto the star, but instead forms planets. This is a complex process which is yet far from fully understood. Since this thesis deals with giant gaseous planets, I will focus here on outlining current views on particularly their formation.

The currently favoured theory for giant planet formation is core accretion (Fig. 1.1A, Pollack et al., 1996; Laughlin et al., 2004; Hubickyj et al., 2005). This is an accumulative process taking place within the protoplanetary disk, from dust and grains which coagulate into larger particles, settling towards the disk midplane eventually forming kilometer sized planetesimals which grow to planetary embryos through collisions, rapidly growing to a protoplanet. Once the planetary core grows large enough, it attracts a gas envelope, slowly at first, however as the total mass exceeds the point where the gravitational force is balanced by the pressure gradient, runaway accretion will take place. Eventually the accretion rate will decrease as the surrounding gas is depleted. Core accretion is expected to be most effective beyond the ice line, between 5 and 10 au. The existence of hot Jupiters with periods on the order of days, are explained with either type II migration within the disk, or as dynamical scattering through gravitational interactions with additional bodies (Chambers, 2007). However, it has also been suggested that hot Jupiters may form by core accretion in situ, initiated by the presence of super Earths (Batygin et al., 2016). Planets can also be scattered in the outward direction, and this is a possible explanation for the existence of the extremely wide-orbit companions which have been discovered with direct imaging techniques.

The major contesting theory for giant planet formation is the disk gravitational

(A) Core Accretion

(B) Disk Instability

(C) Prestellar Core Fragmentation
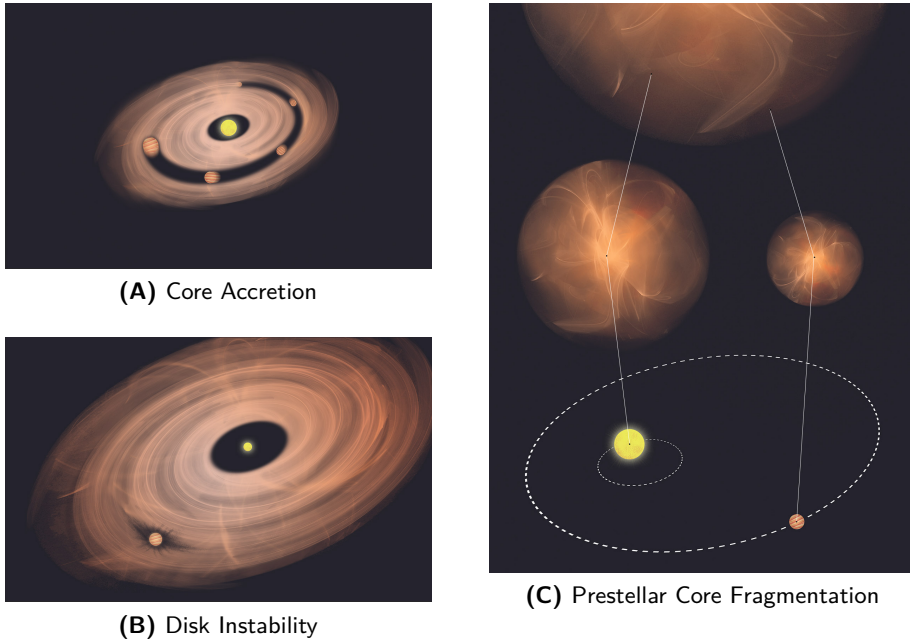
Figure 1.1: The two most common formation theories for giant planets are (A) core accretion, and (B) disk instability. In the core accretion model, the planet agglomerates from dust, typically at a distance of 5-10 au, and once the planetary core grows large enough it attracts a gas envelope. The planet may subsequently migrate inwards through type II migration or be scattered in either direction. In the disk instability model, a clump of gas collapses in the outer part ($> 40\,\mathrm{au}$) of a massive circumstellar disk. A third option, (C) prestellar core fragmentation, is considered for wide-orbit giant planets and brown dwarf companions. This model considers gravitational instabilities that takes place at a much earlier stage of the star's evolution, and it is equivalent to how binary star systems are formed. *Image credit: Rafa Monterde Alonso.*

instability model (Fig. 1.1B, Boss, 1997, 2000), which states that gas giants might form from a gravitational collapse within the protoplanetary disk. Gravitational instabilities lead to fragmentation of the gas into self-gravitating clumps. The majority of the mass is accumulated on a much shorter timescale compared to core accretion, and only later will a core form through sedimentation. The exact conditions for gravitational instabilities to occur are debated, but disks with large masses, low temperatures and high densities are favoured. Furthermore, disk instabilities are only expected to take place in the outer parts of a disk, at several tens to hundreds of au, because the radiative cooling rates there are higher (Cai et al., 2006; Rafikov, 2007).

In the case of wide-orbit giant planets and brown dwarf companions there is a third formation pathway which may play a significant role (Fig. 1.1C). During the earliest stages of the prestellar cloud collapse, the prestellar core can fragment due to global non-linear gravitational instabilities(Chabrier et al., 2014). This is how binary stars are expected to form, and it is possible that that the same process can produce an object pair with an extreme mass ratio (Jumper and Fisher, 2013), forming a system with a central star and a wide-orbit giant planet. This theory is supported by the existence of substellar companions with large projected separations in the range 500 au to 3500 au and masses down to $5\,M_J$ (Aller et al., 2013). The scale of these systems is much larger than that of protoplanetary disks, but is a good match to prestellar core envelopes.

The three formation pathways described here have one thing in common. They all struggle to explain the whole observed spectrum of giant planets. Therefore it is a distinct possibility that all of them can take place, depending on the conditions of the forming star system. While core accretion is expected to operate most efficiently relatively close to the star, disk instabilities is only expected to take place in the outer regions of the protoplanetary disk, and prestellar core fragmentation may explain some of the widest orbiting companions, although it may also be possible to form tight binaries during the prestellar core collapse (Bonnell and Bate, 1994). This opens up the idea that the orbital distance of an exoplanet can be used as an indicator for how the planet was formed. However, this will need to be treated in a statistical sense, since migration and dynamical scattering complicates the situation, with planets potentially having formed in a very different orbit than the one where they are presently observed (Vorobyov, 2013).

In this thesis we focus on a new observable, the rotational velocity, which may shed some light on the formation of giant planets, as well as brown dwarf companions. The spin angular momentum of an exoplanet is accreted together with the mass, during the formation. Therefore it is conceiveable that the initial spin angular momentum content is strongly related to how the planet formed, and that

for example core accretion and disk instability with their different time scales and favoured locations within the disk, will result in observable differences in the spin rate. It is important to realise that the spin will evolve, and that the evolution is mass dependent. It will be necessary to fully understand this evolution if we are to use measurements of the rotational velocity, or alternatively the rotation period, to probe the formation of exoplanets.

1.2   Finding exoplanets

Finding extrasolar planets is extremely challenging. For a distant observer, the reflection of the Earth only adds up to less than 1 part-per-billion of the light from the Sun. Fortunately, there are several methods to indirectly infer the presence of extrasolar planets. The radial velocity method, astrometry, and pulsar timing all make use of the orbital motion of the host star around the center-of-mass of the extrasolar planetary system – without directly seeing the planet. In particular the radial velocity method has been extremely successful with more than a thousand detections to date, providing the main orbital parameters and a lower limit to the planetary mass. Also the transit method has been a flourishing success, not least due to the Kepler mission, which has discovered more than 2300 confirmed exoplanets[1]. The transit method relies on near-perfect alignment of the orbit with the line of sight, so that the planet transits in front of the star, causing periodic dips in the light curve. This provides a measure of the planetary radius, and combined with the radial velocity method, this in turn gives an estimate of the mean density of the planet, constraining its bulk composition. While the radial velocity and transit methods are strongly biased towards planets on close-in orbits, astrometry, which measures the on-sky displacement of the host star, will excell at detecting long-period planets, and it will be more sensitive to planets with an orbital plane which is viewed face-on. Although no exoplanets have been discovered as of yet by astrometry, the ESA GAIA mission is expected to find thousands of exoplanets unlocking a whole new area of orbital parameter space (Perryman et al., 2014). The existence of an extrasolar planet can also be inferred from microlensing through which distant background stars are lensed by foreground planetary systems. Although this has resulted in the detection of a few dozen planets, their properties can only be inferred in a statistical sense.

Direct detection of exoplanets by high contrast imaging is still very challenging, but great progress is being made. So far it is restricted to young massive planets which are still hot from their formation, of which about two-dozen are known. These observations provide a direct measure of the flux from the planet, thereby

---

[1]http://exoplanetarchive.ipac.caltech.edu/

immediately probing the planetary atmosphere. Since the achieved contrasts near the host star are still limited, most planets discovered are located at projected separations of tens to hundreds of au. The theoretical observational limits are a stong function of telescope size, and the future holds great promise with the European Extremely Large Telescope (E-ELT). The E-ELT and other extremely large telescopes are expected to open up the parameter space to include signifantly cooler and older planets - even mature planetary systems around the nearest stars.

The combination of all these techniques, each with their own specific biases, have provided a first view of the planet population (Fig. 1.2). It has revealed that planets are very common. More than 10% of the solar type stars have gas giant planets of Jupiter mass, ~30% have super-Earth to Neptune-size planets (Mayor et al., 2011), with the occurrence rate increasing for smaller radii (Howard et al., 2012). An extrapolation to Earth-mass planets is speculative at best, but it is likely that most stars harbour Earth-mass planets. While the solar system planets already exhibit an enormous diversity, this is extended even further in the exoplanet population. New classes of planets, such as hot Jupiters, super-Earths and massive gas giants on wide orbits, are all common but not found in the solar system. Discoveries are being pushed to smaller and more temperate planets, both using the transit and radial velocity method. The most exciting recent example has been the discovery of a terrestrial planet in the habitable zone of our nearest neighbour Proxima Centauri (Anglada-Escudé et al., 2016).

1.3 Atmospheric characterisation

Detection is only the first step in understanding the physical properties of an exoplanet. The characterisation of its atmosphere is an important next step. It can reveal the chemical composition of the atmosphere, its reflective properties, the presence of condensates, its temperature structure, and possible rotation and global circulation. Those may be linked to the formation and evolutionary history of the planet, and are needed to understand its global climate. Also the information on the atmosphere may shed light on the bulk composition of the planet, which in the case of only mass-radius information may result in persistent degeneracies. Ultimately, we want to find evidence for biological activity through the detection and identification of biomarker gases that are out of chemical equilibrium – such as molecular oxygen in the atmosphere of Earth. To reach this exciting goal a deep understanding of the possibly wide range of planet families, their atmospheric processes and evolutionary histories is required.

The planet detection methods are mostly indirect, meaning that no flux from the planet is identified. For atmospheric characterisation it is necessary to separate
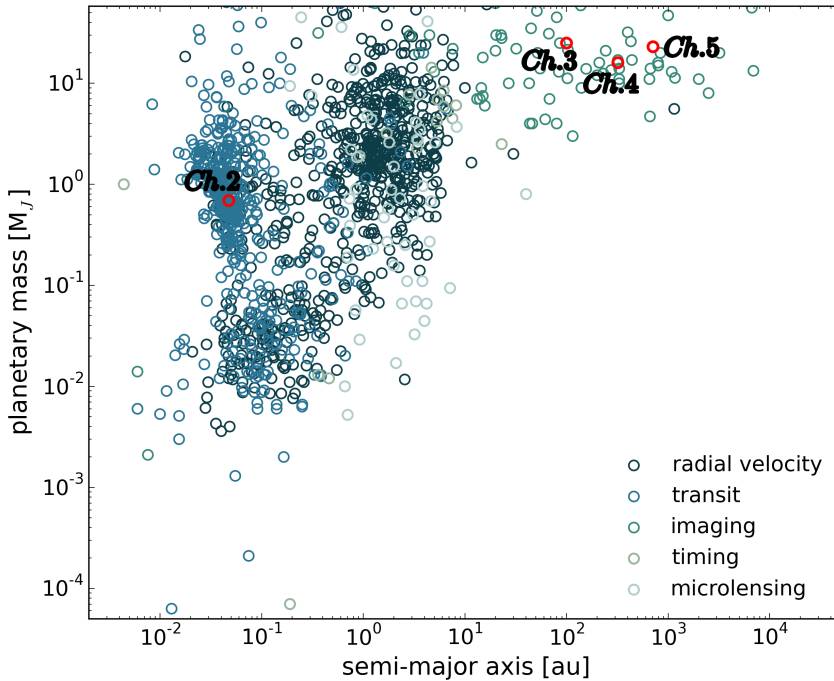
Figure 1.2: The exoplanet.eu catalog as of December 2016. The planets (or brown dwarf companions) which are featured in this thesis are marked with their respective chapters. One is the hot Jupiter HD 209458 b (Chapter 2), and the three others are dircly imaged substellar companions, GQ Lupi b (Chapter 3), GSC 6214-210 b (Chapter 4), and HIP 789530 b (Chapter 5).

the planet light from that of the star. This can be done in several ways. Most successful so far have been atmospheric observations of transiting planets for which time differential measurements are made, including transits, eclipses and phase curves. In addition, planet light can be angularly separated like in the case of direct imaging. As used in this thesis, these methods can be combined with high-dispersion spectroscopy to further separate the planet light from that of the star and, since these are ground-based obervations, the telluric contamination.

1.3.1 Transits, eclipses, and phase curves

Transiting planets offer unique opportunities for atmospheric characterisation. When the planet passes in front of the star, as seen from Earth, starlight filters through the planetary atmosphere. When observed at different wavelengths, this manifests itself as a wavenlength dependent radius, because more or less star light is absorbed
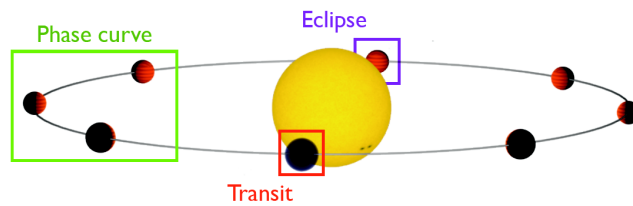
Figure 1.3: Transiting exoplanets provide three distinct methods for characterising the atmosphere of the planet. *Image credit: Ernst de Mooij*

by the planet atmosphere. This is called transmission spectroscopy. These measurements have been very successful from space using the Hubble Space Telescope and Spitzer Space Telescope, resulting in the detection of atomic and molecular gases in the atmosphere and exospheres of hot Jupiters (Charbonneau et al., 2002; Vidal-Madjar et al., 2004), and high-altitude hazes through Rayleigh scattering (Pont et al., 2013). There is also compelling evidence for the existence of high-altitude clouds in some Super-Earths and Neptune-size exoplanets (Kreidberg et al., 2014; Knutson et al., 2014b,a).

Half an orbit later, the planet is eclipsed by its star, offering a moment in time when the observed flux only belongs to the star. This can be subtracted from the observations immediately before or after the eclipse when the day-side of the planet is fully visible, thus revealing the portion of the flux, which belongs to the planet (Deming et al. 2004; Charbonneau et al. 2004). A rough spectrum can be constructed from the broadband measurements of the secondary eclipse depth as function of wavelength, revealing its thermal spectrum and/or reflected spectrum. In addition, molecular features can constrain the temperature structure of the planet.

By monitoring the flux from the planet+star system as function of orbital phase, the varying contribution from the planet's day and night side can be assessed (Knutson et al. 2007), revealing a one-dimensional temperature map of the planet. This can constrain the global circulation patterns of the planet and its overall climate. In the case of optical phase curve observations the planet albedo is being probed.

1.3.2 High-contrast imaging

High-contrast imaging provides a direct way of probing the atmosphere of a planet. The best results are being reached with ground-based telescopes using adaptive optics systems aimed to cancel out seeing effects, and coronography to optimally darken regions directly around the star. Also, smart analysis algorithms are being

used to further remove systematics originating from the telescope.

High-contrast imaging immediately allows the planet thermal spectrum to be constructed by combining measurements at different wavelengths (Lagrange et al., 2010). The planet must be located at large enough orbital distance they it can be angularly separated from the host star, typically tens or hundreds of au. This means the irradiation from the host star is negligible, and mature planets at such orbital distances are too faint, and out of reach of the current telescope systems. On the other hand, the very young planets can be observed (Marois et al., 2008; Lagrange et al., 2010), because they are still hot from their formation, resulting in a much more favourable planet-to-star contrast. This provides a unique opportunity to study exoplanets in their infancy.

1.4   High-dispersion spectroscopy

Ground-based high-dispsersion spectroscopy in the near-infrared has proven to be an effective method to probe both transiting hot Jupiters as well as young directly imaged gas giants. With a sufficiently high spectral resolution the molecular features are resolved into individual lines, allowing a reliable identification of the molecules through line matching with template spectra (Brown et al., 2002; Deming et al., 2005; Barnes et al., 2007). Our team has successfully employed two different strategies for isolating a planetary signal from its host star, using the Cryogenic Infra-Red Echelle Spectrograph (CRIRES; Kaeufl et al., 2004) at the Very Large Telescope (VLT). The first is time-differential observations which has been applied to hot Jupiters (Snellen et al., 2010), and the second is a combination with high contrast imaging, targeting the spatially separated gas giants, discovered with direct imaging(Snellen et al., 2014).

1.4.1   High-dispersion spectroscopy for time-differential observations

CRIRES has a spectral resolving power $\lambda/\Delta\lambda \simeq 100\,000$, which is sufficient that molecular bands, such as the ro-vibrational (2,0) R-branch of carbon monoxide (CO), are resolved into tens or hundreds of individual lines. This means the observations become sensitive to Doppler effects related to the orbital velocity of the planet. In the case of hot Jupiters the orbital velocity can be up to $150\,\mathrm{km\,s^{-1}}$, so within a few hours of observations the radial component can change up to tens of $\mathrm{km\,s^{-1}}$ corresponding to tens of pixels in the observed spectrum. This allows the shifting planet spectrum to be effectively filtered out from the quasi-stationary stellar and telluric spectral features. This method can be applied to any system in

which the planet velocity is expected to vary, including transit and dayside measurement, for which the latter can also be applied to non-transiting systems (Brogi et al., 2012).

CRIRES hot Jupiter survey

Snellen et al. (2010) was the first to successfully implement the high-dispersion time-differential strategy to detect CO at 2.3 μm in the transmission spectrum of the hot Jupiter HD 209458 b. This was followed by a large CRIRES survey targeting five of the brightest hot Jupiters, two of them transiting and three of them non-transiting. Table 1 summarises the published results from high-dispersion infrared spectroscopy of hot Jupiters both from the survey by our team and from other teams. The observations are a mix of transmission spectroscopy and dayside spectroscopy, and they have provided robust detections of CO and/or H_2O in the atmospheres of the targeted hot Jupiters, along with constraints on their abundances. For the three non-transiting planets, 51 Pegasi b, HD 179949 b and τ Boötis b, the absolute masses and inclinations have been measured (Brogi et al., 2012, 2013, 2014; Rodler et al., 2012; Lockwood et al., 2014), a feat which has so far only been achieved with this method. While transmission spectroscopy will always result in molecular *absorption*, dayside spectroscopy is sensitive to the temperature-pressure (T/p) profile, because the line-of-sight is near-aligned with the vertical direction in the planetary atmosphere. The T/p profile affects the average shape of the absorption lines in the dayside spectrum, with the most extreme example being a temperature inversion layer in the atmosphere which would result in emission lines rather than absorption lines in the dayside spectrum. However at the current time, only absorption has been detected (See Chapter 2). Also planet rotation can affect the shape of the spectral lines, and atmospheric circulation can cause an additional Doppler shift. Brogi et al. (2016) constrained the average line shape of CO and H_2O absorption lines in the transmission spectrum of HD 189733 b, and found their measurements to be consistent with synchronous rotation, which is the expectation for a hot Jupiter, and a small day- to nightside wind peed of $-1.7\,\mathrm{km\,s^{-1}}$.

1.4.2 High-dispersion spectroscopy + high-contrast imaging

High-dispersion spectroscopy can also be combined with high contrast imaging (HDS+HCI). While the planet-star contrast obtained with HCI may not be sufficient to detect the planet, the remaining starlight at the planet position may have a significantly different spectrum than that of the planet. The stellar spectrum is well sampled and can be filtered out, leaving only the planet signal at the planet

Table 1.1: Summary of hot Jupiters observed with high-dispersion spectroscopy

Planet	Method	Wavelength	Molecule	Reference	Note
Transiting planets					
HD 209458 b	Transmission	2.3 μm	CO	Snellen et al. (2010)	Pilot study
	Dayside	2.3 μm	(CO)	Schwarz et al. (2015)	Chapter 2
HD 189733 b	Transmission	2.3 μm	$CO+H_2O$	Brogi et al. (2016)	
	Dayside	2.3 μm	CO	de Kok et al. (2013)	
	Dayside	3.2 μm	H_2O	Birkby et al. (2013)	
Non-transiting planets					
51 Pegasi b	Dayside	2.3 μm	$CO+H_2O$	Brogi et al. (2013)	
HD 179949 b	Dayside	2.3 μm	$CO+H_2O$	Brogi et al. (2014)	
τ Boötis b	Dayside	2.3 μm	CO	Brogi et al. (2012)	
	Dayside	2.3 μm	CO	Rodler et al. (2012)	diff. team, CRIRES
	Dayside	3.2 μm	H_2O	Lockwood et al. (2014)	diff. team, NIRSPEC

 Unless stated otherwise in the notes, the observations listed here are part of a CRIRES survey conducted by our team. The dayside detection of CO in the atmosphere of HD 209458 b is only tentative, and is therefore in a paranthesis.

position, and the signal of the individual spectral lines can be combined again by using cross-correlation techniques (Sparks and Ford, 2002; Riaud and Schneider, 2007; Snellen et al., 2015). In this way the spin-rotation of the directly imaged planet β Pictoris b was determined for the first time (Snellen et al., 2014).

1.5   This thesis

In this thesis I characterise giant exoplanets using ground-based high-dispersion spectroscopy, both targeting young directly imaged gas giants and a transiting hot Jupiter. This involved the two observational techniques as described above, time differential spectroscopy and a combination of spectroscopy and high-contrast imaging. Chapter 2 describes CRIRES observations of the famous hot Jupiter HD 209458 b, constraining its atmospheric vertical temperature structure. Chapters 3, 4, and 5 present the first mini-survey of planetary spin measurements.

1.5.1   Chapter 2 - Evidence against a thermal inversion in a hot Jupiter

The vertical temperature structure is one of the prime objectives in the atmospheric characterisation of an exoplanet. There have been claims of temperature inversion layers in a selection of strongly irradiated hot Jupiters, but the claims have been based on broadband secondary-eclipse measurements which suffer from degeneracies between the molecular abundances and the temperature structure. On the other hand, high dispersion spectroscopy has the potential to unambiguously detect the presence of a temperature inversion layer. If molecular emission lines are identified in the spectrum, this can only be explained by the presence of a thermal inversion.

In Chapter 2, we present the results from high-dispersion near infrared spectroscopic observations of the dayside of HD 209458 b. This was one of the objects in the hot Jupiter CRIRES survey described in Section 1.4.1. This exoplanet was long considered the gold standard for a hot Jupiter with a thermal inversion, however, we found evidence against a strong thermal inversion. Although CO is known from transmission spectroscopy to be present in the atmosphere of HD 209458 b, in the dayside spectrum, we saw only a hint of an *absorption* signal from CO. This is best explained by a near-isothermal pressure profile.

1.5.2   Chapters 3, 4 & 5 - first survey of planetary spin

The rotational velocities of exoplanets and brown dwarf companions are fundamental observables which affect their climate, atmospheric dynamics, and mag-

netic fields, and may hold important clues to the formation process and the orbital history of these objects. We have measured the projected rotational velocity of three young substellar companions, GQ Lupi b (Chapter 3), GSC 6214-210 b (Chapter 4), and HIP 78530 b (Chapter 5), showing $v \sin(i)$ of $5.3^{+0.9}_{-1.0}$ km s^{-1}, 21.5 ± 3.5 km s^{-1}, and $12.0^{+2.0}_{-1.5}$ km s^{-1}, respectively. Combining this small sample with the previously observed objects Beta Pictoris b (Snellen et al., 2014) and 2M1207 b (Zhou et al., 2016), I made a first attempt to conduct comparative planetology with the spin as the focus. A correlation is seen of spin velocity with age, which we interpret as due to the youngest objects still accreting angular momentum and their spin-up through subsequent cooling and contraction.
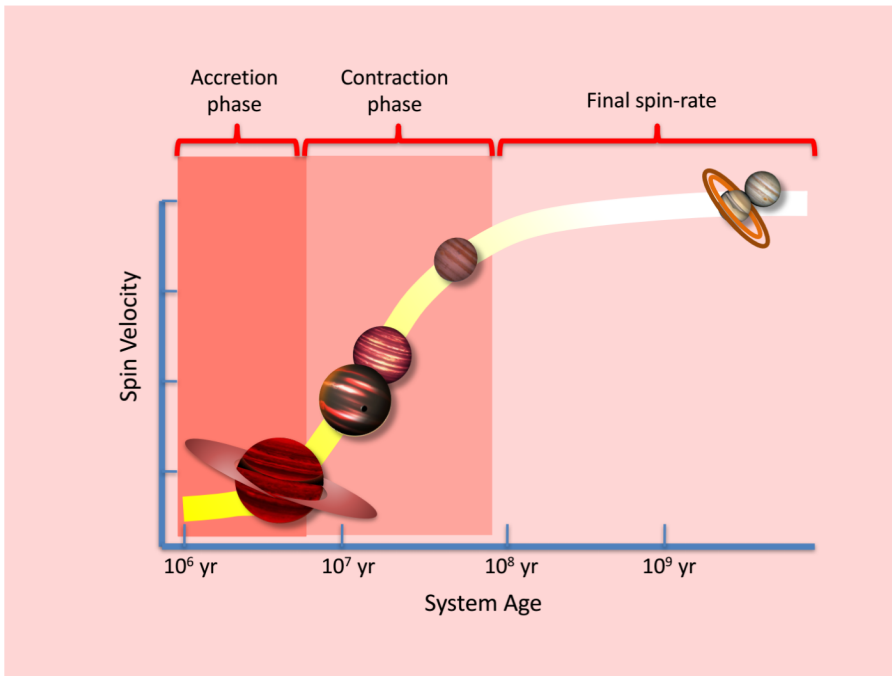
Figure 1.4: Graphical illustration of the proposed spin and angular momentum evolution of gas giant planets (Chapters 3, 4, and 5).

References

Aller, K. M., A. L. Kraus, M. C. Liu, W. S. Burgett, K. C. Chambers, K. W. Hodapp, N. Kaiser, E. A. Magnier, and P. A. Price
2013. A Pan-STARRS + UKIDSS Search for Young, Wide Planetary-mass Companions in Upper Scorpius. *ApJ*, 773:63.

Anglada-Escudé, G., P. J. Amado, J. Barnes, Z. M. Berdiñas, R. P. Butler, G. A. L. Coleman, I. de La Cueva, S. Dreizler, M. Endl, B. Giesers, S. V. Jeffers, J. S. Jenkins, H. R. A. Jones, M. Kiraga, M. Kürster, M. J. López-González, C. J. Marvin, N. Morales, J. Morin, R. P. Nelson, J. L. Ortiz, A. Ofir, S.-J. Paardekooper, A. Reiners, E. Rodríguez, C. Rodríguez-López, L. F. Sarmiento, J. P. Strachan, Y. Tsapras, M. Tuomi, and M. Zechmeister
2016. A terrestrial planet candidate in a temperate orbit around Proxima Centauri. *Nature*, 536:437–440.

Barnes, J. R., T. S. Barman, L. Prato, D. Segransan, H. R. A. Jones, C. J. Leigh, A. Collier Cameron, and D. J. Pinfield
2007. Limits on the 2.2-μm contrast ratio of the close-orbiting planet HD 189733b. *MNRAS*, 382:473–480.

Batygin, K., P. H. Bodenheimer, and G. P. Laughlin
2016. In Situ Formation and Dynamical Evolution of Hot Jupiter Systems. *ApJ*, 829:114.

Birkby, J. L., R. J. de Kok, M. Brogi, E. J. W. de Mooij, H. Schwarz, S. Albrecht, and I. A. G. Snellen
2013. Detection of water absorption in the day side atmosphere of HD 189733 b using ground-based high-resolution spectroscopy at 3.2 μm. *MNRAS*, 436:L35–L39.

Bonnell, I. A. and M. R. Bate
1994. The Formation of Close Binary Systems. *MNRAS*, 271.

Boss, A. P.
1997. Giant planet formation by gravitational instability. *Science*, 276:1836–1839.

Boss, A. P.
2000. Possible Rapid Gas Giant Planet Formation in the Solar Nebula and Other Protoplanetary Disks. *ApJ*, 536:L101–L104.

Boss, A. P. and H. W. Yorke
  1995. Spectral energy of first protostellar cores: Detecting 'class -I' protostars with ISO and SIRTF. *ApJ*, 439:L55–L58.

Brogi, M., R. J. de Kok, S. Albrecht, I. A. G. Snellen, J. L. Birkby, and H. Schwarz
  2016. Rotation and Winds of Exoplanet HD 189733 b Measured with High-dispersion Transmission Spectroscopy. *ApJ*, 817:106.

Brogi, M., R. J. de Kok, J. L. Birkby, H. Schwarz, and I. A. G. Snellen
  2014. Carbon monoxide and water vapor in the atmosphere of the non-transiting exoplanet HD 179949 b. *A&A*, 565:A124.

Brogi, M., I. A. G. Snellen, R. J. de Kok, S. Albrecht, J. Birkby, and E. J. W. de Mooij
  2012. The signature of orbital motion from the dayside of the planet τ Boötis b. *Nature*, 486:502–504.

Brogi, M., I. A. G. Snellen, R. J. de Kok, S. Albrecht, J. L. Birkby, and E. J. W. de Mooij
  2013. Detection of Molecular Absorption in the Dayside of Exoplanet 51 Pegasi b? *ApJ*, 767:27.

Brown, T. M., K. G. Libbrecht, and D. Charbonneau
  2002. A Search for CO Absorption in the Transmission Spectrum of HD 209458b. *PASP*, 114:826–832.

Cai, K., R. H. Durisen, S. Michael, A. C. Boley, A. C. Mejía, M. K. Pickett, and P. D'Alessio
  2006. The Effects of Metallicity and Grain Size on Gravitational Instabilities in Protoplanetary Disks. *ApJ*, 636:L149–L152.

Chabrier, G., A. Johansen, M. Janson, and R. Rafikov
  2014. Giant Planet and Brown Dwarf Formation. *Protostars and Planets VI*, Pp. 619–642.

Chambers, J.
  2007. Planet Formation with Type I and Type II Migration. In *AAS/Division of Dynamical Astronomy Meeting #38*, volume 38 of *AAS/Division of Dynamical Astronomy Meeting*, P. 6.04.

Charbonneau, D., T. M. Brown, R. W. Noyes, and R. L. Gilliland
  2002. Detection of an Extrasolar Planet Atmosphere. *ApJ*, 568:377–384.

de Kok, R. J., M. Brogi, I. A. G. Snellen, J. Birkby, S. Albrecht, and E. J. W. de Mooij
2013. Detection of carbon monoxide in the high-resolution day-side spectrum of the exoplanet HD 189733b. *A&A*, 554:A82.

Deming, D., T. M. Brown, D. Charbonneau, J. Harrington, and L. J. Richardson
2005. A New Search for Carbon Monoxide Absorption in the Transmission Spectrum of the Extrasolar Planet HD 209458b. *ApJ*, 622:1149–1159.

Howard, A. W., G. W. Marcy, S. T. Bryson, J. M. Jenkins, J. F. Rowe, N. M. Batalha, W. J. Borucki, D. G. Koch, E. W. Dunham, T. N. Gautier, III, J. Van Cleve, W. D. Cochran, D. W. Latham, J. J. Lissauer, G. Torres, T. M. Brown, R. L. Gilliland, L. A. Buchhave, D. A. Caldwell, J. Christensen-Dalsgaard, D. Ciardi, F. Fressin, M. R. Haas, S. B. Howell, H. Kjeldsen, S. Seager, L. Rogers, D. D. Sasselov, J. H. Steffen, G. S. Basri, D. Charbonneau, J. Christiansen, B. Clarke, A. Dupree, D. C. Fabrycky, D. A. Fischer, E. B. Ford, J. J. Fortney, J. Tarter, F. R. Girouard, M. J. Holman, J. A. Johnson, T. C. Klaus, P. Machalek, A. V. Moorhead, R. C. Morehead, D. Ragozzine, P. Tenenbaum, J. D. Twicken, S. N. Quinn, H. Isaacson, A. Shporer, P. W. Lucas, L. M. Walkowicz, W. F. Welsh, A. Boss, E. Devore, A. Gould, J. C. Smith, R. L. Morris, A. Prsa, T. D. Morton, M. Still, S. E. Thompson, F. Mullally, M. Endl, and P. J. MacQueen
2012. Planet Occurrence within 0.25 AU of Solar-type Stars from Kepler. *ApJS*, 201:15.

Hubickyj, O., P. Bodenheimer, and J. J. Lissauer
2005. Accretion of the gaseous envelope of Jupiter around a 5 10 Earth-mass core. *Icarus*, 179:415–431.

Jumper, P. H. and R. T. Fisher
2013. Shaping the Brown Dwarf Desert: Predicting the Primordial Brown Dwarf Binary Distributions from Turbulent Fragmentation. *ApJ*, 769:9.

Kaeufl, H.-U., P. Ballester, P. Biereichel, B. Delabre, R. Donaldson, R. Dorn, E. Fedrigo, G. Finger, G. Fischer, F. Franza, D. Gojak, G. Huster, Y. Jung, J.-L. Lizon, L. Mehrgan, M. Meyer, A. Moorwood, J.-F. Pirard, J. Paufique, E. Pozna, R. Siebenmorgen, A. Silber, J. Stegmeier, and S. Wegerer
2004. CRIRES: a high-resolution infrared spectrograph for ESO's VLT. In *Ground-based Instrumentation for Astronomy*, A. F. M. Moorwood and M. Iye, eds., volume 5492 of *Proc. SPIE*, Pp. 1218–1227.

Knutson, H. A., B. Benneke, D. Deming, and D. Homeier
2014a. A featureless transmission spectrum for the Neptune-mass exoplanet GJ436b. *Nature*, 505:66–68.

Knutson, H. A., D. Dragomir, L. Kreidberg, E. M.-R. Kempton, P. R. McCullough, J. J. Fortney, J. L. Bean, M. Gillon, D. Homeier, and A. W. Howard
2014b. Hubble Space Telescope Near-IR Transmission Spectroscopy of the Super-Earth HD 97658b. *ApJ*, 794:155.

Kreidberg, L., J. L. Bean, J.-M. Désert, B. Benneke, D. Deming, K. B. Stevenson, S. Seager, Z. Berta-Thompson, A. Seifahrt, and D. Homeier
2014. Clouds in the atmosphere of the super-Earth exoplanet GJ1214b. *Nature*, 505:69–72.

Lagrange, A.-M., M. Bonnefoy, G. Chauvin, D. Apai, D. Ehrenreich, A. Boccaletti, D. Gratadour, D. Rouan, D. Mouillet, S. Lacour, and M. Kasper
2010. A Giant Planet Imaged in the Disk of the Young Star β Pictoris. *Science*, 329:57.

Larson, R. B.
1969. Numerical calculations of the dynamics of collapsing proto-star. *MNRAS*, 145:271.

Laughlin, G., P. Bodenheimer, and F. C. Adams
2004. The Core Accretion Model Predicts Few Jovian-Mass Planets Orbiting Red Dwarfs. *ApJ*, 612:L73–L76.

Lockwood, A. C., J. A. Johnson, C. F. Bender, J. S. Carr, T. Barman, A. J. W. Richert, and G. A. Blake
2014. Near-IR Direct Detection of Water Vapor in Tau Boötis b. *ApJ*, 783:L29.

Marois, C., B. Macintosh, T. Barman, B. Zuckerman, I. Song, J. Patience, D. Lafrenière, and R. Doyon
2008. Direct Imaging of Multiple Planets Orbiting the Star HR 8799. *Science*, 322:1348.

Mayor, M., M. Marmier, C. Lovis, S. Udry, D. Ségransan, F. Pepe, W. Benz, J. . Bertaux, F. Bouchy, X. Dumusque, G. Lo Curto, C. Mordasini, D. Queloz, and N. C. Santos
2011. The HARPS search for southern extra-solar planets XXXIV. Occurrence, mass distribution and orbital properties of super-Earths and Neptune-mass planets. *ArXiv e-prints*.

Mayor, M. and D. Queloz
  1995. A Jupiter-mass companion to a solar-type star. *Nature*, 378:355–359.

Perryman, M., J. Hartman, G. Á. Bakos, and L. Lindegren
  2014. Astrometric Exoplanet Detection with Gaia. *ApJ*, 797:14.

Pollack, J. B., O. Hubickyj, P. Bodenheimer, J. J. Lissauer, M. Podolak, and
  Y. Greenzweig
  1996. Formation of the Giant Planets by Concurrent Accretion of Solids and
  Gas. *Icarus*, 124:62–85.

Pont, F., D. K. Sing, N. P. Gibson, S. Aigrain, G. Henry, and N. Husnoo
  2013. The prevalence of dust on the exoplanet HD 189733b from Hubble and
  Spitzer observations. *MNRAS*, 432:2917–2944.

Rafikov, R. R.
  2007. Convective Cooling and Fragmentation of Gravitationally Unstable
  Disks. *ApJ*, 662:642–650.

Riaud, P. and J. Schneider
  2007. Improving Earth-like planets' detection with an ELT: the differential
  radial velocity experiment. *A&A*, 469:355–361.

Rodler, F., M. Lopez-Morales, and I. Ribas
  2012. Weighing the Non-transiting Hot Jupiter τ Boo b. *ApJ*, 753:L25.

Schwarz, H., M. Brogi, R. de Kok, J. Birkby, and I. Snellen
  2015. Evidence against a strong thermal inversion in HD 209458b from high-
  dispersion spectroscopy. *A&A*, 576:A111.

Snellen, I., R. de Kok, J. L. Birkby, B. Brandl, M. Brogi, C. Keller, M. Kenworthy,
  H. Schwarz, and R. Stuik
  2015. Combining high-dispersion spectroscopy with high contrast imaging:
  Probing rocky planets around our nearest neighbors. *A&A*, 576:A59.

Snellen, I. A. G., B. R. Brandl, R. J. de Kok, M. Brogi, J. Birkby, and H. Schwarz
  2014. Fast spin of the young extrasolar planet β Pictoris b. *Nature*, 509:63–65.

Snellen, I. A. G., R. J. de Kok, E. J. W. de Mooij, and S. Albrecht
  2010. The orbital motion, absolute mass and high-altitude winds of exoplanet
  HD209458b. *Nature*, 465:1049–1051.

Sparks, W. B. and H. C. Ford
  2002. Imaging Spectroscopy for Extrasolar Planet Detection. *ApJ*, 578:543–564.

Terebey, S., F. H. Shu, and P. Cassen
  1984. The collapse of the cores of slowly rotating isothermal clouds. *ApJ*, 286:529–551.

Vidal-Madjar, A., J.-M. Désert, A. Lecavelier des Etangs, G. Hébrard, G. E. Ballester, D. Ehrenreich, R. Ferlet, J. C. McConnell, M. Mayor, and C. D. Parkinson
  2004. Detection of Oxygen and Carbon in the Hydrodynamically Escaping Atmosphere of the Extrasolar Planet HD 209458b. *ApJ*, 604:L69–L72.

Vorobyov, E. I.
  2013. Formation of giant planets and brown dwarfs on wide orbits. *A&A*, 552:A129.

Wolszczan, A. and D. A. Frail
  1992. A planetary system around the millisecond pulsar PSR1257 + 12. *Nature*, 355:145–147.

Zhou, Y., D. Apai, G. H. Schneider, M. S. Marley, and A. P. Showman
  2016. Discovery of Rotational Modulations in the Planetary-mass Companion 2M1207b: Intermediate Rotation Period and Heterogeneous Clouds in a Low Gravity Atmosphere. *ApJ*, 818:176.

2 | Evidence against a strong thermal inversion in HD 209458 b

Broadband secondary-eclipse measurements of strongly irradiated hot Jupiters have indicated the existence of atmospheric thermal inversions, but their presence is difficult to determine from broadband measurements because of degeneracies between molecular abundances and temperature structure. Furthermore, the primary mechanisms that drive the inversion layers in hot-Jupiter atmospheres are unknown. This question cannot be answered without reliable identification of thermal inversions.

We apply high-resolution ($R = 100\,000$) infrared spectroscopy to probe the temperature-pressure profile of HD 209458 b. This bright, transiting hot-Jupiter has long been considered the gold standard for a hot Jupiter with an inversion layer, but this has been challenged in recent publications.

We observed the thermal dayside emission of HD 209458 b with the CRyogenic Infra-Red Echelle Spectrograph (CRIRES) on the Very Large Telescope during three nights, targeting the carbon monoxide band at 2.3 µm. Thermal inversions give rise to emission features, which means that detecting emission lines in the planetary spectrum, as opposed to absorption lines, would be direct evidence of a region in which the temperature increases with altitude.

We do not detect any significant absorption or emission of CO in the dayside spectrum of HD 209458 b, although cross-correlation with template spectra either with CO absorption lines or with weak emission at the core of the lines show a low-significance correlation signal with a signal-to-noise ratio of $\sim 3 - 3.5$. Models with strong CO emission lines show a weak anti-correlation with similar or lower significance levels. Furthermore, we found no evidence of absorption or emission from H_2O at these wavelengths.

The non-detection of CO in the dayside spectrum of HD 209458 b is interesting in light of a previous CO detection in the transmission spectrum. That there is no signal indicates that HD 209458 b either has a nearly isothermal atmosphere or that the signal is heavily muted. Assuming a clear atmosphere, we can rule out a full-disc dayside inversion layer in the pressure range 1 bar to 1 mbar.

2.1   Introduction

2.1.1   Hot-Jupiter atmospheres

Hot Jupiters form an ideal starting point for exoplanet atmospheric research. While they experience high levels of stellar irradiation, their atmospheric scale heights are relatively large, and their high temperatures result in high planet-to-star contrast ratios, especially in the infrared. Furthermore, since hot Jupiters have short orbital periods (1-5 days), they have a high probability of transiting their host star, and transits and eclipses occur on conveniently short timescales. The accessibility of hot Jupiters have made them excellent test objects for developing techniques for atmospheric characterisation - which are applicable to the next generation of telescopes and instruments and hence also to smaller planets (e.g. Schneider, 1994; Webb and Wormleaton, 2001; Seager and Deming, 2010; Snellen et al., 2013). The composition and structure of individual hot-Jupiter atmospheres are themselves of great interest to better understand the complex physical processes involved (including strong stellar irradiation, atmospheric circulation, and photochemical processes), and because they may hold clues to the planetary formation history (e.g. Öberg et al., 2011; Madhusudhan et al., 2014).

Atmospheric characterisation of hot Jupiters has so far mainly focused on transiting planets because they offer unique observational possibilities. When a planet transits its host star, part of the stellar light is filtered through the planetary atmosphere, leaving an absorption fingerprint in the observed light (Seager and Sasselov, 2000; Brown et al., 2001; Charbonneau et al., 2002). At the opposite side of the orbit, the star occults the planet, providing an opportunity to isolate the planetary contribution to the total flux. The difference between observations of the combined light of the star and planet in and out of secondary eclipse can be used to determine the planet's dayside spectrum (Charbonneau et al., 2005; Deming et al., 2005b). In addition, flux variations during the entire orbit can be measured as a function of phase, gaining information on the day- and nightside contributions (e.g. Knutson et al., 2007a; Snellen et al., 2009).

Hot Jupiters are assumed to have atmospheres that are dominated by molecular hydrogen, but the spectrum of a given planet will contain several spectroscopically active trace gases of carbon- and oxygen-bearing molecules. At high temperatures and observed in the infrared, the most abundant of these molecules are expected to be CO and H_2O, followed by CH_4. Other significant molecules are possibly CO_2, C_2H_2, and HCN (Madhusudhan, 2012; Moses et al., 2013).

2.1.2   Thermal inversion layers

The upper atmospheres of hot Jupiters are thought to be radiation dominated, with the radiation efficiency depending critically on the emission and absorption of the specific molecules that are present. Generally, the radiation from the host star is expected to deeply penetrate the atmosphere and heat it from below, which results in temperatures that decrease with increasing altitude (Guillot, 2010). However, strong optical or UV absorbers in the upper layers of the atmosphere can cause thermal inversion - a layer or region in the atmosphere in which the temperature instead increases with altitude (de Pater and Lissauer, 2010). Thermal inversions are common among the solar system planets. Jupiter, along with the other giant planets, has thermal inversions caused by CH_4-induced hazes, while the inversion in the terrestrial stratosphere is caused by O_3 (e.g. Seager, 2010, and references therein).

Thermal inversions may be commonly present in hot-Jupiter atmospheres as well. Secondary-eclipse measurements with the Spitzer Space Telescope have made it possible to probe the vertical temperature structure of bright transiting hot Jupiters. By measuring the relative depths of a secondary eclipse in multiple band-passes, a low-resolution thermal spectrum of the exoplanet can be constructed that can then be compared with theoretical spectra. There have been several reports of inversion layers in hot Jupiters from Spitzer observations (HD 209458b, Burrows et al. 2007; Knutson et al. 2008; XO-1b, Machalek et al. 2008; XO-2b, Machalek et al. 2009; TrES-4, Knutson et al. 2009; TrES-2, O'Donovan et al. 2010; Hat-P-7b, Christiansen et al. 2010), while other planets show no sign of an inversion (e.g. HD 189733b, Charbonneau et al., 2008). The inference of a thermal inversion is in most cases based upon an excess of flux in the 4.5 μm and 5.8 μm Spitzer band-passes, which has been interpreted as due to water emission features. However, many of these claims are based upon the comparison of only a few inverted and non-inverted atmospheric models, which may not adequately map degeneracies between atmospheric parameters. In contrast, a systematic retrieval analysis of secondary-eclipse spectra of nine hot Jupiters (Line et al. 2014) found little evidence for thermal inversions over a wide range of effective temperatures (with the exception of HD209458b).

The nature of the possible responsible absorbers is as yet unknown in this high-temperature regime. It has been proposed that highly irradiated planets are warm enough for significant amounts of gaseous TiO and VO to exist in the upper atmosphere, providing the necessary opacity to generate a temperature inversion (Hubeny et al., 2003; Fortney et al., 2006, 2008; Burrows et al., 2008). This advocates a correlation between high irradiation and existence of inversion layers. No observational evidence for TiO and VO absorption in hot Jupiter atmospheres

has been found, however (Huitson et al., 2013; Sing et al., 2013; Gibson et al., 2013; Bento et al., 2014; Hoeijmakers et al., 2015), although Désert et al. (2008) suggested TiO and VO molecules as possible candidates to explain observed absorption broadband features in the optical transmission spectrum of HD 209458 b.

The TiO/VO hypothesis has since been challenged by Spiegel et al. (2009), who argued that even a ten times supersolar abundance of VO is insufficient to drive a thermal inversion and that the high molecular weight of TiO requires substantial vertical mixing to retain a high abundance of TiO at low pressures. Apart from a deep vertical cold trap, TiO can be depleted by a nightside cold trap if it condenses to particles larger than a few microns (Parmentier et al., 2013). Furthermore, Madhusudhan et al. (2011) found that for carbon-rich (C/O > 1) hot Jupiters, most of the oxygen is bound up in CO, and as a result, the abundances of TiO and VO are too low to cause a thermal inversion. Alternatively, Knutson et al. (2010) found a preference for planets thought to host an inversion to orbit around chromospherically quiet stars and vice versa, and they theorised that increased UV levels for active stars were destroying the unknown compounds responsible for inversion layers. The inversion-causing absorbers could also be the result of non-equilibrium processes. Zahnle et al. (2009) propounded the photochemically produced sulfur compounds, S_2 and HS, as efficient UV and optical absorbers at high temperatures.

Comparative studies of hot Jupiters with and without temperature inversions are key to explaining the physical causes of inversion layers. Although such studies have been attempted (Fortney et al., 2008; Burrows et al., 2008; Knutson et al., 2010), this is not truly possible until a reliable method is available for measuring thermal inversions. Broadband photometry does not resolve the molecular spectral bands, which means that emission lines cannot be directly detected, and the inference of a thermal inversion must therefore rely heavily on models and their inherent assumptions. The Spitzer inferences of inversion layers tend to rely on assumptions about the presence of water, and typically, solar composition is assumed. Madhusudhan and Seager (2010) explored a wider paramater space and found evidence for degeneracies between the temperature pressure profile and the molecular abundances.

2.1.3   High-resolution spectroscopy

Ground-based high-dispersion spectroscopy in the near-infrared has recently become successful in characterising hot Jupiters. By resolving molecular features into individual lines, the lines can be reliably identified through line matching (Brown et al., 2002; Deming et al., 2005a; Barnes et al., 2007). Snellen et al. (2010) em-

ployed the Cryogenic Infra-Red Echelle Spectrograph (CRIRES, Kaeufl et al., 2004) at the Very Large Telescope (VLT) to observe the transmission spectra of HD 209458 b with a resolution of $R = 100\,000$, and detected CO at 2.3 µm. The technique makes use of the changing radial velocity of the planet during the observations to separate the planetary lines from the telluric and stellar lines.

The target planet can be observed favourably either during a transit (transmission spectroscopy) or at phases shortly before or after superior conjunction (dayside spectroscopy). Since a secondary eclipse is not required to separate the contamination from the parent star, dayside spectroscopy can also be applied to non-transiting planets. τ Boötis b has been observed at 2.3 µm with high resolution by Brogi et al. (2012) and Rodler et al. (2012), who detected absorption of CO, and the radial velocity measurements led to the first mass determination of a non-transiting hot Jupiter. The dayside spectrum of 51 Peg b revealed absorption from CO and possibly water (Brogi et al., 2013), but the signal was not detected in one of the three nights of observations, and therefore more data are necessary to confirm the result. CO absorption was detected in 2.3 µm dayside observations of HD 189733 b (de Kok et al., 2013). H_2O absorption was detected in 3.2 µm dayside observations of the same planet (Birkby et al., 2013), demonstrating the ability of high-resolution spectroscopy to also detect a more complex molecule in a wavelength regime more heavily contaminated by telluric lines. Recently, a combined signal from CO and H_2O absorption was detected in 2.3 µm dayside observations of HD 179949 b (Brogi et al., 2014), and Lockwood et al. (2014) detected H_2O in the dayside spectrum of τ Boötis b at L-band using NIRSPEC at Keck.

Dayside high-dispersion infrared spectroscopy has the potential to provide evidence for an inversion layer in a hot Jupiter. The molecular bands are resolved into individual lines, so that the average shape of the lines and the average contrast with respect to the stellar continuum can be measured, or at least constrained. The dayside spectrum of a hot Jupiter is sensitive to the presence of thermal inversions because the line-of-sight to a high degree coincides with the vertical direction in the planetary atmosphere. The sign of the vertical temperature gradient determines whether the thermal emission from the molecules in the upper atmosphere is seen as emission or absorption relative to the continuum part of the spectrum, emitted deep in the atmosphere (between 1 and 0.1 bar). The sign of the measured line contrast thus allows distinguishing between emission and absorption lines, and the shape of the lines can help further constrain the temperature-pressure profile.

2.1.4 HD 209458 b

At this point, all published high-dispersion detections of molecules have detected lines in absorption, but if instead emission lines were to be detected, this would

prove the existence of a thermal inversion. We therefore apply here the high-resolution technique to the dayside of the hot Jupiter HD 209458 b. The planet was the first exoplanet known to transit its parent star (Charbonneau et al., 2000), and today it is one of the best-studied hot Jupiters.

In the context of inversion layers, HD 209458 b is of particular interest since it was the first exoplanet reported to have a thermal inversion (Burrows et al., 2007; Knutson et al., 2008), and until recently, it was often proclaimed to be the benchmark for a hot Jupiter with a thermal inversion in its upper atmosphere. This was based on secondary-eclipse observations at 3.6, 4.5, 5.8 and 8.0 μm using the Spitzer Infrared Array Camera (IRAC Knutson et al., 2008). The 4.5 and 5.8 μm bandpasses showed an excess of flux relative to the 3.6 μm bandpass, in contrast to traditional models that expected a trough at these wavelengths due to water absorption features. The excess flux was best explained with a low-pressure inversion layer producing water emission features. The claim of a thermal inversion in HD 209458 b was supported by extensive modelling by Madhusudhan and Seager (2009, 2010) and Line et al. (2014). However, the existence of a thermal inversion in the atmosphere of HD 209458 b has recently been challenged. Zellem et al. (2014) measured the full orbit 4.5 μm phase curve with Spitzer IRAC using the now standard staring-mode observations and pixel-mapping techniques. They found the 4.5 μm secondary-eclipse depth to be 35% shallower than previously measured by Knutson et al. (2008), who did not use staring mode, nor intra-pixel sensitivity maps. This revision does not rule out an inversion layer, but is consistent with models both with and without a thermal inversion, or with a blackbody. Diamond-Lowe et al. (2014) have performed a self-consistent analysis of all available Spitzer/IRAC secondary-eclipse data of HD 209458 b. This includes both a reanalysis of the eclipses in the four IRAC bandpasses published by Knutson et al. (2008) and five previously unpublished eclipses in staring mode, one in 2007 at 8.0 μm, two in 2010 at 4.5 μm, and two in 2011 at 3.6 μm. They found no evidence for a thermal inversion in the atmosphere of HD 209458 b. Their best eclipse depths are well fitted by a model where the temperature decreases between pressure levels of 1 and 0.01 bars.

2.1.5   Re-evaluation of the HD209458b CO abundance from Snellen et al. (2010)

Carbon monoxide absorption has previously been observed with CRIRES at the VLT during a transit of HD 209458 b (Snellen et al., 2010), with a relative line strength at the level of $1 - 1.5 \times 10^{-3}$ with respect to the host star spectrum. Although a constraint on the CO volume-mixing ratio was presented, in hindsight it became clear that the underlying analysis did not include a thorough investiga-

tion of the parameter space. Furthermore, an erroneous conversion factor in the computation of the pressure broadening of the absorption lines resulted in a too high derived abundance. We note that the conversion error was only present in Snellen et al. (2010) and not in any of our subsequent work. We since performed a re-analysis of the constraints to the CO volume mixing ratio that can be inferred from the high-dispersion transit observations. A large grid of models was constructed, assuming a range of temperature-pressure profiles, abundances of a range of molecules, and pressure levels of the continuum. This re-analysis indicates that the observed relative line strength corresponds to a CO volume-mixing ratio in the range $10^{-5} - 10^{-4}$, with an additional uncertainty of a factor of ~ 2 if uncertainties in the high-altitude atmospheric temperature at the terminator region are included. However, if clouds or hazes contribute to the continuum extinction, the corresponding CO abundance could in turn be significantly higher.

2.1.6 Outline

In this paper we present three nights of CRIRES observations of HD 209458 at 2.3 μm, targeting CO in the planet's dayside, allowing us to probe the vertical temperature structure of the atmosphere. Section 5.3 details our observations of HD 209458 b, and Sect. 5.4 describes the data analysis steps from the raw spectra to removal of telluric contamination. In Sect. 2.4 the cross-correlation analysis we used to extract the potential planetary signal is explained, and the results are presented in Sect. 5.6. We discuss these in Sect. 2.6, and conclude in Sect. 2.7.

Table 2.1: Details of the observations, showing the observing date for the beginning of the night in local time, the use of nodding, the planetary phase, the total observing time, the number of observed spectra, range in airmass, water vapour, detector integration time (DIT), number of integrations per nod or observation (NDIT), and detector counts.

	2011-08-04	2011-09-05	2011-09-12
Nodding	yes	yes	no
Orbital Phase	0.51–0.57	0.55–0.62	0.54–0.61
t_{obs} [h]	6.07	5.53	6.02
N_{obs}	118	108	122
Airmass	2.16–1.38	2.27–1.38	2.20–1.38
DIT [s]	30	30	50
NDIT	5	5	3
Cnts [#/pix/s]	40–65	50–70	50–90

2.2   Observations

We observed HD 209458 ($K = 6.31$ mag) for a total of 17.5 hours during three nights in August and September 2011 as part of the large ESO program 186.C-0289, which was designed to study the brightest transiting and non-transiting hot-Jupiter systems visible from Cerro Paranal. The observations were obtained with the CRIRES instrument, which is mounted at the Nasmyth A focus of VLT Antu. We observed at the standard wavelength settings for the reference wavelength 2.3252 µm, covering the ro-vibrational (2,0) R-branch of carbon monoxide. The CRIRES instrument has four Aladdin III InSb detectors, each of the size 1024x512 pixels with gaps of about 280 pixels between the individual detectors.

We used a 0.2″ slit in combination with the Multi Application Curvature Adapative Optics system (MACAO, Arsenault et al., 2003) to achieve the highest possible resolution of $R \simeq 100\,000$. During each of the three nights, the target was observed continuously for 5–6 hours at planetary phases shortly after a secondary eclipse, when a significant portion of the dayside of the planet was visible. Additionally, a standard set of calibration frames was obtained during daytime and twilight.

The first two nights were observed in nodding mode, where the telescope is nodded along the slit by 10″ in an ABBA pattern, providing an easy method for background subtraction. The third night was observed without nodding in an effort to enhance stability and reduce overheads. Details of the observations are given in Table 5.2.

2.3   Data analysis

The data in this work have been analysed in a similar way as in Snellen et al. (2010) and Brogi et al. (2012, 2013), but all analyses were performed with new purpose-built Python scripts.

2.3.1   Extracting the one-dimensional spectra

The basic image processing was performed with the CRIRES pipeline version 2.1.3 and the corresponding version 3.9.0 of ESOREX. The images were dark-subtracted and flatfielded and were corrected for bad pixels and non-linearity effects. For the first two nights, the CRIRES pipeline was also used to combine the images in AB nodding pairs, thus performing a background subtraction, and to extract the 1D spectra. This resulted in a single extracted spectrum for every two observations. These spectra were extracted with the optimal extraction technique

(Horne, 1986). The spectra of the final night were observed without nodding, for which the CRIRES pipeline was ill-suited. Instead, we used the IRAF data analysis package *apall*, both for the background subtraction and the optimal extraction of the spectra.

Detectors 1 and 4 are both affected by the odd-even effect, a non-linear change in gain between odd and even columns along the spectral direction[1]. This is the result of the reading direction being perpendicular to the spectral dispersion for these two detectors. In particular, detector 4 showed residual odd-even imprints after non-linearity correction. Furthermore, detector 1 has very few expected carbon monoxide lines. For these reasons, we chose to leave out detectors 1 and 4 from further analysis, which now covers the wavelength range 2.3038 µm–2.3311 µm.

2.3.2 Bad-pixel correction and wavelength calibration

The extracted spectra were treated separately per night and per detector. The spectra were arranged into two-dimensional matrices with wavelength along the x-axis and time along the y-axis. The bad-pixel correction included in the CRIRES pipeline is insufficient, and we therefore manually identified bad pixels, columns, and regions through visual inspection of the matrices with the program DS9. A few larger regions consisting of several adjacent bad columns, such as the columns closest to the edge of the CCD's and a well-known defect on the second detector, were masked during the subsequent data analysis. The masked pixels made up about 2% of the total number of pixels. Remaining individual bad pixels and bad columns were corrected with cubic spline interpolation based on the four nearest neighbours on each side in the row.

All spectra of a given matrix were aligned to a common wavelength grid. We determined the offsets between centroids (determined using a Gaussian fit) of deep and isolated telluric lines in the individual spectra (typically 15-20 per array) and those in the average spectrum. The centroid offsets from a given spectrum showed no trend with wavelength and a typical scatter of less than 0.1 pixel with respect to each other. Each spectrum was therefore shifted with a spline interpolation using the median centroid offset of that spectrum. Next, we matched the pixel positions of centroids of telluric lines in the average aligned spectrum with the wavelengths in a synthetic telluric transmission spectrum from ATRAN[2] (Lord, 1992). The pairs of pixel position and wavelength were fitted with a second-order polynomial to yield the wavelength solution for a given night and detector. The highest residuals to the second-order fits were of the order $\pm 3 \times 10^{-6}$ µm, which corresponds

---

[1]http://www.eso.org/sci/facilities/paranal/instruments/crires/doc/VLT-MAN-ESO-14500-3486_v93.pdf

[2]http://atran.sofia.usra.edu/cgi-bin/atran/atran.cgi
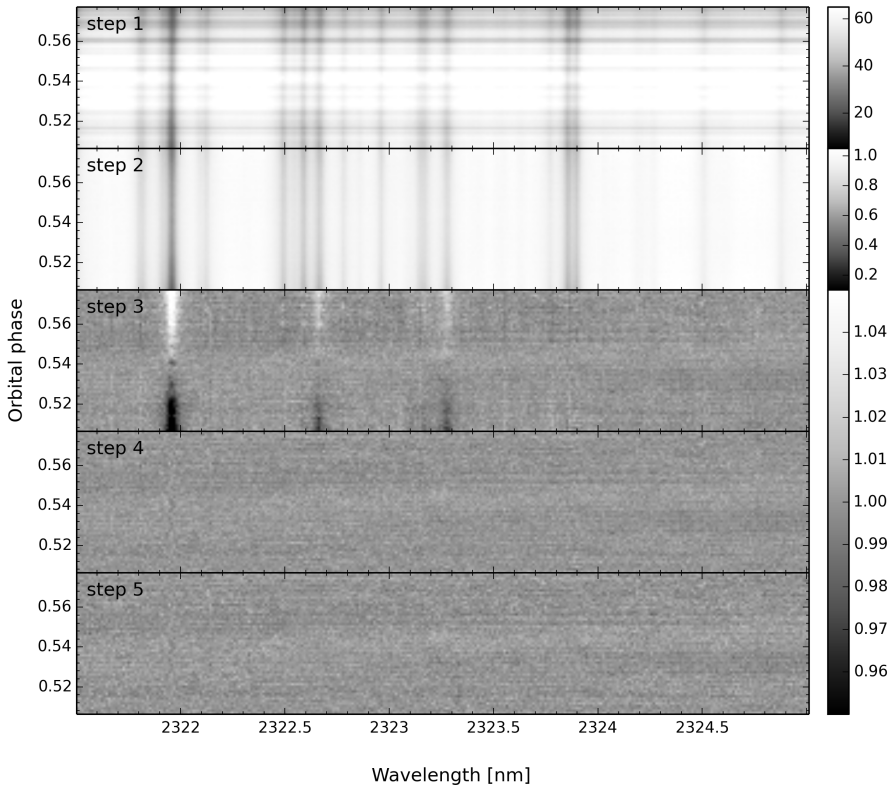
Figure 2.1: Overview of the different steps in the data analysis, showing a small fraction of the third array from the first night of observations. From top to bottom, step 1 shows the extracted spectra after bad-pixel correction, step 2 after spectral alignment and normalization, step 3 after first-order airmass correction, step 4 after second-order airmass correction, and step 5 after normalization of each column with the variance.

to 20% of a pixel. Finally, each spectrum was normalised by its median value.

2.3.3   Removing telluric contamination

The observed near-infrared spectra are dominated by absorption lines originating in the atmosphere of Earth, and a crucial datareduction step is therefore to remove this telluric contamination. The telluric lines are stationary in wavelength (but vary in strength) over the course of the observations, and therefore fall on fixed columns in the matrices. On the other hand, molecular lines arising in the planetary atmosphere are Doppler-shifted in each consecutive spectrum as the radial component of the orbital velocity of the planet changes, resulting in diagonal features across

the matrices, buried in the noise. The planet lines typically move by 30 to 40 pixels during one night of observation. This means that we can manipulate the matrices column by column without significantly affecting the planetary signature.

The variations along columns of the matrices are strongly correlated with the changing airmass over the time interval of the observations. We corrected for this with a linear least-squares fit of the logarithm of the fluxes in each column as a function of geometric airmass.

At the positions of some of the more prominent telluric lines, there are clear residuals, showing a correlation with time. These second-order effects stem from changing conditions in Earth's atmosphere over the course of the night. Two distinct patterns in time were recognizable and were found to correspond to water and methane lines. We sampled the two effects of flux with time in a few affected columns in a strong water line and a strong methane line. We then corrected the remaining matrix by expressing each column as a linear function of the sampled effects and dividing by the fit. The second-order airmass fitting can be affected by the planetary signal we are ultimately looking for. In particular, in columns (wavelengths) where the planet signal is at the start or end of the time series, the fit can be affected by this additional signal and therefore partially compensate for it. This is overall typically a 10% effect. Therefore we masked pixels expected to contain a planetary signal when performing this step.

Following this, a few columns that coincided with the wavelengths of the deepest telluric lines were visibly more noisy than the rest. We divided each column by the variance of itself to ensure that the noisiest columns did not dominate the cross-correlation in the next step of the data analysis. An example of the intermediate results of the different steps in the data reduction is shown in Fig. 5.2. We achieve a typical signal-to-noise ratio (S/N) of $\sim$250 per pixel per spectrum for the first two nights, and $\sim$200 per pixel per spectrum for the final night, for which we did not dither.

2.4   Search for the planet signal

The individual planetary lines are buried in the noise of the residual spectra. With the chosen wavelength setting of 2.3 μm, we are targeting the (2,0) R-branch of CO, and we expect tens of CO lines within the observed wavelength range (see Fig. 2.2). The signals from the individual lines are combined by cross correlating the residual spectra one at a time with purpose-built model spectra. In this section we describe the model spectra and the cross-correlation analysis used to search for a planetary signal in the observed spectra.
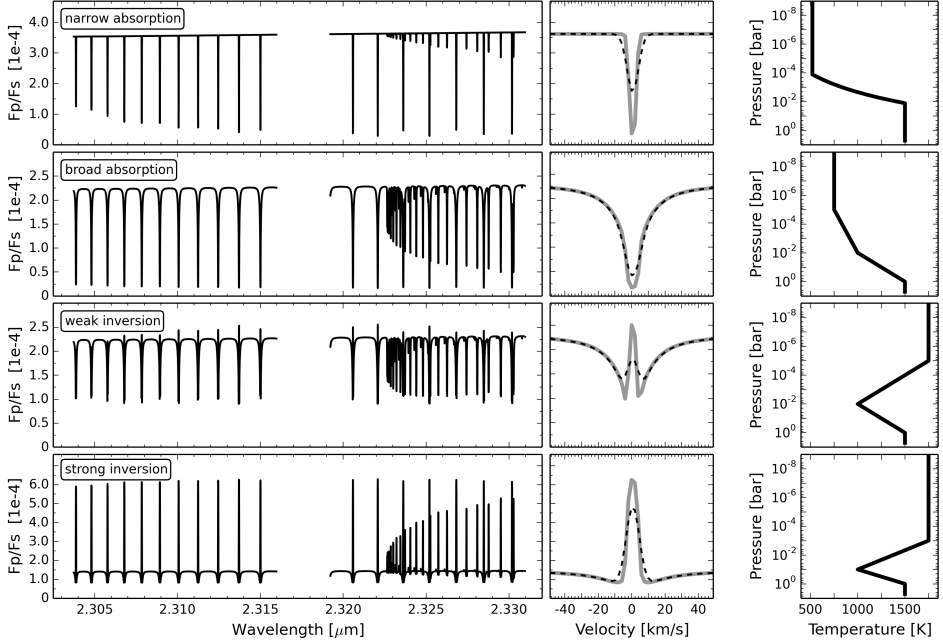
Figure 2.2: Examples of CO model spectra used in the cross-correlation analysis. The model in the top row has an adiabatic lapse rate and a CO VMR of $10^{-4.5}$, resulting in strong, narrow absorption lines. The following three rows are models from the T/p grid described in Sect. 4.5.1, all with CO VMR $= 10^{-4.0}$: the first is without a thermal inversion and with relatively broad absorption lines, the second is with a weak inversion, and the last model is for a strong thermal inversion. The left column displays the models before convolution to CRIRES resolution over the wavelength coverage of the two central detectors. The middle column zooms in on the CO line at approximately 2.3205 μm, showing the line profiles both before (solid) and after (dashed) convolution to CRIRES resolution. The right column gives the corresponding T/p profiles.

2.4.1 Model spectra

The model spectra of HD 209458 b were calculated line by line using parameterised temperature-pressure profiles (T/p profiles), H_2-H_2 collision-induced absorption (Borysow et al., 2001; Borysow, 2002) and with either CO or H_2O as a single trace gas. The CO and H_2O data were taken from HITEMP 2010 (Rothman et al., 2010), and a Voigt line profile was employed. We used the parameter values for the Voigt profile as given by the HITEMP database. Uncertainties in the line shape parameters will mainly influence the depths of the lines, not the cross-correlation values, since the CO lines are widely separated, and the spectral shape will not be affected much. In this article, we focus on the analysis and results from

cross correlating with the model spectra with CO as the single trace gas. A short summary of the results from the H_2O models, which showed no signs of a signal, is given in Sect. 2.5.2.

We performed the cross-correlation analysis for a grid of models spanning a range of T/p profiles and CO volume-mixing ratios (VMR). The T/p profiles describe the average vertical temperature structure of the dayside of the planetary atmosphere. All the models in the grid are isothermal with a temperature of $T_1 = [1500\,\text{K}, 2000\,\text{K}]$ at pressures higher than $P_1 = 1\,\text{bar}$. The temperature decreases with a constant lapse rate (i.e. the rate of temperature change with log pressure) until it reaches $T_2 = 1000\,\text{K}$ at pressure $P_2 = [10^{-1}\,\text{bar}, 10^{-2}\,\text{bar}]$. At higher altitudes there is either an inversion layer or not, depending on the temperature $T_3 = [750\,\text{K}, 1750\,\text{K}]$ at the pressure $P_3 = [10^{-3}\,\text{bar}, 10^{-5}\,\text{bar}]$, above which the models again become isothermal. This amounts to eight different T/p profiles with an inversion layer and eight T/p profiles without, all of which were tested with three different volume-mixing ratios, $\text{VMR} = [10^{-4.5}, 10^{-4.0}, 10^{-3.5}]$.

The three bottom rows of Fig. 2.2 show representative examples of CO model spectra from the T/p grid: A model atmosphere without a thermal inversion, and two with inversion layers, all with CO $\text{VMR} = 10^{-4.0}$. The model without an inversion has absorption lines, while the two models with thermal inversions conversely show emission at the core of the CO lines and absorption in the wings. In the following, we refer to the model with the strongest emission lines as the strong-inversion model and to the one with weaker emission as the weak-inversion model. The distinction between weak and strong is based on whether or not the core emission is below or above the continuum level after convolving to the resolution of the CRIRES instrument. All the models from the grid without an inversion layer have relatively broad CO absorption lines (FWHM $\sim$ 10 to 45 km s^{-1}), which have a tendency to smear out the planetary signal in the cross-correlation analysis. We therefore also investigated a CO model with more narrow absorption lines (FWHM $\sim$4 km sec^{-1}), illustrated in the top row of Fig. 2.2. This model has no thermal inversion and an adiabatic lapse rate until the assumed lowest temperature of 500 K, thus maximising the temperature gradient for the given CO volume-mixing ratio, which in this case is $1 \times 10^{-4.5}$.

More inversion models

For comparison, we calculated an additional suit of CO models with a thermal inversion with T/p profiles qualitatively and quantitatively similar to the best-fit T/p profiles in Madhusudhan and Seager (2009). We call these the MS models. Madhusudhan and Seager (2009) applied an atmospheric retrieval method with a parametric T/p profile to the Spitzer IRAC secondary-eclipse depths in Knutson et al.

(2008), supporting and constraining a dayside thermal inversion in HD 209458 b. The T/p profiles of the MS models are shown in black in Fig. 2.3 together with the profiles from the thermal inversion models of the T/p grid described in Sect. 4.5.1 shown in red. We calculated the MS models using three different CO volume-mixing ratios, VMR $= [10^{-5}, 10^{-4}, 10^{-3}]$.

The thermal inversions of the MS models are located deeper in the atmosphere than those from the T/p grid in the previous section. This results in strong emission in all cases and in line shapes that are very sensitive to the volume mixing ratio. The models with the lowest VMR $= 10^{-5}$ probe relatively low altitudes, making the inversion layer more spectroscopically dominant, thus resulting in line profiles with pure emission after convolution to CRIRES resolution. Models with higher VMRs still have siginificant emission due to the deep inversion layer, but they have absorption at the core of the lines because the core probes higher altitudes than for the lower VMRs where the temperature again decreases with increasing altitude. The shape of the lines at CRIRES resolution of MS models with a VMR of 10^{-4} or 10^{-3} resemble the line profile of the weak-inversion model in the middle panel of Fig. 2.2 at CRIRES resolution, only mirrored vertically.

Note that recent analyses of the dayside spectrum of HD209458b by Diamond-Lowe et al. (2014) and Zellem et al. (2014) found that the data were best fit by a near-isothermal T/p profile. However, with high-dispersion spectroscopy we are only sensitive to the narrow components of the spectra, which are produced relatively high up in the atmosphere, making our observations insensitive to such a near-isothermal atmosphere. This is further discussed in Sect. 2.6.

2.4.2   Cross-correlation analysis

Each model was convolved to the CRIRES resolution using a Gaussian filter, then Doppler-shifted over the range -250 to $250\,\mathrm{km\,s^{-1}}$ in steps of $1.5\,\mathrm{km\,s^{-1}}$, and for each velocity step cross-correlated with the residual spectra. The velocity range was chosen to cover every possible radial velocity of the planet, and the step size roughly corresponds to the pixel velocity scale of the detectors. The outcome is a geocentric correlation matrix, with the strength of the cross-correlation as a function of the applied radial velocity shift and the spectrum number (i.e. time). The cross-correlation was performed separately for each night and detector.

To maximise a potential planet signal, each row of the geocentric cross-correlation matrices, that is, the cross-correlation functions for each spectrum, was shifted to the rest frame of the planet, then summed over time. Finally, the summed, planetocentric cross-correlation functions from detectors 2 and 3 from all three nights were combined, providing the total cross-correlation functions (T-CCF).

The radial velocity corrections (rv_corr) from the geocentric to the planetcentric
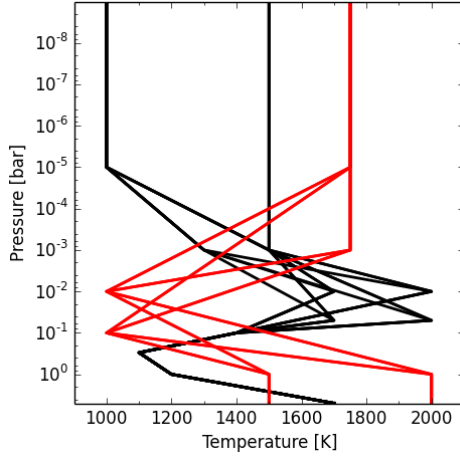
Figure 2.3: Temperature-pressure profiles of models hosting a thermal inversion. The red profiles are the ones from the T/p grid described in Sect. 4.5.1 and the black profiles are the MS models described in Sect. 2.4.1. The deep inversion layers of the MS models give rise to strong CO emission.

frame are a function of time and are given by

$$rv_{\mathrm{corr}}(t) = rv_{\mathrm{planet}}(t) + rv_{\mathrm{helio}}(t) + V_{\mathrm{sys}}. \tag{2.1}$$

Here, rv_{planet} is the radial velocity curve of the planet, rv_{helio} is the heliocentric correction term, and V_{sys} is the systemic velocity of the host star (-14.69 $\pm$ 0.09 km s^{-1}, Nidever et al., 2002). Assuming a circular orbit (Crossfield et al., 2012), the radial velocity curve is given by

$$rv_{\mathrm{planet}}(t) = K_{\mathrm{P}} \sin(2\pi\varphi(t)), \tag{2.2}$$

with K_{P} being the semi-amplitude of the orbital radial velocity of the planet and φ being the orbital phase. The orbital period and the mid-transit time used to calculate the phases of the planet are adopted from Knutson et al. (2007b).

Since HD 209458 b is a transiting planet with an inclination of $i = 86.589° \pm 0.076°$ (Southworth, 2008) close to 90 degrees, K_{P} equals the orbital velocity $V_{\mathrm{orb}} = 140 \pm 10$ km s^{-1} (Snellen et al., 2010) to within the uncertainty. However, we investigated a wider range of K_{P} values (50 $-$ 170 km s^{-1}) and V_{sys} values (-75 $-$ 45 km s^{-1}) to scan the parameter space and check the strength of potential spurious signals.
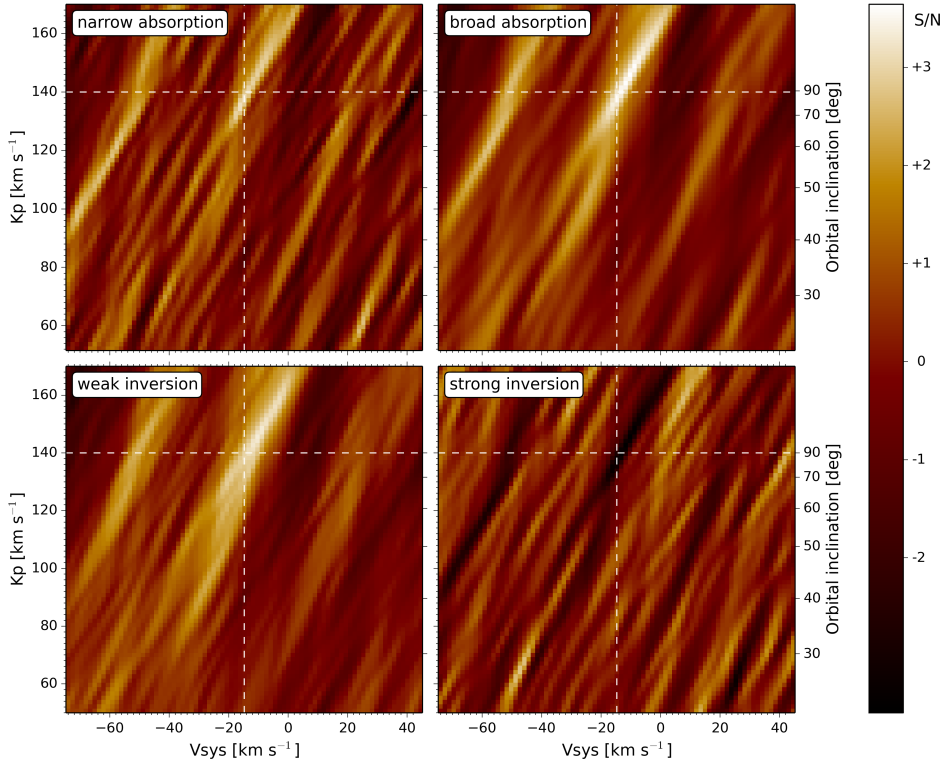
Figure 2.4: Total cross-correlation diagrams for the four models illustrated in Fig. 2.2 after summing over time for a range of V_{sys} and K_P values, and combining detectors 2 and 3 from the three observation nights. The dashed white lines indicate the expected planet signal based on literature values, which coincides with a weak correlation signal in the case of the two absorption models as well as the weak-inversion model, and a weak anti-correlation signal in the case of the strong-inversion model. Although there are hints of a signal visible, CO is not detected with statistical significance.

2.5   Results

The diagrams in Fig. 2.4 show the strength of the total cross-correlation as function of K_P and V_{sys} for the four example models from Fig. 2.2. The colour scale indicates the signal of the total cross-correlation function for a given parameter set. The S/N was obtained by dividing the total cross-correlation values by their standard deviation excluding points in parameter space close to the expected signal position. The K_P values translate into orbital inclinations, which are given on the right-hand axis of the figures. The literature K_P and V_{sys} values are indicated by the dashed white lines.

The absorption models and the weak-inversion models in the grid show a S/N = 3 − 3.5 hint of a CO correlation signal at a position within the uncertainties of the literature values of K_P and V_{sys}. The models from the T/p grid with the strongest emission lines and only low-level absorption in the wings, such as shown in the bottom panel of Fig. 2.2, give the lowest cross-correlation values. In fact, these models give rise to anti-correlation signals with S/N values of -2.5 − -3.5. This is expected because the strong-inversion models are close to the inverse of the non-inversion models. The peak of the cross-correlation signal in the T-CCF diagram is in all cases very close (within 1 σ) to the expected position of the planet signal. The values of the peak cross-correlation signals, their positions, and the cross-correlation signal at the expected planet position for the four example models are all given in Table 2.2.

The $\sim 3\sigma$ signal we obtain for non-inverted models is in our opinion not strong enough to claim an unambiguous detection of CO. In the T-CCF diagrams (Fig. 2.4) one can see spurious signals that are only slightly lower in significance. Indeed, in previous analyses where we claimed planet signals, we obtained significantly higher S/N in the range S/N 4 − 6 (Snellen et al., 2010; Brogi et al., 2012; Birkby et al., 2013; de Kok et al., 2013; Brogi et al., 2014).

The diagonal noise structures in the T-CCF diagrams of Fig. 2.4 are a result of a degeneracy between K_P and V_{sys}, with the slope depending on the observed orbital phases of the planet. The combination of three nights with slightly different phases, all with the planet on the same side of the host star, has acted to broaden and distort these naturally occurring noise structures. The noise structures are also affected by the line shape of the model. Cross-correlation with the narrow absorption model results in more narrow noise structures, and the location of the potential CO signal is better defined. At the opposite end of the scale is the weak-inversion model, for which the line shapes at the CRIRES resolution resemble absorption doublets (see Fig. 2.2). Cross-correlation with this much broader line profile smoothes the potential signal along the diagonal noise structures, increasing the uncertainty in

Table 2.2: Results from the cross-correlation analysis for the four example models from Fig. 2.4. The first column gives the S/N of the correlation or anti-correlation signal at the expected planet postion (-14.69, 140)km s^{-1}. The second column gives the peak (anti-)correlation value, and the third column gives the location of the peak relative to the expected position. Note that these positions are all well within the 1σ uncertainty.

	S/N at planet pos.	S/N peak	peak location [km s^{-1}]
narrow abs.	2.8	3.2	(-1.5, +4.5)
broad abs.	3.2	3.6	(+4.5, +7.5)
weak inv.	3.0	3.4	(+4.5, +7.5)
strong inv.	-2.8	-3.6	(+4.5, +7.5)

the peak position. The peak cross-correlation values as given in Table 2.2 all fall along the degenerate diagonal of the diagrams.

2.5.1   MS models

The models with temperature-pressure profiles similar to the best-fit models of Madhusudhan and Seager (2009) have two basic types of CO line shapes at the CRIRES resolution, as described in Sect. 2.4.1. The pure emission lines can be seen as a mirror of the pure absorption lines from the T/p grid, and the lines with absorption at the core and strong emission in the wings are mirrors of the line shapes of weak-inversion models from the T/p grid. We do not detect carbon monoxide when cross-correlating the MS models with the observed residual spectra, as described in Sect. 4.5.2. The S/N at the expected planet position is about -3.3 for the models with strong simple emission lines and about -2.8 for the models with some absorption at the core of the otherwise emission-dominated lines. The weak anti-correlations are consistent with the results from the T/p grid models, and indeed the T-CCF diagrams of the MS models look like colour-inverted versions of the diagrams for the models with broad absorption lines and weak inversion in Fig. 2.4.

2.5.2   Water models

We have also cross correlated model spectra with water as the single trace gas. The water models were calculated using the same T/p grid as for the CO models, but the tested volume-mixing ratios for the H$_2$O models were VMR = $[10^{-5}, 10^{-4}, 10^{-3}]$.
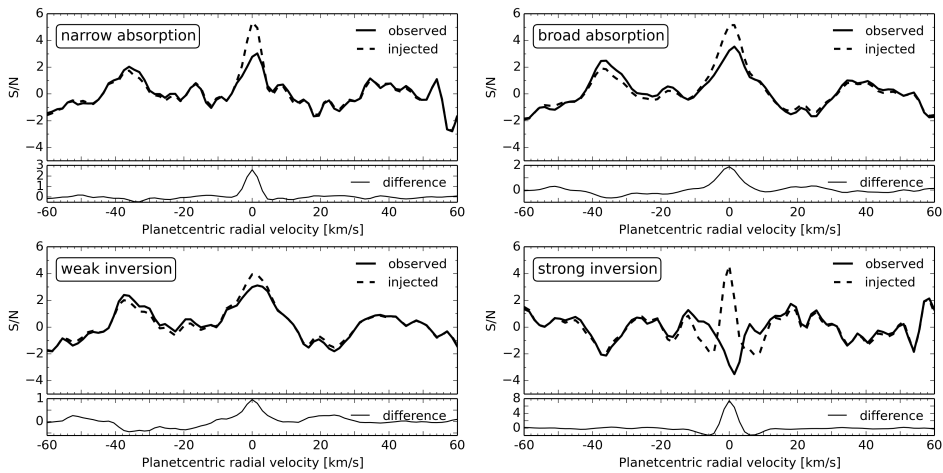
Figure 2.5: Slices through the total cross-correlation diagrams for the four atmospheric models from Fig. 2.2, assuming the literature values $V_{\mathrm{sys}} = -14.69\,\mathrm{km\,s^{-1}}$ and $K_{\mathrm{P}} = 140\,\mathrm{km\,s^{-1}}$. The solid line is the T-CCF from cross-correlating a given model with the observed spectra, and the dashed line is the T-CCF from injecting the model at nominal strength into the observed spectra before telluric removal, and then cross-correlating with the same model. The differences between the observed and the injected T-CCFs are shown in the lower panels, and the peak signal in the difference T-CCFs are good estimates of expected S/N correlation signals, if the models are correct.

We did not detect a water signal from cross-correlating with any of the H_2O models. The typical correlation S/N at the expected planet position lies within ± 1, and there is no systematic behaviour in the T-CCF diagrams as a function of the line profiles, such as for the CO models. Recently, Madhusudhan et al. (2014) constrained the H_2O abundance of HD 209458 b to sub-solar levels assuming a clear atmosphere, with the central H_2O VMR measured to be 5.4×10^{-6}, which is lower than the VMRs of the models in this work. The water abundance may still be solar or supersolar if the atmosphere of HD 209458 b has clouds or hazes.

2.5.3   Estimating expected CO signals

We injected model spectra into the observed spectra as fake planet signals and subsequently retrieved the signals to evaluate the expected CO signals as function of volume-mixing ratio and T/p profile.

First the model planet spectrum (F_{model}) was scaled with respect to the stellar continuum of the parent star. We adopted the effective temperature for HD 209458 of 6092 K (Boyajian et al., 2015), and approximated the stellar spectrum from a linear interpolation between two Castelli-Kurucz stellar atmosphere models[3] with [M/H]=0.0, $\log g = 4.5$ and the temperatures 6000 and 6250. The scaling was subsequently performed according to

$$F_{scaled}(\lambda) = \frac{F_{model}(\lambda)}{F_S(\lambda)} \left(\frac{r_P}{r_S} \right)^2, \tag{2.3}$$

where F_S is the model stellar spectrum, and r_P and r_S are the radii of the planet and star. The scaled model planet spectrum was then convolved to match the CRIRES resolution. For each observed spectrum the relative radial velocity between HD 209458 b and the observer was calculated using Eq. (2.1), and the scaled model planet spectrum was Doppler-shifted accordingly before being injected into the aligned and normalised observed spectra (step 2 in Fig. 5.2) using

$$F_{obs+fake}(\lambda) = F_{obs}(\lambda) \cdot (1 + F_{scaled}(t, \lambda)). \tag{2.4}$$

We then proceeded with the telluric removal as described in Sect. 2.3.3, and the fake planetary signal was retrieved by cross-correlating with the same input model spectrum as described in Sect. 4.5.2.

Since the parameter $K_P = 140 \, \mathrm{km \, s^{-1}}$ of the injected signal is precisely known, it is sufficient to examine slices through the T-CCF diagram when estimating the expected signals. Such one dimensional T-CCfs are shown in Fig. 5.6 for each

---

[3]ftp://ftp.stsci.edu/cdbs/grid/ck04models/

of the four example models from Fig. 2.2. The T-CCFs obtained from cross-correlating with the observed spectra are the solid lines, and the dashed lines are the T-CCFs from cross-correlating with the spectra injected with artificial planet signals. The injected planetary signatures show up as central peaks. We note that the shape of the four injected T-CCFs in Fig. 5.6 are to a high degree determined by the auto-correlation function of the average line profile of the model. This is especially true for the relatively large negative wings on either side of the correlation peak of the strong-inversion model.

Since the injected signal is superimposed on top of the observed T-CCF, we need to examine the difference between the T-CCF with and without the injected signal, which are shown in a sub-panel below the T-CCFs in Fig. 5.6. This shows that we can expect signals with a S/N of 2.6 for the narrow-absorption model, 1.9 for the broad-absorption model, 1.0 for the weak-inversion model, and 7.4 for the strong-inversion model. These results are to be interpreted as the approximate strength of the signal we should be able to detect if that spectral signature is present in the planetary atmosphere.

Both of the absorption models have expected signals that are similar in strength to the observed signals, but because there are spurious signals of similar strength, more data are needed to confidently confirm the detection of CO absorption lines. For the strong-inversion model, it is immediately clear that the observed correlation results are a poor match to the expected results. The emission lines are expected to give rise to a strong planetary signature, but there is no hint of this in the observed T-CCF. Instead, the observed T-CCF shows a weak anti-correlation signal, consistent with the possible presence of absorption lines. The weak-inversion model has an expected S/N < 1, revealing that it is very difficult to detect models with such line profiles.

Line contrast

For the simplest line profiles, those with either pure absorption or pure emission, it is possible to place an upper limit on the line contrast, that is, the line strength relative to the stellar continuum. We performed this analysis for the two absorption models in the top panels of Fig. 2.2. The model was injected into the observed spectra with variable strength by multiplying F_{scaled} in Eq. (2.3) and (2.4) with a variable scaling factor S. For each value of S the difference between the observed and injected T-CCFs was determined, and we measured the line contrast of the model $S * F_{\text{scaled}}(\lambda)$, which gave rise to a correlation signal with S/N = 3. This resulted in a line contrast of $\sim 3.2 \times 10^{-4}$ for both the narrow- and broad-absorption model.

2.6   Discussion

We searched for a CO signal in dayside spectra of HD 209458 b by cross-correlating with template spectra with CO as the single trace gas, and assuming many different temperature-pressure profiles that covered atmospheres with and without a temperature inversion. The presence of an inversion layer gives rise to CO emission in the spectra of the planet, but depending on the pressure range and temperature gradient of the inverted layer, the shape of the CO lines can differ significantly. A thermal inversion will give rise to strong emission when it is located deep in the atmosphere and has a large temperature difference. The depth of a temperature inversion depends on the opacity sources responsible for the inversion, but since the sources are unknown in hot Jupiters, it is relevant to test models with inversions at different depths. At the high spectral resolution of the CRIRES instrument, more complex line shapes can be partly resolved, with the core of the lines probing higher altitudes, while the wings of the lines probe deeper, just above where the atmosphere becomes optically thick. The line shape for a given T/p profile is to a lesser degree also affected by the CO volume-mixing ratio because the VMR influences the probed pressure range.

We have tested models with a wide variety of line shapes: Pure absorption and pure emission lines, as well as models with either emission at the core and absorption in the wings, or absorption at the core and emission in the wings. We did not detect carbon monoxide in the HD 209458 b dayside spectrum with statistical significance, regardless of which model we cross-correlated with. The models with non-inverted atmospheres and the models with a weak-inversion layer, typically located at pressures lower than 0.01 bar, all show a hint of a correlation signal with S/N = $3.0 - 3.5$, while the models with stronger inversion layers, including the MS models with T/p profiles like those of Madhusudhan and Seager (2009), show anti-correlation signals with similar low-significance levels.

Our results are inconsistent with the inference of Knutson et al. (2008) of a thermal inversion in HD 209458 b based on Spitzer IRAC broadband photometry, but agrees with the more recent IRAC data and analysis by Zellem et al. (2014) and Diamond-Lowe et al. (2014), who both found that a thermal inversion is not required to explain the Spitzer secondary-eclipse depths. In fact, the best-fitting T/p profile found by Diamond-Lowe et al. (2014) is isothermal at pressures lower than 0.1 bar. However, the high-resolution spectroscopy method is only sensitive to narrow components in the planetary spectrum - any broad component is filtered out in the early stages of the analysis. In Fig. 2.6 we show the contribution function for a CO volume-mixing ratio of 10^{-3}, indicating that our data are mostly sensitive to temperature differences in the 10^{-5} to 10^{-2} pressure range. This means that

we expect no signal from an atmosphere such as shown by Diamond-Lowe et al. (2014). Our non-detection is therefore consistent with their results.

The non-detection of CO in the dayside spectrum of HD 209458 b is interesting in light of previous successes with detecting CO using high-resolution spectroscopy at 2.3 µm, both in the dayside spectra of other hot Jupiters (Brogi et al., 2012; Rodler et al., 2012; Brogi et al., 2013; de Kok et al., 2013; Brogi et al., 2014) and in the transmission spectrum of HD 209458 b itself (Snellen et al., 2010). Snellen et al. detected CO absorption and determined the line strength relative to the stellar continuum to be $1 - 1.5 \times 10^{-3}$, while in this work we obtain a best estimate of the relative line strength for simple absorption lines in the dayside spectrum to be $\sim 3.2 \times 10^{-4}$.

The most likely explanation for the lack of CO signal is that the average dayside T/p profile is near-isothermal in the pressure range we probe ($10^{-1} - 10^{-5}$ bar, see Fig. 2.6). However, we note that at high altitudes there may still be a weak inversion layer, for instance at pressures $<< 10^{-3}$ bar, which are only probed by very narrow cores of the CO lines. Furthermore, when observing the dayside spectrum of HD 209458 b, the spectrum is disk integrated. HD 209458 b is expected to be tidally locked to its parent star, and Zellem et al. (2014) have observed the planet to have a hotspot, shifted eastward of the substellar point due to equatorial superrotation, as expected if the planet is in synchronous rotation. It is possible that the planetary atmosphere has a thermal inversion only in the substellar point, or alternatively, in the eastward-shifted hotspot. If a thermal inversion is localised to only a part of the dayside, the effect of the inversion will be muted.

Although high, the limited spectral resolution ($R = 100\,000$) of the CRIRES instrument can work to dampen a thermal inversion signal somewhat. This is especially true for the weakest inversions (high altitude and less steep temperature gradient dT/dP), where the emission at the core of the lines is so weak that the complex line profiles are reduced to slightly muted, simple absorption lines. This effect alone cannot explain the lack of a CO detection, but it may be a contributing factor.

Alternatively, the CO signal, whether it is absorption or emission, might be heavily dampened by clouds or hazes. Charbonneau et al. (2002) first suggested an opaque cloud layer as a possible explanation for the lack of a strong optical Na feature in the optical transmission spectrum of HD 209458 b, although they noted that if clouds were the sole explanation, the cloud tops were required to be located above pressures of 0.4 mbar. It is unclear if such high-altitude cloud layers can exist in hot Jupiters, although Fortney et al. (2003) suggests it is possible to have clouds at pressures of several millibars. However, one does expect that the contributions from clouds or hazes will be significantly stronger in transit spectra than in the

dayside spectrum because of the grazing geometry in the former. Deming et al. (2013) and Madhusudhan et al. (2014) have observed the transmission spectrum of HD 209458 b with HST/WFC3 and both found weak transit features that possibly require haze. The haze alone is not expected to have a major influence on the thermal emission spectrum, but a cloud or haze layer at altitudes below those probed by transit observations might influence the continuum level for the thermal emission spectra and hence our results. The role of clouds or haze is thus still unclear.
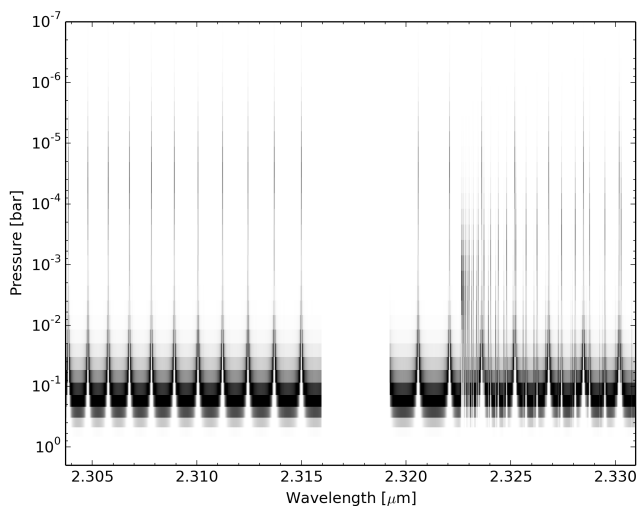
Figure 2.6: Contribution function of the CRIRES observations for a CO volume-mixing ratio of 10^{-3}, with CO as a single trace gas. Note that these observations are sensitive to the narrow-line components over a pressure range $\sim10^{-2}$ to $\sim10^{-5}$ bar. In particular, in this range the T/p profile as derived by Diamond-Lowe et al. (2014) is near isothermal, making these observations insensitive to it.

2.7   Conclusion

We did not detect carbon monoxide at a statistically significant level in the 2.3 μm high-resolution dayside spectrum of HD 209458 b, although we saw a potential absorption signal at the $3 - 3.5\sigma$ level. CO is expected to be abundant in hot Jupiters according to theory (e.g. Madhusudhan, 2012), and has been found to be present in the tranmission spectrum of the planet (Snellen et al., 2010). A near-isothermal pressure profile of the planetary atmosphere is the most probable cause of the lack of CO signal.

We showed that high-resolution spectroscopy can in principle measure line shapes and constrain the temperature pressure profiles in exoplanet atmospheres. In general, it will be possible to distinguish between a clear atmosphere with and without a thermal inversion, as long as these occur within the probed pressure range.

Our observations support the recent findings by Diamond-Lowe et al. (2014) and Zellem et al. (2014) that there is no strong inversion layer in the dayside atmosphere of HD209458b, in the pressure range 10^{-1} bar $- 10^{-3}$ bar. The emission signal from such an inversion layer would have been readily detected in our spectra.

References

Arsenault, R., J. Alonso, H. Bonnet, J. Brynnel, B. Delabre, R. Donaldson, C. Dupuy, E. Fedrigo, J. Farinato, N. N. Hubin, L. Ivanescu, M. E. Kasper, J. Paufique, S. Rossi, S. Tordo, S. Stroebele, J.-L. Lizon, P. Gigan, F. Delplancke, A. Silber, M. Quattri, and R. Reiss
2003. MACAO-VLTI: An Adaptive Optics system for the ESO VLT interferometer. In *Adaptive Optical System Technologies II*, P. L. Wizinowich and D. Bonaccini, eds., volume 4839 of *Proc. SPIE*, Pp. 174–185.

Barnes, J. R., T. S. Barman, L. Prato, D. Segransan, H. R. A. Jones, C. J. Leigh, A. Collier Cameron, and D. J. Pinfield
2007. Limits on the 2.2-μm contrast ratio of the close-orbiting planet HD 189733b. *MNRAS*, 382:473–480.

Bento, J., P. J. Wheatley, C. M. Copperwheat, J. J. Fortney, V. S. Dhillon, R. Hickman, S. P. Littlefair, T. R. Marsh, S. G. Parsons, and J. Southworth
2014. Optical transmission photometry of the highly inflated exoplanet WASP-17b. *MNRAS*, 437:1511–1518.

Birkby, J. L., R. J. de Kok, M. Brogi, E. J. W. de Mooij, H. Schwarz, S. Albrecht, and I. A. G. Snellen
2013. Detection of water absorption in the day side atmosphere of HD 189733 b using ground-based high-resolution spectroscopy at 3.2 μm. *MNRAS*, 436:L35–L39.

Borysow, A.
2002. Collision-induced absorption coefficients of H_2 pairs at temperatures from 60 K to 1000 K. *A&A*, 390:779–782.

Borysow, A., U. G. Jorgensen, and Y. Fu
2001. High-temperature (1000-7000 K) collision-induced absorption of H"2 pairs computed from the first principles, with application to cool and dense stellar atmospheres. *J. Quant. Spec. Radiat. Transf.*, 68:235–255.

Boyajian, T., K. von Braun, G. A. Feiden, D. Huber, S. Basu, P. Demarque, D. A. Fischer, G. Schaefer, A. W. Mann, T. R. White, V. Maestro, J. Brewer, C. B. Lamell, F. Spada, M. López-Morales, M. Ireland, C. Farrington, G. T. van Belle, S. R. Kane, J. Jones, T. A. ten Brummelaar, D. R. Ciardi, H. A. McAlister, S. Ridgway, P. J. Goldfinger, N. H. Turner, and L. Sturmann
2015. Stellar diameters and temperatures - VI. High angular resolution mea-

surements of the transiting exoplanet host stars HD 189733 and HD 209458 and implications for models of cool dwarfs. *MNRAS*, 447:846–857.

Brogi, M., R. J. de Kok, J. L. Birkby, H. Schwarz, and I. A. G. Snellen
2014. Carbon monoxide and water vapor in the atmosphere of the non-transiting exoplanet HD 179949 b. *A&A*, 565:A124.

Brogi, M., I. A. G. Snellen, R. J. de Kok, S. Albrecht, J. Birkby, and E. J. W. de Mooij
2012. The signature of orbital motion from the dayside of the planet τ Boötis b. *Nature*, 486:502–504.

Brogi, M., I. A. G. Snellen, R. J. de Kok, S. Albrecht, J. L. Birkby, and E. J. W. de Mooij
2013. Detection of Molecular Absorption in the Dayside of Exoplanet 51 Pegasi b? *ApJ*, 767:27.

Brown, T. M., D. Charbonneau, R. L. Gilliland, R. W. Noyes, and A. Burrows
2001. Hubble Space Telescope Time-Series Photometry of the Transiting Planet of HD 209458. *ApJ*, 552:699–709.

Brown, T. M., K. G. Libbrecht, and D. Charbonneau
2002. A Search for CO Absorption in the Transmission Spectrum of HD 209458b. *PASP*, 114:826–832.

Burrows, A., J. Budaj, and I. Hubeny
2008. Theoretical Spectra and Light Curves of Close-in Extrasolar Giant Planets and Comparison with Data. *ApJ*, 678:1436–1457.

Burrows, A., I. Hubeny, J. Budaj, H. A. Knutson, and D. Charbonneau
2007. Theoretical Spectral Models of the Planet HD 209458b with a Thermal Inversion and Water Emission Bands. *ApJ*, 668:L171–L174.

Charbonneau, D., L. E. Allen, S. T. Megeath, G. Torres, R. Alonso, T. M. Brown, R. L. Gilliland, D. W. Latham, G. Mandushev, F. T. O'Donovan, and A. Sozzetti
2005. Detection of Thermal Emission from an Extrasolar Planet. *ApJ*, 626:523–529.

Charbonneau, D., T. M. Brown, D. W. Latham, and M. Mayor
2000. Detection of Planetary Transits Across a Sun-like Star. *ApJ*, 529:L45–L48.

Charbonneau, D., T. M. Brown, R. W. Noyes, and R. L. Gilliland
    2002. Detection of an Extrasolar Planet Atmosphere. *ApJ*, 568:377–384.

Charbonneau, D., H. A. Knutson, T. Barman, L. E. Allen, M. Mayor, S. T.
    Megeath, D. Queloz, and S. Udry
    2008. The Broadband Infrared Emission Spectrum of the Exoplanet HD
    189733b. *ApJ*, 686:1341–1348.

Christiansen, J. L., S. Ballard, D. Charbonneau, N. Madhusudhan, S. Seager, M. J.
    Holman, D. D. Wellnitz, D. Deming, M. F. A'Hearn, and EPOXI Team
    2010. Studying the Atmosphere of the Exoplanet HAT-P-7b Via Secondary
    Eclipse Measurements with EPOXI, Spitzer, and Kepler. *ApJ*, 710:97–104.

Crossfield, I. J. M., H. Knutson, J. Fortney, A. P. Showman, N. B. Cowan, and
    D. Deming
    2012. Spitzer/MIPS 24 μm Observations of HD 209458b: Three Eclipses, Two
    and a Half Transits, and a Phase Curve Corrupted by Instrumental Sensitivity
    Variations. *ApJ*, 752:81.

de Kok, R. J., M. Brogi, I. A. G. Snellen, J. Birkby, S. Albrecht, and E. J. W. de
    Mooij
    2013. Detection of carbon monoxide in the high-resolution day-side spectrum
    of the exoplanet HD 189733b. *A&A*, 554:A82.

de Pater, I. and J. J. Lissauer
    2010. *Planetary Sciences*.

Deming, D., T. M. Brown, D. Charbonneau, J. Harrington, and L. J. Richardson
    2005a. A New Search for Carbon Monoxide Absorption in the Transmission
    Spectrum of the Extrasolar Planet HD 209458b. *ApJ*, 622:1149–1159.

Deming, D., S. Seager, L. J. Richardson, and J. Harrington
    2005b. Infrared radiation from an extrasolar planet. *Nature*, 434:740–743.

Deming, D., A. Wilkins, P. McCullough, A. Burrows, J. J. Fortney, E. Agol,
    I. Dobbs-Dixon, N. Madhusudhan, N. Crouzet, J.-M. Desert, R. L. Gilliland,
    K. Haynes, H. A. Knutson, M. Line, Z. Magic, A. M. Mandell, S. Ranjan,
    D. Charbonneau, M. Clampin, S. Seager, and A. P. Showman
    2013. Infrared Transmission Spectroscopy of the Exoplanets HD 209458b and
    XO-1b Using the Wide Field Camera-3 on the Hubble Space Telescope. *ApJ*,
    774:95.

Désert, J.-M., A. Vidal-Madjar, A. Lecavelier Des Etangs, D. Sing, D. Ehrenreich, G. Hébrard, and R. Ferlet
2008. TiO and VO broad band absorption features in the optical spectrum of the atmosphere of the hot-Jupiter <ASTROBJ>HD 209458b</ASTROBJ>. *A&A*, 492:585–592.

Diamond-Lowe, H., K. B. Stevenson, J. L. Bean, M. R. Line, and J. J. Fortney
2014. New Analysis Indicates No Thermal Inversion in the Atmosphere of HD 209458b. *ApJ*, 796:66.

Fortney, J. J., K. Lodders, M. S. Marley, and R. S. Freedman
2008. A Unified Theory for the Atmospheres of the Hot and Very Hot Jupiters: Two Classes of Irradiated Atmospheres. *ApJ*, 678:1419–1435.

Fortney, J. J., D. Saumon, M. S. Marley, K. Lodders, and R. S. Freedman
2006. Atmosphere, Interior, and Evolution of the Metal-rich Transiting Planet HD 149026b. *ApJ*, 642:495–504.

Fortney, J. J., D. Sudarsky, I. Hubeny, C. S. Cooper, W. B. Hubbard, A. Burrows, and J. I. Lunine
2003. On the Indirect Detection of Sodium in the Atmosphere of the Planetary Companion to HD 209458. *ApJ*, 589:615–622.

Gibson, N. P., S. Aigrain, J. K. Barstow, T. M. Evans, L. N. Fletcher, and P. G. J. Irwin
2013. The optical transmission spectrum of the hot Jupiter HAT-P-32b: clouds explain the absence of broad spectral features? *MNRAS*, 436:2974–2988.

Guillot, T.
2010. On the radiative equilibrium of irradiated planetary atmospheres. *A&A*, 520:A27.

Hoeijmakers, H. J., R. J. de Kok, I. A. G. Snellen, M. Brogi, J. L. Birkby, and H. Schwarz
2015. A search for TiO in the optical high-resolution transmission spectrum of HD 209458b: Hindrance due to inaccuracies in the line database. *A&A*, 575:A20.

Horne, K.
1986. An optimal extraction algorithm for CCD spectroscopy. *PASP*, 98:609–617.

Hubeny, I., A. Burrows, and D. Sudarsky
2003. A Possible Bifurcation in Atmospheres of Strongly Irradiated Stars and Planets. *ApJ*, 594:1011–1018.

Huitson, C. M., D. K. Sing, F. Pont, J. J. Fortney, A. S. Burrows, P. A. Wilson, G. E. Ballester, N. Nikolov, N. P. Gibson, D. Deming, S. Aigrain, T. M. Evans, G. W. Henry, A. Lecavelier des Etangs, A. P. Showman, A. Vidal-Madjar, and K. Zahnle
2013. An HST optical-to-near-IR transmission spectrum of the hot Jupiter WASP-19b: detection of atmospheric water and likely absence of TiO. *MNRAS*, 434:3252–3274.

Kaeufl, H.-U., P. Ballester, P. Biereichel, B. Delabre, R. Donaldson, R. Dorn, E. Fedrigo, G. Finger, G. Fischer, F. Franza, D. Gojak, G. Huster, Y. Jung, J.-L. Lizon, L. Mehrgan, M. Meyer, A. Moorwood, J.-F. Pirard, J. Paufique, E. Pozna, R. Siebenmorgen, A. Silber, J. Stegmeier, and S. Wegerer
2004. CRIRES: a high-resolution infrared spectrograph for ESO's VLT. In *Ground-based Instrumentation for Astronomy*, A. F. M. Moorwood and M. Iye, eds., volume 5492 of *Proc. SPIE*, Pp. 1218–1227.

Knutson, H. A., D. Charbonneau, L. E. Allen, A. Burrows, and S. T. Megeath
2008. The 3.6-8.0 μm Broadband Emission Spectrum of HD 209458b: Evidence for an Atmospheric Temperature Inversion. *ApJ*, 673:526–531.

Knutson, H. A., D. Charbonneau, L. E. Allen, J. J. Fortney, E. Agol, N. B. Cowan, A. P. Showman, C. S. Cooper, and S. T. Megeath
2007a. A map of the day-night contrast of the extrasolar planet HD 189733b. *Nature*, 447:183–186.

Knutson, H. A., D. Charbonneau, A. Burrows, F. T. O'Donovan, and G. Mandushev
2009. Detection of A Temperature Inversion in the Broadband Infrared Emission Spectrum of TrES-4. *ApJ*, 691:866–874.

Knutson, H. A., D. Charbonneau, R. W. Noyes, T. M. Brown, and R. L. Gilliland
2007b. Using Stellar Limb-Darkening to Refine the Properties of HD 209458b. *ApJ*, 655:564–575.

Knutson, H. A., A. W. Howard, and H. Isaacson
2010. A Correlation Between Stellar Activity and Hot Jupiter Emission Spectra. *ApJ*, 720:1569–1576.

Line, M. R., H. Knutson, A. S. Wolf, and Y. L. Yung
2014. A Systematic Retrieval Analysis of Secondary Eclipse Spectra. II. A Uniform Analysis of Nine Planets and their C to O Ratios. *ApJ*, 783:70.

Lockwood, A. C., J. A. Johnson, C. F. Bender, J. S. Carr, T. Barman, A. J. W. Richert, and G. A. Blake
2014. Near-IR Direct Detection of Water Vapor in Tau Boötis b. *ApJ*, 783:L29.

Lord, S. D.
1992. A new software tool for computing Earth's atmospheric transmission of near- and far-infrared radiation. Technical report.

Machalek, P., P. R. McCullough, C. J. Burke, J. A. Valenti, A. Burrows, and J. L. Hora
2008. Thermal Emission of Exoplanet XO-1b. *ApJ*, 684:1427–1432.

Machalek, P., P. R. McCullough, A. Burrows, C. J. Burke, J. L. Hora, and C. M. Johns-Krull
2009. Detection of Thermal Emission of XO-2b: Evidence for a Weak Temperature Inversion. *ApJ*, 701:514–520.

Madhusudhan, N.
2012. C/O Ratio as a Dimension for Characterizing Exoplanetary Atmospheres. *ApJ*, 758:36.

Madhusudhan, N., N. Crouzet, P. R. McCullough, D. Deming, and C. Hedges
2014. H_2O Abundances in the Atmospheres of Three Hot Jupiters. *ApJ*, 791:L9.

Madhusudhan, N., O. Mousis, T. V. Johnson, and J. I. Lunine
2011. Carbon-rich Giant Planets: Atmospheric Chemistry, Thermal Inversions, Spectra, and Formation Conditions. *ApJ*, 743:191.

Madhusudhan, N. and S. Seager
2009. A Temperature and Abundance Retrieval Method for Exoplanet Atmospheres. *ApJ*, 707:24–39.

Madhusudhan, N. and S. Seager
2010. On the Inference of Thermal Inversions in Hot Jupiter Atmospheres. *ApJ*, 725:261–274.

Moses, J. I., N. Madhusudhan, C. Visscher, and R. S. Freedman
2013. Chemical Consequences of the C/O Ratio on Hot Jupiters: Examples from WASP-12b, CoRoT-2b, XO-1b, and HD 189733b. *ApJ*, 763:25.

Nidever, D. L., G. W. Marcy, R. P. Butler, D. A. Fischer, and S. S. Vogt
  2002. Radial Velocities for 889 Late-Type Stars. *ApJS*, 141:503–522.

Öberg, K. I., R. Murray-Clay, and E. A. Bergin
  2011. The Effects of Snowlines on C/O in Planetary Atmospheres. *ApJ*,
  743:L16.

O'Donovan, F. T., D. Charbonneau, J. Harrington, N. Madhusudhan, S. Seager,
  D. Deming, and H. A. Knutson
  2010. Detection of Planetary Emission from the Exoplanet Tres-2 Using
  Spitzer/IRAC. *ApJ*, 710:1551–1556.

Parmentier, V., A. P. Showman, and Y. Lian
  2013. 3D mixing in hot Jupiters atmospheres. I. Application to the day/night
  cold trap in HD 209458b. *A&A*, 558:A91.

Rodler, F., M. Lopez-Morales, and I. Ribas
  2012. Weighing the Non-transiting Hot Jupiter τ Boo b. *ApJ*, 753:L25.

Rothman, L. S., I. E. Gordon, R. J. Barber, H. Dothe, R. R. Gamache, A. Gold-
  man, V. I. Perevalov, S. A. Tashkun, and J. Tennyson
  2010. HITEMP, the high-temperature molecular spectroscopic database.
  J. Quant. Spec. Radiat. Transf., 111:2139–2150.

Schneider, J.
  1994. On the search for O2 in extrasolar planets. *Ap&SS*, 212:321–325.

Seager, S.
  2010. *Exoplanet Atmospheres: Physical Processes*.

Seager, S. and D. Deming
  2010. Exoplanet Atmospheres. *ARA&A*, 48:631–672.

Seager, S. and D. D. Sasselov
  2000. Theoretical Transmission Spectra during Extrasolar Giant Planet Tran-
  sits. *ApJ*, 537:916–921.

Sing, D. K., A. Lecavelier des Etangs, J. J. Fortney, A. S. Burrows, F. Pont, H. R.
  Wakeford, G. E. Ballester, N. Nikolov, G. W. Henry, S. Aigrain, D. Dem-
  ing, T. M. Evans, N. P. Gibson, C. M. Huitson, H. Knutson, A. P. Showman,
  A. Vidal-Madjar, P. A. Wilson, M. H. Williamson, and K. Zahnle
  2013. HST hot-Jupiter transmission spectral survey: evidence for aerosols and
  lack of TiO in the atmosphere of WASP-12b. *MNRAS*, 436:2956–2973.

Snellen, I. A. G., R. J. de Kok, E. J. W. de Mooij, and S. Albrecht
2010. The orbital motion, absolute mass and high-altitude winds of exoplanet HD209458b. *Nature*, 465:1049–1051.

Snellen, I. A. G., R. J. de Kok, R. le Poole, M. Brogi, and J. Birkby
2013. Finding Extraterrestrial Life Using Ground-based High-dispersion Spectroscopy. *ApJ*, 764:182.

Snellen, I. A. G., E. J. W. de Mooij, and S. Albrecht
2009. The changing phases of extrasolar planet CoRoT-1b. *Nature*, 459:543–545.

Southworth, J.
2008. Homogeneous studies of transiting extrasolar planets - I. Light-curve analyses. *MNRAS*, 386:1644–1666.

Spiegel, D. S., K. Silverio, and A. Burrows
2009. Can TiO Explain Thermal Inversions in the Upper Atmospheres of Irradiated Giant Planets? *ApJ*, 699:1487–1500.

Webb, J. K. and I. Wormleaton
2001. Could We Detect O_2 in the Atmosphere of a Transiting Extra-solar Earth-like Planet? *PASA*, 18:252–258.

Zahnle, K., M. S. Marley, R. S. Freedman, K. Lodders, and J. J. Fortney
2009. Atmospheric Sulfur Photochemistry on Hot Jupiters. *ApJ*, 701:L20–L24.

Zellem, R. T., N. K. Lewis, H. A. Knutson, C. A. Griffith, A. P. Showman, J. J. Fortney, N. B. Cowan, E. Agol, A. Burrows, D. Charbonneau, D. Deming, G. Laughlin, and J. Langton
2014. The 4.5 μm Full-orbit Phase Curve of the Hot Jupiter HD 209458b. *ApJ*, 790:53.

3 | The slow spin of the substellar companion GQ Lupi b and its orbital configuration

The spin of a planet or brown dwarf is related to the accretion process, and therefore studying spin can help promote our understanding of the formation of such objects. We present the projected rotational velocity of the young substellar companion GQ Lupi b, along with its barycentric radial velocity. The directly imaged exoplanet or brown dwarf companion joins a small but growing ensemble of wide-orbit, substellar companions with a spin measurement. The GQ Lupi system was observed at high spectral resolution ($R \sim 100\,000$), and in the analysis we made use of both spectral and spatial filtering to separate the signal of the companion from that of the host star. We detect both CO (S/N=11.6) and H_2O (S/N=7.7) in the atmosphere of GQ Lupi b by cross-correlating with model spectra, and we find it to be a slow rotator with a projected rotational velocity of $5.3^{+0.9}_{-1.0}$ km s^{-1}. The slow rotation is most likely due to its young age of < 5 Myr, as it is still in the process of accreting material and angular momentum. We measure the barycentric radial velocity of GQ Lupi b to be 2.0 ± 0.4 km s^{-1}, and discuss the allowed orbital configurations and their implications for formation scenarios for GQ Lupi b.

3.1 Introduction

Measurements of the spin and the orbit of giant extrasolar planets and brown dwarf companions may hold important clues to their origin and evolution. Generally, two formation processes are considered for giant planets: i) core accretion and ii) disk fragmentation. Jupiter and Saturn are commonly accepted to have formed through core accretion. In this class of formation models, gas accretes onto solid planetary embryos of several to ten Earth masses that may have formed beyond the iceline by runaway accretion from kilometer-sized planetesimals (Pollack et al.,

1996; Laughlin et al., 2004; Hubickyj et al., 2005). The discovery of extrasolar giant planets led to the reinvigoration of the disk fragmentation hypothesis, which states that giant (exo)planets may form as a disk gravitational instability that collapses on itself in the outer protoplanetary disk (Boss, 1997, 2000). Disk fragmentation is also considered a potential formation scenario for the more massive brown dwarf companions (Chabrier et al., 2014), or alternatively brown dwarf companions can be the result of prestellar core fragmentation during the earliest stages of the cloud collapse (Jumper and Fisher, 2013).

Spin is predominantly a result of accretion of angular momentum during the formation, and if core accretion and gravitational instability result in differences in spin angular momentum, it is possible this will show up in studies of spin of sub-stellar companions as function of mass. In the solar system, the spin angular momenta of those planets not influenced by tidal effects or tidal energy dissipation by a massive satellite follow a clear relationship, spinning faster with increasing mass (Hughes, 2003). In particular, gas giants far away from their central star are likely to have primordial spin angular momentum, making the directly imaged substellar companions ideal candidates for exploring the connection between formation and spin.

The rotational velocity of an exoplanet was measured for the first time by Snellen et al. (2014), who observed the directly imaged planet β Pictoris b with high-dispersion spectroscopy and measured this planet to have a projected rotational velocity of $v \sin(i) = 25\,\mathrm{km\,s^{-1}}$. Another young directly imaged planet, 2M1207 b, became the first exoplanet to directly have its rotational period measured ($P_{\mathrm{rot}} = 10.7\,\mathrm{h}$), when Zhou et al. (2016) detected rotational modulations with Hubble Space Telescope (HST) photometric monitoring of the object. Both results are in accordance with an extrapolation of the spin-mass trend observed in the solar system planets (see Fig. 3.8).

Apart from being related to the accretion process, the spin of an exoplanet is also a fundamental observable that, in particular, affects its atmospheric dynamics and climate as well as, for example, its magnetic fields. On Earth, the Coriolis effect generates large-scale ocean currents that in turn promote cyclones. For fast rotators, including many brown dwarfs, the wind flows are rotation dominated (Showman and Kaspi, 2013). On the other hand, exoplanets orbiting close to their parent star are expected to be tidally locked. Brogi et al. (2016) and Louden and Wheatley (2015) both recently made use of high-dispersion spectroscopy to detect a Doppler signature in the transmission spectrum of the hot Jupiter HD 189733 b, which is consistent with synchronous rotation. Synchronous rotation is the cause of large temperature differences between the day- and nightside, which in turn can cause fast winds flowing from the hot dayside to the cold nightside.

Another approach to understanding the formation and dynamical evolution of exoplanets is to study their orbits. In the case of directly imaged substellar companions, it is often difficult to constrain the orbits because of the long timescales involved (e.g. Pearce et al., 2015; Ginski et al., 2014a). However, using a high-dispersion slit spectrograph in combination with adaptive optics, it is possible to extract spatially resolved high-dispersion spectra for the companion (Snellen et al., 2014), and thereby measure even very small Doppler shifts due to the orbital motion of the companion. Thus, even just one radial velocity measurement can in some cases prove to be a powerful orbital constraint (Nielsen et al., 2014; Lecavelier des Etangs and Vidal-Madjar, 2016).

In this paper we present both the spin measurement and the barycentric radial velocity (RV) of the widely separated, substellar companion GQ Lupi b as obtained from high-dispersion spectroscopy. We introduce the GQ Lupi system in Section 3.2, and give the details of the observations in Section 3.3. The data analysis is detailed in Section 3.4 with special emphasis on how the spatially resolved spectrum of the companion is extracted and cleaned from telluric and stellar spectral lines. In Section 3.5 we explain the cross-correlation analysis that is employed to measure the rotational broadening and doppler shifts of the molecular lines in the companion spectrum, and the results from the companion are presented in Section 3.6, along with the host star spin and systemic velocity. We discuss the implications of the spin measurement in Section 3.7.1 and the constraints on orbital elements in Section 3.7.2.

3.2   The GQ Lupi system

GQ Lupi A is a classical T Tauri star with spectral type K7 V (Kharchenko and Roeser, 2009) that is located in the star-forming cloud Lupus I (Tachihara et al., 1996) at an approximate distance of 140 ± 50 pc (e.g. Neuhäuser and Brandner, 1998). The system is less than five million years old (Neuhäuser et al., 2005; Seperuelo Duarte et al., 2008; Weise et al., 2010), and there is strong observational evidence for a circumstellar warm dust disk (Hughes et al., 1994; Kessler-Silacci et al., 2006; Morales et al., 2012; Donati et al., 2012), extending to between 25 and 75 au from the star (Dai et al., 2010). The inclination of the spin axis of GQ Lupi A is estimated to be 30° (Donati et al., 2012), which is roughly consistent with the inclination of the warm inner parts of the circumstellar disk determined by Hügelmeyer et al. (2009) to be $\sim$22°. Additional stellar parameters are given in Table 3.1.

The star has a directly imaged substellar companion, GQ Lupi b, with a highly uncertain and model dependent mass most likely in the range $10\,M_J$ to $36\,M_J$,

(Marois et al., 2007; Seifahrt et al., 2007), placing it somewhere on the border between a giant planet and a brown dwarf, although this boundary is becoming increasingly blurred (Chabrier et al., 2014; Hatzes and Rauer, 2015). The exoplanet candidate was first discovered with HST by Neuhäuser et al. (2005), and it was recently imaged as part of the SEEDS survey (Uyama et al., 2016). It is located at a projected separation of 0.7″ west (100 au at 140 pc) and an astrometric analysis by Ginski et al. (2014b) points to a best-fit semimajor axes of $a = 76$ au to 129 au (at 140 pc) and high eccentricity in the range 0.21 to 0.69. The GQ Lupi system has a favourable companion to star contrast ratio, with the host star (Kharchenko and Roeser, 2009) and companion (Ginski et al., 2014b) having K-band magnitudes of 7.1 and 13.3, respectively. Selected parameters for GQ Lupi b are given in Table 3.2.

Table 3.1: Parameters for GQ Lupi A from Donati et al. (2012)

Effective temperature, T_{eff}	4300	$\pm$	50 K
Stellar mass, $M_\star$	1.05	$\pm$	$0.07\,\mathrm{M}_\odot$
Stellar radius, $R_\star$	1.7	$\pm$	$0.2\,\mathrm{R}_\odot$
Surface gravity, $\log g$	3.7	$\pm$	0.2
Rotation period, $P_\star$	8.4	$\pm$	0.3 days
Proj. rot. velocity, $v\sin(i)$	5.0	$\pm$	$1.0\,\mathrm{km\,s^{-1}}$
Inclination, i	30°		

3.3   Observations

We observed the GQ Lupi system for one hour (including acquisition) on 29 May 2014 with the Cryogenic High-Resolution Infrared Echelle Spectrograph (CRIRES; Kaeufl et al., 2004), located at the Nasmyth A focus of the Antu telescope of the Very Large Telescope array (VLT) at Cerro Paranal in Chile. The long slit spectrograph has a slit length of 50″, and we chose a slit width of 0.2″ to achieve the maximal spectral resolving power $R \sim 100\,000$. The slit was positioned in a near east to west orientation to both encompass the host star and the substellar companion located at position angle PA $= -83.6°$ (Zhou et al., 2014), allowing a combination of high-dispersion spectroscopy with high-contrast imaging (Snellen et al., 2015).

We took 18 exposures of 120 s in a classical ABBA pattern, where the telescope was nodded sequentially 10″ in the slit direction between postions A and B, then

B and A to allow accurate background subtraction. At each position an additional small random jitter offset was introduced to minimise issues from flatfielding and hot pixels.

The four CRIRES detectors are of type Aladdin III InSb, and each has a size of 1024×512 pixels with a gap of approximately 280 pixels in between. Unfortunately, the two outer detectors have severe odd-even column non-linearity effects[1], which were not possible to accurately calibrate in these data. These are therefore left out of the analysis. The observations were performed with the standard wavelength settings for order 24 ($\lambda_{cen} = 2.3252\,\mu m$), using the two central detectors to target the ro-vibrational (2, 0) R branch of carbon monoxide. The wavelength range $2.302\,\mu m$–$2.331\,\mu m$ of the two central detectors covers more than 30 strong CO lines.

We used the Multi Application Curvature Adaptive Optics system (MACAO; Arsenault et al., 2003) in $1.0''$ to $1.1''$ seeing conditions. To further maximise the performance of MACAO, the target system was observed at low airmasses between 1.056 and 1.121. This resulted in the starlight being suppressed by a factor ~ 45 at the companion position. With a K-band contrast ratio of 3.3×10^{-3}, the companion contributes with $(F_b/F_A) * 45 * 100 = 15 \pm 3\,\%$ of the total flux at the companion position. The remaining 85% flux is from the host star.

3.4 Data analysis

3.4.1 Basic data reduction

The data was processed with the CRIRES pipeline version 2.3.2 and the corresponding version 3.10.2 of ESOREX. The pipeline performed the basic image processing, i.e. the images were dark subtracted, flatfielded, and were corrected for known bad pixels and non-linearity effects. Furthermore, the pipeline combined the images in AB nodding pairs performing a background subtraction, and extracted a one-dimensional (1D) spectrum from each of these combined images with the optimal extraction technique (Horne, 1986).

We made use of the intermediate data products, i.e. the combined images, and the optimally extracted 1D spectra of the host star as follows. From the 18 exposures, 9 combined image frames were produced for each detector. An example of such a frame for detector 2 is shown in Fig. 3.1. We cut away everything but the central 51 rows that contain the stellar spectral trail, the hidden companion spectral trail (8 pixels above the centre), and enough extra rows to properly de-

---

[1]http://www.eso.org/sci/facilities/paranal/instruments/crires/doc/
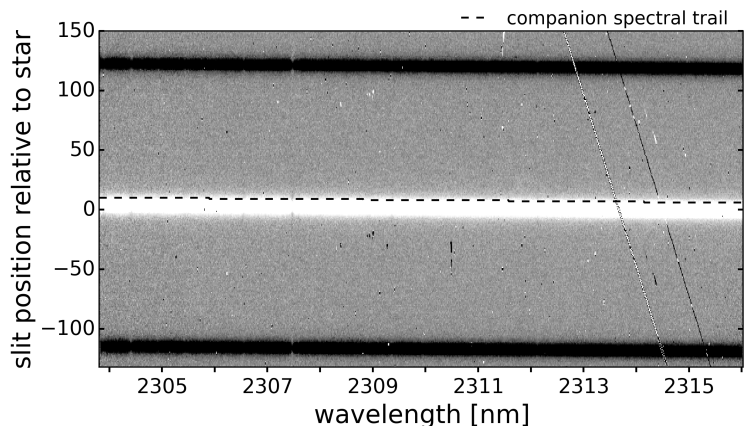VLT-MAN-ESO-14500-3486_v93.pdf

Figure 3.1: One of the combined image frames from detector 2. This is an intermediate data product from the CRIRES pipeline, and it is the combination of an AB nodding pair of exposures. The central rows that are used in the further data analysis are indicated on the right axis. The stellar spectral trail is clearly visible as the central white band, and the location of the hidden spectral trail from GQ Lupi b is indicated with a dashed line. The two diagonal stripes towards the right end are detector defects.

termine the stellar point spread function along the slit. The bad pixel correction in the CRIRES pipeline is insufficient. Therefore the remaining bad pixels (including cosmic rays) were visually identified with the programme DS9, and they were corrected with cubic spline interpolation using the four nearest neighbours in the row on both sides. The 9 optimally extracted 1D spectra of the host star were corrected for bad pixels in the same manner and then median normalised. Subsequently they were averaged over time to a single reference spectrum, representing the average spectrum of the host star, GQ Lupi A, plus telluric absorption in the Earth's atmosphere.

The wavelength calibration was performed using line matching between deep and isolated telluric lines in the reference spectrum and a synthetic transmission spectrum from ESO SkyCalc[2]. We used 15 to 20 lines per detector and fitted a second-order polynomial to the pairs of pixel and wavelength centroids, where the centroids were determined from Gaussian fits. The highest residuals to the second-order polynomial fits were at a level of 20% of a pixel.

---

[2]https://www.eso.org/observing/etc/skycalc/
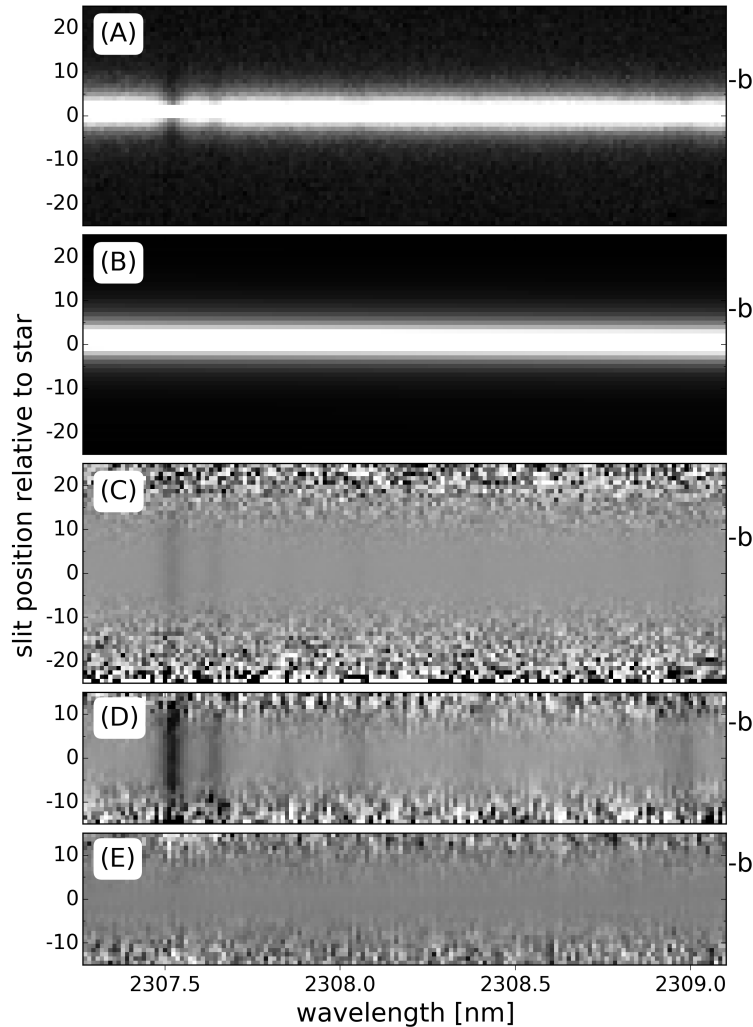
Figure 3.2: Illustration of the data analysis steps from a short wavelength range from detector 2. The y-axis depicts the slit position relative to the star, with the slit position of the companion indicated by a 'b' on the right-hand axes. The greyscales were adjusted individually for each array with an IRAF-like z-scale algorithm. Top to bottom: (A) the AB-combined image corrected for bad pixels, (B) the spatial profiles of the star, (C) the image after each row has been normalised with the rows of the spatial profile array, (D) the spatial spectra (i.e. rectified for the trace), and (E) the residual spatial spectra after removing stellar and telluric lines.

3.4.2   Extraction of spectra for each slit position

From the clean combined image frames (Fig. 5.2A), we optimally extracted a spectrum for each slit position. Fig. 5.2 illustrates the procedure, which was performed individually for each frame and each detector. Looking at the star trail in Fig. 3.1, it can be seen that the y-position of the intensity peak shifts with wavelength, and it is an important step in the data analysis to correct for this tilt of the trail of the star. In detector 2, the pixel with the maximum intensity shifts by 4 pixels from one end of the detector to the other, and in detector 3 the shift is 2 pixels. The tilted trail introduces a curvature in the continuum for a given row, and therefore we normalised each row with a polynomial fit of the curvature, where the degree of the polynomial depended on the distance from the stellar spectral trail. The fitted curves also provide the spatial profiles of the star as a function of wavelength (Fig. 5.2B). We used the spatial profiles to optimally extract a spectrum for each of the 31 most central rows from the normalised arrays (Fig. 5.2C). We refer to these collectively as the spatial spectra (Fig. 5.2D). The nine AB frames of spatial spectra were combined to a single frame to increase the signal-to-noise ratio of a given spectrum. Each pixel was normalised by the median of the pixel value through the nine frames and then combined as a weighted average. The weights were determined according to the varying width of the spatial profile (Fig. 5.2B), which is a seeing proxy. Pixels that deviated $> 4\sigma$ for the given pixel position were excluded.

3.4.3   Removal of telluric and stellar spectrum

The spatial spectra are dominated by the telluric absorption and the stellar spectrum, which has prominent CO lines. In contrast, the additional component to the spectra from the companion is strongly localised on the detector at the slit position of the companion. The stellar and telluric components are quasi identical at all slit positions, although the spectral resolution changes slightly with slit position. This is due to variations in the spatial profile of the star along the slit. Furthermore a small offset of the position of the star with respect to the centre of the slit can result in a small wavelength offset, and in addition there is a scaling factor. In order to remove both the telluric and stellar components, we made use of the reference spectrum we constructed in Section 3.4.1. The reference spectrum was adjusted to each slit position to correct for the above-mentioned effects by convolving with an appropriate broadening function, which was determined with the singular value decomposition technique (Rucinski, 1999). The telluric and stellar spectrum was then removed from the spatial spectra by dividing with the adjusted reference spectrum (Fig. 5.2E).

Companion position

The presence of CO lines in the spectrum of the host star is a complicating factor because they potentially overlap with the CO lines of the companion. If the orbital motion of the companion has a significant radial component, the lines are red- or blueshifted relative to the lines of the star, but because of the wide separation between host and companion in the GQ Lupi system, the upper limit on the absolute value of this shift is 2.5 to 3.5 km s^{-1}, depending on the exact semimajor axis and mass of GQ Lupi A. Furthermore, both the molecular lines of the companion and of the host star are rotationally broadened. Guenther et al. (2005) measured the projected rotational velocity of GQ Lupi A to be 6.8 ± 0.4 km s^{-1}, and more recently Donati et al. (2012) found a similar value of 5 ± 1 km s^{-1}. The concern is that the shape and strength of the companion lines may be affected by the process of removing the stellar lines, thereby compromising the $v \sin(i)$ and/or Doppler shift measurements.

The severity of this issue is greatly reduced by the angular separation between the host and the companion of $0.7''$. As stated in section 3.3, we achieved a suppression of the starlight at the position of the companion to a few percent, which means that 15% of the total flux at this slit position originates from the companion and 85% originates from the host star. We therefore scaled the stellar lines in the reference spectrum down by 15% before proceeding as described in section 3.4.3 with removing the stellar and telluric spectrum from the spatial spectrum of the companion position.

We isolated the stellar lines from the telluric parts of the reference spectrum to rescale the stellar reference spectrum. This was carried out as an iterative process, where a telluric model spectrum and a stellar model spectrum were fitted and removed separately from the reference spectrum. The steps were as follows:

- We used the same telluric model spectrum from ESO SkyCalc, which was used to perform the wavelength calibration. The airmass and the precipitable water vapor (PWV) was set manually at airmass 1.1 and PWV 1.5 to best fit the observed reference spectrum. The stellar model is a PHOENIX spectrum from Husser et al. (2013) with $T_{\text{eff}} = 4300$ K and $\log g = 3.5$. The telluric model was smoothed, and both the telluric and the stellar model were resampled to the observed wavelength solution.

- We convolved the telluric model with a broadening kernel to adjust the resolution to that of the reference spectrum. As in section 3.4.3 the singular value decomposition (SVD) technique (Rucinski, 1999) was employed to determine the appropriate kernel, but here it was performed in log space to avoid the deepest telluric lines from dominating. The telluric spectrum was

then removed from the reference spectrum by dividing by the telluric fit.

- The stellar template was fitted to the telluric-removed reference spectrum by convolving with an SVD broadening kernel in log space. Following this, the stellar lines were removed from the original reference spectrum by dividing by the stellar fit.

- The telluric SVD fit and removal was redone, adjusting the telluric model to the stellar-removed reference spectrum before dividing the original reference spectrum by the fit, thus producing an improved telluric-removed reference spectrum.

- The continuum of the new telluric-removed reference spectrum was fitted with a second order polynomial and removed. Subsequently the stellar SVD fit was redone, fitting the stellar model to the flat telluric-removed reference spectrum. This stellar fit was then scaled to 15% of the line strength, and the original reference spectrum was divided by this scaled down stellar model, resulting in a reference spectrum with the strength of the stellar lines reduced by 15%.

The effects of scaling down the stellar lines are minor. Details of how it affects the measured $v \sin(i)$ and RV are given in Section 3.7.1 and Section 3.7.2.

3.5   Measuring the signal from the companion

After removing the telluric and stellar spectrum, the residual spatial spectra consist of residual noise, with the exception at the slit position of the companion, which also has a contribution from the companion spectrum. Fig. 5.2E shows a short wavelength range of the residual spatial spectra. At the high spectral resolution of the CRIRES data, the molecular bands are resolved into individual lines, and the signal from all of the lines from a given molecule within the wavelength range can be combined through cross-correlation with a model spectrum. Molecules are identified in the spectrum of the companion as a peak in the cross-correlation function (CCF). The CCF profile is sensitive to both the shape and the Doppler shift of the companion spectral lines. Lines that are broadened by rotation result in broadened CCF profiles, and lines that are shifted also shift the peak of the CCF. In this section we describe the model spectra and the cross-correlation analysis, as well as the procedure for measuring the rotation and radial velocity of the companion from the cross-correlation function.
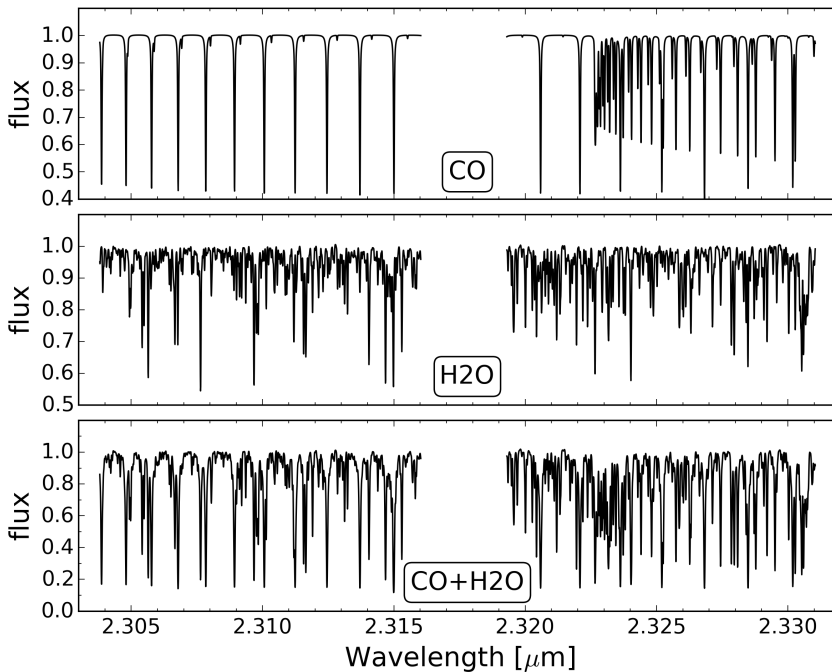
Figure 3.3: Models with a T/p profile and abundance that give rise to the strongest cross-correlation signals from the companion. The top panel shows the model with CO as a single trace gas, the middle panel the model with only H_2O, and the bottom panel model contains both CO and H_2O. The temperature is set to decrease from 2150 K at 1 bar to 1100 K at 0.03 bar and is isothermal outside this pressure range. The volume mixing ratios for CO and/or H_2O in these three models are 10^{-4}.

3.5.1 The model spectra

The GQ Lupi system is thought to be very young (<5 Myr), and as a result GQ Lupi b is very hot with an effective temperature (T_{eff}) of approximately 2650 K (Seifahrt et al., 2007). At such high temperatures the most abundant trace gas molecules in the K band are expected to be CO and H_2O. We cross-correlated with models with CO or H_2O as a single trace gas and with a suit of models containing both CO and H_2O. The models were calculated line by line, assuming H_2-H_2 collision-induced absorption (Borysow et al., 2001; Borysow, 2002). The CO and H_2O data were taken from HITEMP 2010 (Rothman et al., 2010) and a Voigt line profile was employed.

The models were constructed from a narrow grid of parameterised temperature-pressure profiles (T/p profiles). All the models are isothermal with a temperature

Figure 3.4: The residual spectrum after removing telluric and stellar lines at the companion position. Overplotted in red is the CO model from the top panel of Fig. 3.3, convolved to the CRIRES resolution, rotationally broadened, and Doppler shifted 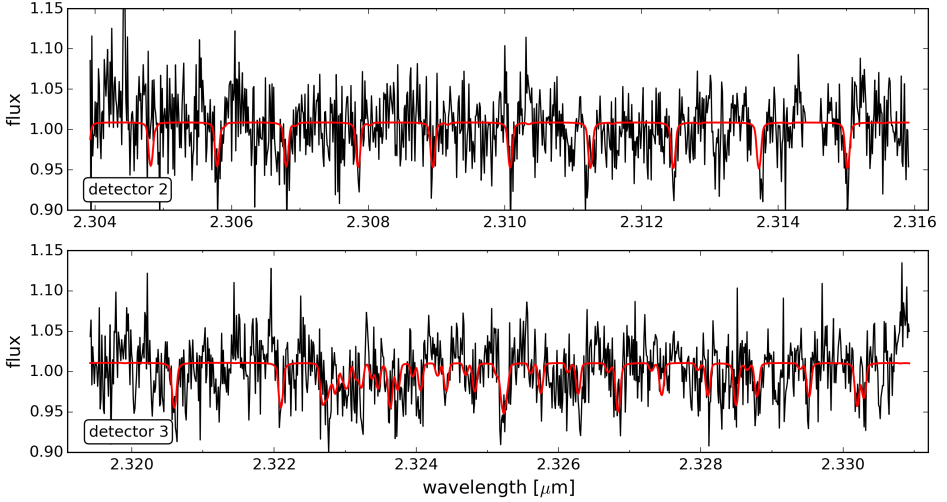to match the measured $v \sin i$ (5.3 km s^{-1}) and radial velocity (2 km s^{-1}) of GQ Lupi b. For illustration purposes, the model was also fitted to the residual companion spectrum with a vertical offset and a scaling factor. The companion spectrum is dominated by noise, but the individual CO lines are discernible.

of T_0 = [1650 K, 1900 K, 2150 K] at pressures higher than p_0 = 1 bar. The temperature decreases with a constant lapse rate (i.e. the rate of temperature change with log pressure) until it reaches T_1 = [750 K, 1100 K, 1450 K, 1800 K] at pressure p_1 = [10$^{-1.5}$ bar, 10$^{-2.5}$ bar, 10$^{-3.5}$ bar, 10$^{-4.5}$ bar]. The models are isothermal again at higher altitudes or equivalently lower pressures. Both CO and H$_2$O were tested with four different volume mixing ratios, VMR = [10$^{-5.5}$, 10$^{-5.0}$, 10$^{-4.5}$, 10$^{-4.0}$]. Fig. 3.3 illustrates the CO-only, H$_2$O-only and CO+H$_2$O models with the best T/p profile and volume mixing ratios from the grid.

3.5.2   Cross-correlation analysis

The model spectrum was first convolved to the CRIRES spectral resolution using a Gaussian filter, then Doppler shifted over the range -250 to 250 km s^{-1} in steps of 1.5 km s^{-1}, and for each velocity step cross-correlated with the residual spatial spectra. We assumed R = 100 000 for the instrumental profile, but we measured the actual resolving power to be in the range 80 000 to 90 000. This causes a small overestimation of $v \sin(i)$ of the order of 60 m s^{-1}, which is included in the lower uncertainty bound of the final result. The cross-correlation was performed for every

slit position as a means to investigate the strength of spurious signals and issues with, for example stellar residual signals. Each detector was treated separately and only combined as an average after the cross-correlation analysis. This results in two-dimensional arrays with the cross-correlation coefficient as a function of slit position and applied Doppler shift.

3.5.3   Measuring the companion $v \sin(i)$ and RV

The cross-correlation function (CCF) from the residual spectrum at the companion position using any of the models contains the rotational broadening and radial velocity of the companion. We selected the model with the strongest cross-correlation signal for the purpose of measuring $v \sin(i)$ and RV. The CCFs from the two detectors were averaged to further maximise the signal-to-noise (S/N). We refer to the average CCF from the companion position and the best model as the measured companion CCF.

   We determined the best-fit $v \sin(i)$ and RV of the measured companion CCF through $\mathcal{X}^2$ minimisation with a suite of model CCFs, along with confidence intervals from rescaling the errors so $\bar{\mathcal{X}}^2 = 1$. The model CCFs were constructed by cross-correlating the non-broadened best model with broadened and shifted versions of the model itself. Both the broadened and non-broadened models were convolved to the CRIRES spectral resolution prior to the cross-correlation. We tested projected rotational velocities in the range 0 to $10 \, \mathrm{km \, s^{-1}}$ and Doppler shifts in the range -5 to $5 \, \mathrm{km \, s^{-1}}$. For both parameters the step size was $0.1 \, \mathrm{km \, s^{-1}}$. Each of these model CCFs were then offset (y-direction) and scaled with a least-squares fit to best match the measured companion CCF, after which the $\mathcal{X}^2$ minimisation routine was performed. The measured radial velocity was corrected to the barycentric radial velocity using the systemic velocity (v_{sys}) determined from the host star spectrum as described in Section 3.5.4, and the heliocentric correction term for the time of observation. The results are presented in Section 3.6.2 and discussed in Sections 3.7.1 and 3.7.2.

3.5.4   Measuring the systemic velocity and the host star $v \sin(i)$

We took the same approach to measuring $v \sin(i)$ and RV of the host star as we did for the companion. In this case, the measured host star CCF was the cross-correlation function of the flat telluric-removed reference spectrum from the final step of Section 3.4.3 and a synthetic PHOENIX spectrum from Husser et al. (2013) with $T_{\mathrm{eff}} = 4300 \, \mathrm{K}$ and $\log g = 3.5$. A suite of model CCFs were constructed from the PHOENIX model with a range of $v \sin(i)$ and RV values, and we performed the $\mathcal{X}^2$ analysis for the host star, comparing the measured and modelled

CCFs. The measured radial velocity was corrected to the barycentric radial velocity (i.e. the systemic velocity) using the heliocentric correction term for the time of observation. We carried out this analysis for PHOENIX models with $T_{\text{eff}} \pm 100$ K and $\log g \pm 0.5$ to test the sensitivity to the stellar parameters, and found that this temperature difference can affect the radial velocity with up to 100 m s^{-1} and the $v \sin(i)$ with up to 200 m s^{-1}. The radial velocity is not sensitive to the choice of $\log g$, but the $v \sin(i)$ can be affected by up to 200 m s^{-1}. The results are presented and discussed in Sections 3.6.3 and 3.7.3, respectively.

3.6   Results

Although the residual spectrum at the companion position is noisy, the absorption lines from CO in the companion atmosphere are in some cases visible (Fig. 4.4). To help guide the eye, we overplotted the best CO model shifted to the best-fit radial velocity. Although we can visually detect the individual CO lines, the companion spectrum is too noisy to allow the rotational broadening or the Doppler shift to be measured directly from the CO lines, and we therefore need to make use of the CCF.

3.6.1   Detection of CO and H_2O

We clearly detect the substellar companion at the expected distance from the host star ($0.7''$) in the CCF arrays (see Fig. 3.5). We detect CO with a S/N of 11.6 and H_2O with a S/N of 7.7. The best model containing both CO and H_2O is detected with a S/N of 12.3. These are average values from the two central CRIRES detectors, but both CO and H_2O are detected separately in each detector. The S/N values were obtained by dividing the cross-correlation coefficients with the standard deviation of the array, excluding points in parameter space that are close to the companion signal. Fig. 3.5 shows the S/N cross-correlation arrays for the best CO-only, H_2O-only and CO+H_2O models from the tested T/p and VMR grid. These arrays are displayed here from -50 to 50 km s^{-1}, but the S/N-values are based on the standard deviation of the full radial velocity range from -250 to 250 km s^{-1}. These best models are illustrated in Fig. 3.3 and share the same T/p profile with the temperature decreasing from 2150 K at 1 bar to 1100 K at 0.03 bar. The steep decrease in temperature relatively deep in the atmosphere gives rise to strong absorption lines. The VMR for both CO and H_2O in these models are in all cases 10^{-4}. All the models in the grid described in Section 3.5.1 give rise to significant molecular detections, and for a given VMR the significance of a detection from the different T/p profiles agree to within 1σ.

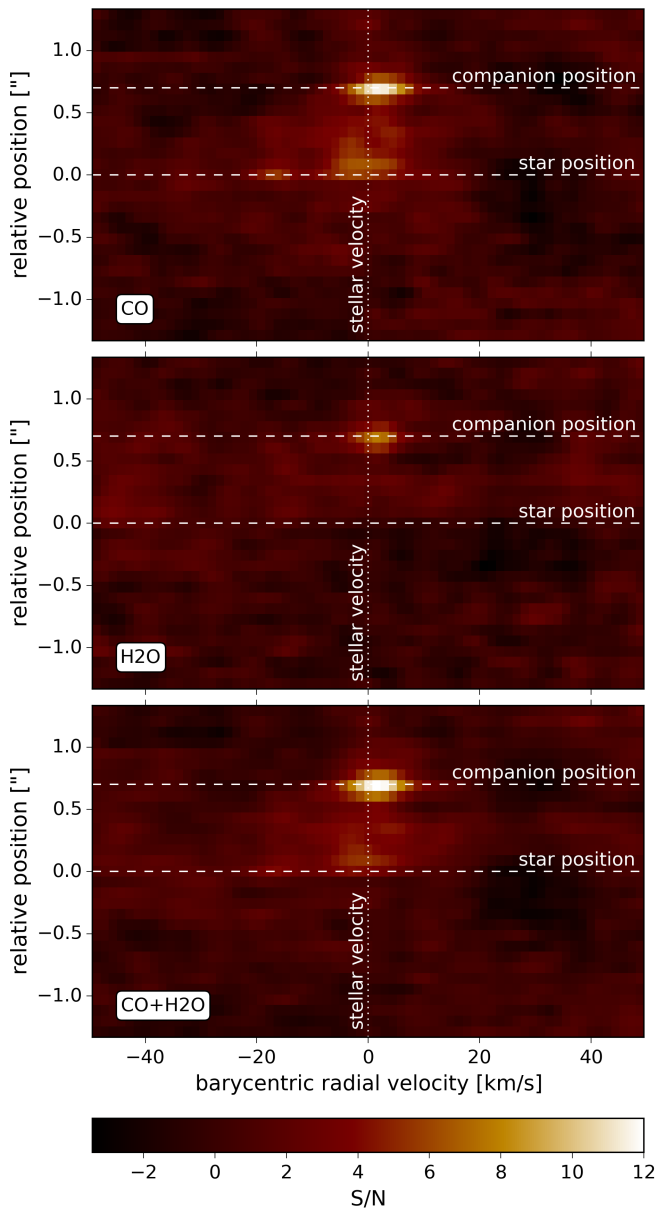**Figure 3.5:** Strength of the cross-correlation as function of slit position and radial velocity for the three best-fit models (see Fig. 3.3). We detect both CO and H_2O using single-trace gas models with a S/N of 11.6 for CO and 7.7 for H_2O, and the signal from the double-trace gas model is marginally stronger with a S/N of 12.3. These cross-correlation arrays are the averages from the two central CRIRES detectors.

The CO signal and the CO+H$_2$O signal are detected with a stronger significance in detector 3 compared to detector 2. This is in line with expectations because the third detector has a higher number of CO lines. In detector 3 there are stellar CO residuals in the row just above the star position, although at a lower level than the companion signal. The residuals are strong enough to also show up in the average cross-correlation arrays in Fig. 3.5. It is unclear why the procedure for removing the stellar light has partly failed at this one slit position, and also why the issue only involves one of the detectors. The companion is a further 7 pixels away where the light from the star is decreased to only $\sim 2\%$ of its peak intensity, so we expect this issue to have negligible effect on the $v \sin(i)$ and RV measurements.

3.6.2   Companion $v \sin(i)$ and RV

It is already clear from the Fig. 3.5 cross-correlation arrays that the companion signal is quite narrow, and that it is redshifted relative to the stellar radial velocity by only a small amount. The measured companion CCF is shown in Fig. 3.6 together with the best-fit model CCF, and the CCF for the same model, but without rotational broadening. We find from the $\mathcal{X}^2$ minimisation routine that the projected rotational velocity of GQ Lupi b is $5.3^{+0.9}_{-1.0}\,\mathrm{km\,s^{-1}}$ and its barycentric radial velocity is $2.0 \pm 0.4\,\mathrm{km\,s^{-1}}$.
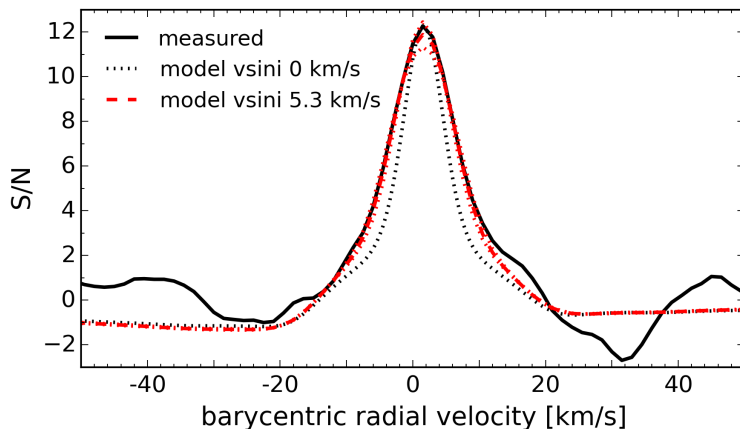
Figure 3.6: The measured companion cross-correlation function (CCF) is best fit by a CO + H$_2$O model CCF, which is redshifted $2.0\,\mathrm{km\,s^{-1}}$ and rotationally broadened by $5.3\,\mathrm{km\,s^{-1}}$. For comparison we also show the model CCF without rotational broadening for which the width is dominated by the spectral resolution of the CRIRES instrument.

3.6.3   Host star $v\sin(i)$ and v_{sys}

As a by-product of the analysis carried out in this work, we have estimates of the systemic velocity and the projected rotational velocity of GQ Lupi A. The systemic velocity is of direct importance as it is required to translate the measured companion RV to the barycentric frame. We find $v_{sys} = -2.8 \pm 0.2 \, \mathrm{km \, s^{-1}}$. For the host star, we measured a rotational broadening corresponding to $v\sin(i) = 6.8 \pm 0.5 \, \mathrm{km \, s^{-1}}$. However, we have not taken additional broadening terms (e.g. macro-turbulence) into account when determining $v\sin(i)$ of GQ Lupi A.
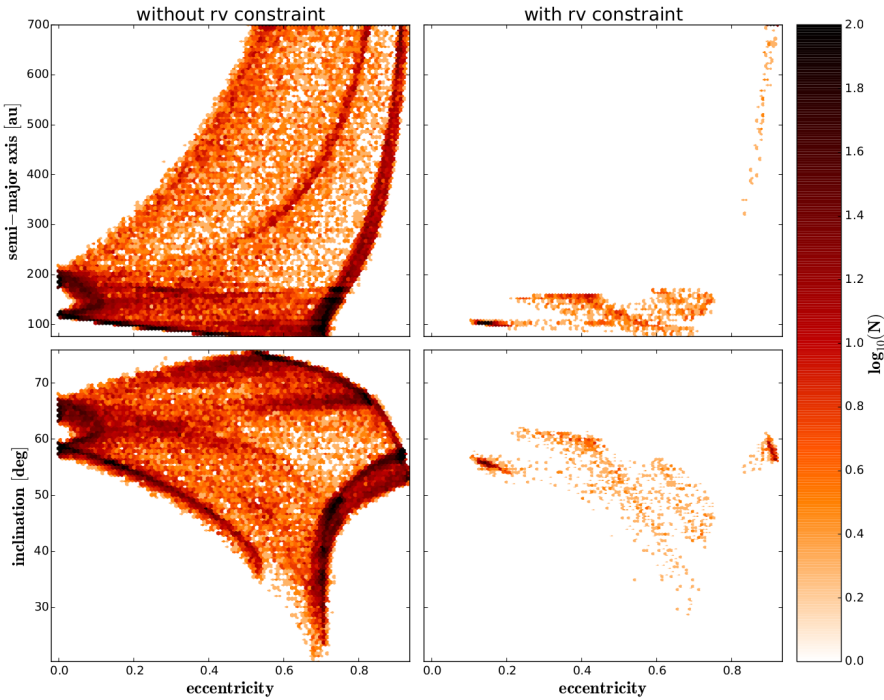
Figure 3.7: Orbital parameters as function of eccentricity for the substellar companion GQ Lupi b around its host star with the colour scale indicating the logarithmic density of solutions. The panels in the left column are reproduced from Ginski et al. (2014b) and they show the 1% best-fitting solutions out of 5 000 000 runs of their LSMC fit. The right-hand panels show the orbital solutions, which are consistent with the radial velocity measurement from this work.

3.6.4   Orbital constraints for GQ Lupi b

The radial velocity measurement of $2.0 \pm 0.4\,\text{km\,s}^{-1}$ can be used to constrain the orbit of GQ Lupi b. We approached this by applying the radial velocity as a constraint to the best-fitting orbital solutions from Ginski et al. (2014b). They applied astrometry to 15 astrometric epochs from VLT and HST spanning a time frame of 18 years to determine the angular separation and relative position angle. They applied least-squares Monte Carlo (LSMC) statistics to constrain the orbit. The details of the LSMC approach, along with a comparison to the more widely used Markov chain Monte Carlo (MCMC) approach, are described in Ginski et al. (2013). The mass of the host star was assumed to be $0.7 M_\odot$, and the distance to the system 140 pc. The left-hand panels of Fig. 3.7 are a reproduction of Ginski et al. (2014b) Fig. 5a and 5b. The orbital solutions in this figure represent the 1% best-fitting solutions out of 5 000 000 LSMC runs. Dismissing the solutions from this best-fitting subset that are inconsistent with the new radial velocity measurement produces the right-hand panels of Fig. 3.7.

The new radial velocity constraint dramatically reduces the number of possible solutions, and certain families of orbital solutions are excluded. In particular, the observations no longer support long-period orbits ($a > 185$ au) with eccentricities below 0.8, or circular orbits.

The remaining allowed solutions fall into three different families:

1. Orbits with a semimajor axis ~ 100 au, inclination $\sim 57°$, and eccentricity ~ 0.15

2. Orbits with a semimajor axis < 185 au, a range of eccentricities $0.2 < e < 0.75$, and inclinations $28° < i < 63°$

3. Highly eccentric, long-period orbits with a semimajor axis > 300 au, eccentricities > 0.8, and high inclinations $52° < i < 63°$

3.7   Discussion

3.7.1   The slow spin of GQ Lupi b

The CO and H_2O lines in the spectrum of GQ Lupi b are narrow, with only a moderate rotational broadening corresponding to a projected rotational velocity of $5.3^{+0.9}_{-1.0}\,\text{km\,s}^{-1}$. This strongly suggests that GQ Lupi b is a slow rotator when compared to the giant planets in the solar system or the recent spin measurements of β Pictoris b and 2M1207 b (see Table 3.2 and Fig. 3.8).

The $v \sin(i)$ measured for GQ Lupi b could have been influenced by the removal of the stellar lines, for example, by removing too much of the CO, which actually originates from the companion and not from the star. This removal could have over-subtracted the short-wavelength wing of the companion signal, thereby making it more narrow. We compared the widths of the CO+H$_2$O signal for the analyses with and without rescaling the stellar CO and found $5.3^{+0.9}_{-1.0}$ km s^{-1} and 4.8 ± 1.0 km s^{-1}, respectively. This suggests that the influence in any case is only minor and cannot have resulted in the $v \sin(i)$ of the companion to be artificially small. The measured companion CCFs for the two cases are plotted together in Fig. 3.9.

Micro- and macro-turbulence act as additional broadening of line profiles and can therefore cause an overestimation of the projected rotational velocity. Wende et al. (2009) investigated the effective temperature and $\log g$ dependence of the velocity field for M stars extending to temperatures as low as 2500 K, thereby just covering the estimated temperature of GQ Lupi b. Micro- and macro-turbulent velocities decrease with lower effective temperatures and, in particular, micro-turbulence increases towards lower surface gravities. Assuming a surface gravity for GQ Lupi b in the range $\log g = 3.0$ to 4.2, a realistic upper limit for the sum of the squares of the turbulent velocities is 1.5 km s^{-1}, corresponding to an over-estimate of $v \sin(i)$ by 0.22 km s^{-1}. We included this in the lower bound of the uncertainty estimate of the $v \sin(i)$ measurement.

If the orientation of the spin axis is edge-on, the measured spin velocity corresponds to a rotational period of 82 hr, assuming a companion radius of $3.5^{+1.5}_{-1.03} R_{\rm J}$ (Seifahrt et al., 2007). Since the spin axis orientation is unknown, it could possibly be nearly pole on. Therefore the equatorial rotation velocity ($v_{\rm eq}$) could be much higher than $v \sin(i)$. However, the inclination of the axis of rotation would have to be less than 15° to make the spin of GQ Lupi b comparable to β Pic b or the solar system giant planets. Assuming a random orientation, this has only a probability of 3.4%. If we make the assumption that orbital and spin axes are aligned, then based on Fig. 3.7 we can rule out inclinations below 28°, corresponding to $v_{\rm eq}$ faster than 11.3 km s^{-1}. This is still well below the $v \sin(i)$ of 25 km s^{-1}, which Snellen et al. (2014) measured for β Pic b. Therefore, it is unlikely that GQ Lupi b is a fast rotator.

The slow rotation of GQ Lupi b may be caused by a different formation path from β Pic b, 2M1207 b, and the giant planets in the solar system. GQ Lupi b at $\sim$100 au is significantly further away from its host star than the other mentioned planets. In addition it is likely more massive with a mass range 10 M$_{\rm J}$ to 36 M$_{\rm J}$ extending well into the brown dwarf regime. It could therefore have formed through either disk gravitational instability or even fragmentation of the collapsing

Table 3.2: Comparison of key parameters of the three substellar companions with spin measurements.

	proj. dist.	mass	radius	age	Teff	$v \sin(i)$ or v_{eq}
GQ Lup b[1−3]	100 au	$25^{+11}_{-15}\,M_J$	$3.5^{+1.5}_{-1.03}\,R_J$	< 5 Myr	2650 ± 100 K	$5.3^{+0.9}_{-1.0}$ km s^{-1}
2M1207 b[4−5]	46 au	$5 \pm 3\,M_J$	-	8 Myr	1230 ± 310 K	17.3 ± 1.5 km s$^{-1}\star$
β Pic b[6−9]	6 − 9 au	$11 \pm 5\,M_J$	$1.65 \pm 0.06\,R_J$	21 ± 4 Myr	1600^{+50}_{-25} K	25 ± 3 km s^{-1}

1) Ginski et al. (2014b), 2) Seifahrt et al. (2007), 3) This work, 4) Song et al. (2006), 5) Zhou et al. (2016) 6) Lecavelier des Etangs and Vidal-Madjar (2016), 7) Binks and Jeffries (2014), 8) Currie et al. (2013), 9) Snellen et al. (2014). $\star$ The spin of 2M1207 b is the equatorial rotation velocity based on $P_{rot} = 10.7^{+1.2}_{-0.8}$hr from Zhou et al. (2016) and assuming $R = 1.5\,R_J$ consistent with evolutionary models.

proto-stellar core, rather than through core accretion, which is a possible common formation path for the (exo)planets showing the spin-mass trend that we see in Fig. 3.8. Allers et al. (2016) have recently measured the projected rotational velocity of PSO J318.5338-22.8603, which is a free-floating planetary mass member of the β Pictoris moving group with an estimated age of 23 ± 3 Myr. Their measured $v \sin(i) = 17.5^{+2.3}_{-2.8}$km s^{-1} is also consistent with the solar system spin-mass trend. Such an object is most likely the result of gravitational instability (Chabrier et al., 2014; Stamatellos, 2014), possibly followed by photo-erosion, but it could also have been dynamically kicked out of an orbit around a star, and core accretion can therefore not be ruled out. Low resolution spectra of GQ Lupi b are consistent with a spectral type of late M to early L (Neuhäuser et al., 2005), and comparable brown dwarf binaries and field brown dwarfs from the literature show a wide variety of rotational velocities and no simple correlation with mass (Konopacky et al., 2012; Zapatero Osorio et al., 2006; Metchev et al., 2015; Scholz et al., 2015). Most brown dwarfs are rapid rotators ($v \sin(i) > 10$ km s^{-1}), and their minimum rotation rates are a function of their spectral types with the higher mass objects rotating more slowly than their lower mass counterparts, in contrast with the planetary trend. This is because magnetic breaking plays an increasing role in the more massive brown dwarfs. However, it is much too early to make any claims about relations between spin, mass, and orbital distance based on the limited observations; this is the case in particular because there is another very probable explanation for the slow spin of GQ Lupi b.

We believe that the slow spin of GQ Lupi b is linked to its young age. All current estimates set the age of the GQ Lupi system to < 5 Myr, and Neuhäuser et al. (2005) estimated the age to be only 1 ± 1 Myr. In fact, observational evidence exists of GQ Lupi b actively accreting, through the detection of Paβ emission (Seifahrt et al., 2007) and the detection of Hα in emission together with excess optical continuum emission (Zhou et al., 2014). This means that a significant amount of angular momentum could still be accreted in the future. Furthermore,
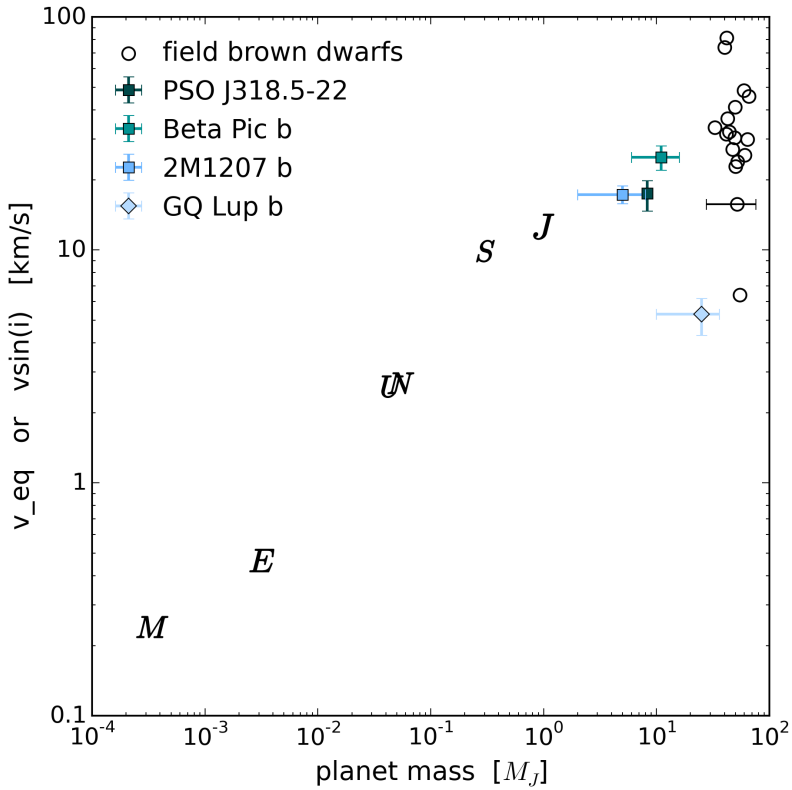
Figure 3.8: Spin as function of mass for extrasolar substellar companions and solar system planets, together with the free-floating planetary mass object PSO J318.5-22 and field brown dwarfs. The solar system planets and 2M1207 b have equatorial rotation velocities and β Pictoris b and GQ Lupi b have projected rotation velocities, as does PSO J318.5-22. Mercury and Venus are not included in the plot because their proximity to the Sun has caused their spin to be dominated by tidal interactions with the Sun. For comparison, field brown dwarfs with estimated masses and either a rotational period measurement or $v\sin(i)$ measurement are shown as empty circles, with the typical uncertainty in mass indicated for a single object. Their masses and radii are from Filippazzo et al. (2015), rotational periods are from Metchev et al. (2015), and $v\sin(i)$'s are from either Zapatero Osorio et al. (2006) or Blake et al. (2010). The field brown dwarfs are much older than the substellar companions and PSO J318.5-22 with highly uncertain ages in the range 500 Myr to 10 Gyr.

its radius is now estimated at $3.5^{+1.5}_{-1.03}\,R_J$ (Seifahrt et al., 2007), meaning that even without extra accretion it is still expected to contract significantly to $\sim 1\,R_J$ radius and spin up to $10 - 25\,\text{km s}^{-1}$. This would bring it much nearer the mass-spin relation of the other giant planets. In this context, it is interesting that 2M1207 b, with an age in between that of GQ Lupi b and β Pic b, is also seen to have an intermediate spin.

The spin angular momenta of brown dwarfs and low-mass stars also evolve over time (Bouvier et al., 2014; Irwin et al., 2011; Newton et al., 2016; Scholz et al., 2015). Analogously to the spin evolution of giant planets, gravitational contraction causes the brown dwarfs to spin up, but after 10 Myr to 100 Myr magnetic breaking starts dominating the spin evolution. The angular momentum loss mechanisms are more inefficient for smaller and cooler objects (Reiners and Basri, 2008). This stands in contrast to planets, which are expected to retain their spin angular momenta, unless they are gravitationally disturbed by a third object.

Measurements of spin as a function of mass, orbital distance, and crucially, age, for numerous substellar companions and free-floating low-mass objects, are necessary to determine the effects of formation pathways on spin-mass relationships. Yet at this early stage, every spin measurement of a substellar companion is likely to lead to new insights.

3.7.2   The orbital orientation of GQ Lupi b

We used the radial velocity measurement for GQ Lupi b of $2.0 \pm 0.4\,\text{km s}^{-1}$ in conjunction with previous astrometry from Ginski et al. (2014b) to constrain its orbital elements. This allows us to rule out both circular orbits and long-period orbits ($a > 185$ au) with eccentricities below 0.8. If we allow for a larger uncertainty in the astrometry, then circular orbits with inclinations $60° < i < 78°$ are still possible. The orbital solutions that are consistent with the RV measurement show a degeneracy between eccentricity and inclination. Orbits with a relatively low eccentricity ($0.1 < e < 0.4$) have high inclinations $48° < i < 63°$, which are distinctly different from that of the circumstellar disk ($\sim$22°). In the case of the more eccentric solutions $0.4 < e < 0.75$, the inclinations are less well constrained, yet there is a tendency towards allowing for smaller inclinations towards higher eccentricities. This includes orbits with $0.65 < e < 0.7$ that are nearly aligned with the circumstellar disk. Finally we have a subset of orbital solutions with extremely wide orbits (a > 300 au) and high eccentricities $e > 0.8$. This last subset seems less likely because it would imply that we observe the companion at a special moment near periastron. All solutions shown in the right column of Fig. 3.7 fit both our new radial velocity measurement and the available astrometric data well and the density of solutions does not correspond directly to the likelihood of solutions.

As in the case of the measured $v \sin(i)$, the RV measurement of the companion could also have been influenced by the contribution of the stellar lines. If we over-subtracted the short-wavelength wing of the companion CO lines when we removed the stellar spectrum, this could introduce an artificial redshift. Comparison of the RV measurement with and without the scaling of the stellar contribution (Fig. 3.9) indicates that this effect is confined to $0.2 \, \mathrm{km \, s^{-1}}$. Assuming that we have performed the stellar removal to a precision of $\sim 10\%$, this should not add to the uncertainty in RV to a level of more than $0.1 \, \mathrm{km \, s^{-1}}$.

Our RV measurement improves the orbital constraints significantly. A large family of possible orbital solutions found by Ginski et al. (2014b), in particular with intermediate eccentricities and large semimajor axes, are now no longer in line with the observations. Further constraints from either astrometry or high-dispersion spectroscopy will take at least another decade such that GQ Lupi b has moved significantly enough in its orbit and/or changed its radial velocity.

The orbital solutions that are misaligned with the circumstellar disk are particularly intriguing. A companion in such an orbit must either have been scattered to that position, or it must have formed in situ, yet outside of the protoplanetary disk. The latter would indicate a formation scenario that is analogous to that of a binary star system with the collapsing proto-stellar core fragmenting into smaller objects.

The orbit of GQ Lupi b is wide enough that disk instability is a possible formation mechanism. Fragmentation of the disk is allowed from approximately 50 au to 300 au (Vorobyov and Basu, 2012), and although only a small number of fragments are expected to survive to become orbiting planets or brown dwarfs, this is in line with the small number of observed systems that fit the description. HR 8799 and HIP 78530 are other examples. However, if GQ Lupi b formed in situ through disk instability, one would expect low eccentricity orbits within or near the plane of the circumstellar disk. This type of orbit is not supported by the previous astrometric analysis by Ginski et al. (2014b) and our RV measurement strengthens this conclusion. Instead GQ Lupi b may have a high eccentricity orbit, which could be an indication that the companion has been scattered to its current position.

3.7.3 The systemic velocity and $v \sin(i)$ of GQ Lupi A

We measured the systemic velocity from the observed spectrum of the star and find it to be $v_{\mathrm{sys}} = -2.8 \pm 0.2 \, \mathrm{km \, s^{-1}}$. The major contributor to the uncertainty is the accuracy of the wavelength solution. Donati et al. (2012) measured the radial velocity in July 2009 to be $-3.2 \pm 0.1 \, \mathrm{km \, s^{-1}}$ and again in June 2011 to be $-2.8 \pm 0.1 \, \mathrm{km \, s^{-1}}$. They argue that the $0.4 \, \mathrm{km \, s^{-1}}$ change is real and explain it as either long-term changes of the surface granulation pattern or as the result of a

third body, a brown dwarf of a few tens of Jupiter masses orbiting the central star at a few au.

We measured the $vsin(i)$ of GQ Lupi A to be $6.8 \pm 0.5\,\mathrm{km\,s^{-1}}$, although without including additional potential broadening mechanisms, which in the case of stars with relatively low projected rotational velocities may contribute significantly to the broadening. The $6.8\,\mathrm{km\,s^{-1}}$ is therefore likely to be an overestimate. Our result is in agreement with a previous estimate by Guenther et al. (2005) of $6.8 \pm 0.4\,\mathrm{km\,s^{-1}}$. Donati et al. (2012) estimated $v\sin(i)$ to be $5 \pm 1\,\mathrm{km\,s^{-1}}$ and highlighted that, unlike Guenther et al. (2005), they included magnetic broadening. Also micro-turbulence (Donati et al., 2012) and macro-turbulence from subsurface convective zones (Grassitelli et al., 2015) may contribute to the broadening of stellar spectral lines. The rotation period of GQ Lupi A of 8.4 days (Broeg et al., 2007; Donati et al., 2012) is typical of classical T Tauri stars, and is often attributed to a disk-locking mechanism (Choi and Herbst, 1996; Landin et al., 2016).
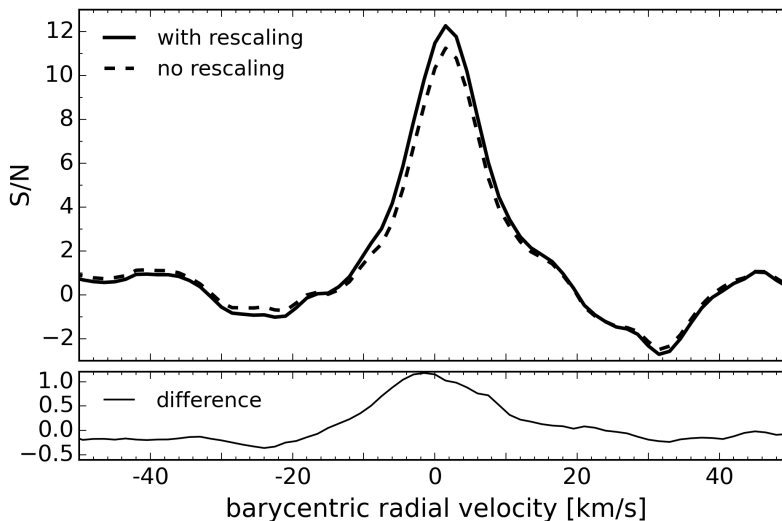
Figure 3.9: Measured cross-correlation function between the companion spectrum and the CO + H$_2$O model with and without the rescaling of the stellar lines described in section 3.4.3. The difference between the two stems from when the reference spectrum containing the stellar and telluric lines was removed from the companion spectrum. The solid line is the resulting CCF from the approach we have taken in this paper, where we have scaled the stellar lines in the reference spectrum down by 15% to match the companion to star flux ratio at the companion position. The dashed line is the CCF for the case where the reference spectrum is removed from the companion spectrum without rescaling the stellar lines. The bottom panel shows the difference between the two.

3.8   Summary and conclusions

The young GQ Lupi system has a central classical T Tauri star surrounded by a warm dust disk, and is orbited by a substellar companion GQ Lupi b at $\sim$100 au, which is either a gas giant or a brown dwarf. We observed the parent star and the companion simultanously in the K band by careful positioning of the slit of the high-dispersion spectrograph CRIRES, in combination with adaptive optics. We made use of both the spatial and spectral information to separate the spectrum of the companion from that of the host star. We detect both water and CO in the companion spectrum. The molecular lines are rotationally broadened and Doppler shifted due to the orbital motion of the companion. We measured the projected rotation velocity to be $v \sin(i) = 5.3^{+0.9}_{-1.0}$km s^{-1} and the barycentric radial velocity to be RV$=2.0 \pm 0.4$ km s^{-1}.

GQ Lupi b is a slow rotator compared to the giant planets in the solar system, and to the recent spin measurements of the exoplanets β Pic b ($v \sin(i) =$25 km s^{-1}; Snellen et al. (2014)) and 2M1207 b ($v \sin(i) =$17 km s^{-1}, Zhou et al. (2016)). This is in spite of GQ Lupi b being likely more massive than either of these, and thus this new spin measurement does not agree with the spin-mass trend of the others. However, we argue that the slow spin is a manifestation of the young age of GQ Lupi, and that the discrepancy cannot be used to argue for fundamental differences in formation path at this time.

We used the barycentric radial velocity measurement to place new constraints on orbital elements such as the semimajor axis, eccentricity, and orbital inclination with respect to the observer. This shows the strength of high-dispersion spectroscopy because it is possible to measure even small radial velocities.

The spin and RV measurements of GQ Lupi b demonstrate the potential of the combination of spatial and spectral filtering through the use of high-dispersion spectrographs together with adaptive optics.

References

Allers, K. N., J. F. Gallimore, M. C. Liu, and T. J. Dupuy
  2016. The Radial and Rotational Velocities of PSO J318.5338-22.8603, a Newly
  Confirmed Planetary-mass Member of the β Pictoris Moving Group. *ApJ*,
  819:133.

Arsenault, R., J. Alonso, H. Bonnet, J. Brynnel, B. Delabre, R. Donald-
  son, C. Dupuy, E. Fedrigo, J. Farinato, N. N. Hubin, L. Ivanescu, M. E.
  Kasper, J. Paufique, S. Rossi, S. Tordo, S. Stroebele, J.-L. Lizon, P. Gigan,
  F. Delplancke, A. Silber, M. Quattri, and R. Reiss
  2003. MACAO-VLTI: An Adaptive Optics system for the ESO VLT inter-
  ferometer. In *Adaptive Optical System Technologies II*, P. L. Wizinowich and
  D. Bonaccini, eds., volume 4839 of *Society of Photo-Optical Instrumentation En-
  gineers (SPIE) Conference Series*, Pp. 174–185.

Binks, A. S. and R. D. Jeffries
  2014. A lithium depletion boundary age of 21 Myr for the Beta Pictoris moving
  group. *MNRAS*, 438:L11–L15.

Blake, C. H., D. Charbonneau, and R. J. White
  2010. The NIRSPEC Ultracool Dwarf Radial Velocity Survey. *ApJ*, 723:684–
  706.

Borysow, A.
  2002. Collision-induced Absorption Coefficients of H_2 Pairs at Temperatures
  from 60 K to 1000 K. *A&A*, 390:779.

Borysow, A., U. G. Jørgensen, and Y. Fu
  2001. High-temperature (1000-7000k) Collision-induced Absorption of H_2
  Pairs Computed from the First Principles, with Application to Cool and Dense
  Stellar Atmospheres. *J. Quant. Spec. Radiat. Transf.*, 68(3):235.

Boss, A. P.
  1997. Giant planet formation by gravitational instability. *Science*, 276:1836–
  1839.

Boss, A. P.
  2000. Possible Rapid Gas Giant Planet Formation in the Solar Nebula and
  Other Protoplanetary Disks. *ApJ*, 536:L101–L104.

Bouvier, J., S. P. Matt, S. Mohanty, A. Scholz, K. G. Stassun, and C. Zanni
2014. Angular Momentum Evolution of Young Low-Mass Stars and Brown Dwarfs: Observations and Theory. *Protostars and Planets VI*, Pp. 433–450.

Broeg, C., T. O. B. Schmidt, E. Guenther, A. Gaedke, A. Bedalov, R. Neuhäuser, and F. M. Walter
2007. Rotational period of GQ Lupi. *A&A*, 468:1039–1044.

Brogi, M., R. J. de Kok, S. Albrecht, I. A. G. Snellen, J. L. Birkby, and H. Schwarz
2016. Rotation and Winds of Exoplanet HD 189733 b Measured with High-dispersion Transmission Spectroscopy. *ApJ*, 817:106.

Chabrier, G., A. Johansen, M. Janson, and R. Rafikov
2014. Giant Planet and Brown Dwarf Formation. *Protostars and Planets VI*, Pp. 619–642.

Choi, P. I. and W. Herbst
1996. Rotation Periods of Stars in the Orion Nebula Cluster: The Bimodal Distribution. *AJ*, 111:283.

Currie, T., A. Burrows, N. Madhusudhan, M. Fukagawa, J. H. Girard, R. Dawson, R. Murray-Clay, S. Kenyon, M. Kuchner, S. Matsumura, R. Jayawardhana, J. Chambers, and B. Bromley
2013. A Combined Very Large Telescope and Gemini Study of the Atmosphere of the Directly Imaged Planet, β Pictoris b. *ApJ*, 776:15.

Dai, Y., D. J. Wilner, S. M. Andrews, and N. Ohashi
2010. Millimeter Dust Emission in the GQ Lup System. *AJ*, 139:626–629.

Donati, J.-F., S. G. Gregory, S. H. P. Alencar, G. Hussain, J. Bouvier, C. Dougados, M. M. Jardine, F. Ménard, and M. M. Romanova
2012. Magnetometry of the classical T Tauri star GQ Lup: non-stationary dynamos and spin evolution of young Suns. *MNRAS*, 425:2948–2963.

Filippazzo, J. C., E. L. Rice, J. Faherty, K. L. Cruz, M. M. Van Gordon, and D. L. Looper
2015. Fundamental Parameters and Spectral Energy Distributions of Young and Field Age Objects with Masses Spanning the Stellar to Planetary Regime. *ApJ*, 810:158.

Ginski, C., M. Mugrauer, R. Neuhäuser, and T. O. B. Schmidt
2014a. Astrometric monitoring and orbit constraint of the GSC 08047-00232 system with VLT/NaCo. *MNRAS*, 438:1102–1113.

Ginski, C., R. Neuhäuser, M. Mugrauer, T. O. B. Schmidt, and C. Adam
2013. Orbital motion of the binary brown dwarf companions HD 130948 BC around their host star. *MNRAS*, 434:671–683.

Ginski, C., T. O. B. Schmidt, M. Mugrauer, R. Neuhäuser, N. Vogt, R. Errmann, and A. Berndt
2014b. Astrometric follow-up observations of directly imaged sub-stellar companions to young stars and brown dwarfs. *MNRAS*, 444:2280–2302.

Grassitelli, L., L. Fossati, N. Langer, A. Miglio, A. G. Istrate, and D. Sanyal
2015. Relating turbulent pressure and macroturbulence across the HR diagram with a possible link to γ Doradus stars. *A&A*, 584:L2.

Guenther, E. W., R. Neuhäuser, G. Wuchterl, M. Mugrauer, A. Bedalov, and P. H. Hauschildt
2005. The low-mass companion of GQ Lup. *Astronomische Nachrichten*, 326:958–963.

Hatzes, A. P. and H. Rauer
2015. A Definition for Giant Planets Based on the Mass-Density Relationship. *ApJ*, 810:L25.

Horne, K.
1986. An optimal extraction algorithm for CCD spectroscopy. *PASP*, 98:609–617.

Hubickyj, O., P. Bodenheimer, and J. J. Lissauer
2005. Accretion of the gaseous envelope of Jupiter around a 5 10 Earth-mass core. *Icarus*, 179:415–431.

Hügelmeyer, S. D., S. Dreizler, P. H. Hauschildt, A. Seifahrt, D. Homeier, and T. Barman
2009. Radiative transfer in circumstellar disks. I. 1D models for GQ Lupi. *A&A*, 498:793–800.

Hughes, D. W.
2003. Planetary spin. *Planet. Space Sci.*, 51:517–523.

Hughes, J., P. Hartigan, J. Krautter, and J. Kelemen
1994. The stellar population of the Lupus clouds. *AJ*, 108:1071–1090.

Husser, T.-O., S. Wende-von Berg, S. Dreizler, D. Homeier, A. Reiners, T. Barman, and P. H. Hauschildt
2013. A new extensive library of PHOENIX stellar atmospheres and synthetic spectra. *A&A*, 553:A6.

Irwin, J., Z. K. Berta, C. J. Burke, D. Charbonneau, P. Nutzman, A. A. West, and E. E. Falco
2011. On the Angular Momentum Evolution of Fully Convective Stars: Rotation Periods for Field M-dwarfs from the MEarth Transit Survey. *ApJ*, 727:56.

Jumper, P. H. and R. T. Fisher
2013. Shaping the Brown Dwarf Desert: Predicting the Primordial Brown Dwarf Binary Distributions from Turbulent Fragmentation. *ApJ*, 769:9.

Kaeufl, H.-U., P. Ballester, P. Biereichel, B. Delabre, R. Donaldson, R. Dorn, E. Fedrigo, G. Finger, G. Fischer, F. Franza, D. Gojak, G. Huster, Y. Jung, J.-L. Lizon, L. Mehrgan, M. Meyer, A. Moorwood, J.-F. Pirard, J. Paufique, E. Pozna, R. Siebenmorgen, A. Silber, J. Stegmeier, and S. Wegerer
2004. CRIRES: a high-resolution infrared spectrograph for ESO's VLT. In *Ground-based Instrumentation for Astronomy*, A. F. M. Moorwood and M. Iye, eds., volume 5492 of *Society of Photo-Optical Instrumentation Engineers (SPIE) Conference Series*, Pp. 1218–1227.

Kessler-Silacci, J., J.-C. Augereau, C. P. Dullemond, V. Geers, F. Lahuis, N. J. Evans, II, E. F. van Dishoeck, G. A. Blake, A. C. A. Boogert, J. Brown, J. K. Jørgensen, C. Knez, and K. M. Pontoppidan
2006. c2d Spitzer IRS Spectra of Disks around T Tauri Stars. I. Silicate Emission and Grain Growth. *ApJ*, 639:275–291.

Kharchenko, N. V. and S. Roeser
2009. VizieR Online Data Catalog: All-Sky Compiled Catalogue of 2.5 million stars (Kharchenko+ 2009). *VizieR Online Data Catalog*, 1280:0.

Konopacky, Q. M., A. M. Ghez, D. C. Fabrycky, B. A. Macintosh, R. J. White, T. S. Barman, E. L. Rice, G. Hallinan, and G. Duchêne
2012. Rotational Velocities of Individual Components in Very Low Mass Binaries. *ApJ*, 750:79.

Landin, N. R., L. T. S. Mendes, L. P. R. Vaz, and S. H. P. Alencar
2016. Stellar models simulating the disk-locking mechanism and the evolutionary history of the Orion Nebula cluster and NGC 2264. *A&A*, 586:A96.

Laughlin, G., P. Bodenheimer, and F. C. Adams
    2004. The Core Accretion Model Predicts Few Jovian-Mass Planets Orbiting
    Red Dwarfs. *ApJ*, 612:L73–L76.

Lecavelier des Etangs, A. and A. Vidal-Madjar
    2016. The orbit of beta Pictoris b as a transiting planet. *A&A*, 588:A60.

Louden, T. and P. J. Wheatley
    2015. Spatially Resolved Eastward Winds and Rotation of HD 189733b. *ApJ*,
    814:L24.

Marois, C., B. Macintosh, and T. Barman
    2007. GQ Lup B Visible and Near-Infrared Photometric Analysis. *ApJ*,
    654:L151–L154.

Metchev, S. A., A. Heinze, D. Apai, D. Flateau, J. Radigan, A. Burgasser, M. S.
    Marley, É. Artigau, P. Plavchan, and B. Goldman
    2015. Weather on Other Worlds. II. Survey Results: Spots are Ubiquitous on
    L and T Dwarfs. *ApJ*, 799:154.

Morales, F. Y., D. L. Padgett, G. Bryden, M. W. Werner, and E. Furlan
    2012. WISE Detections of Dust in the Habitable Zones of Planet-bearing
    Stars. *ApJ*, 757:7.

Neuhäuser, R. and W. Brandner
    1998. HIPPARCOS results for ROSAT-discovered young stars. *A&A*,
    330:L29–L32.

Neuhäuser, R., E. W. Guenther, G. Wuchterl, M. Mugrauer, A. Bedalov, and
    P. H. Hauschildt
    2005. Evidence for a co-moving sub-stellar companion of GQ Lup. *A&A*,
    435:L13–L16.

Newton, E. R., J. Irwin, D. Charbonneau, Z. K. Berta-Thompson, J. A. Dittmann,
    and A. A. West
    2016. The Rotation and Galactic Kinematics of Mid M Dwarfs in the Solar
    Neighborhood. *ApJ*, 821:93.

Nielsen, E. L., M. C. Liu, Z. Wahhaj, B. A. Biller, T. L. Hayward, J. R. Males,
    L. M. Close, K. M. Morzinski, A. J. Skemer, M. J. Kuchner, T. J. Rodigas, P. M.
    Hinz, M. Chun, C. Ftaclas, and D. W. Toomey
    2014. The Gemini NICI Planet-Finding Campaign: The Orbit of the Young
    Exoplanet β Pictoris b. *ApJ*, 794:158.

Pearce, T. D., M. C. Wyatt, and G. M. Kennedy
  2015. Constraining the orbits of sub-stellar companions imaged over short orbital arcs. *MNRAS*, 448:3679–3688.

Pollack, J. B., O. Hubickyj, P. Bodenheimer, J. J. Lissauer, M. Podolak, and Y. Greenzweig
  1996. Formation of the Giant Planets by Concurrent Accretion of Solids and Gas. *Icarus*, 124:62–85.

Reiners, A. and G. Basri
  2008. Chromospheric Activity, Rotation, and Rotational Braking in M and L Dwarfs. *ApJ*, 684:1390–1403.

Rothman, L. S., I. E. Gordon, R. J. Barber, H. Dothe, R. R. Gamache, A. Goldman, V. I. Perevalov, S. A. Tashkun, and J. Tennyson
  2010. HITEMP, the High-Temperature Molecular Spectroscopic Database. *J. Quant. Spec. Radiat. Transf.*, 111(15):2139.

Rucinski, S.
  1999. Determination of Broadening Functions Using the Singular-Value Decomposition (SVD) Technique. In *IAU Colloq. 170: Precise Stellar Radial Velocities*, J. B. Hearnshaw and C. D. Scarfe, eds., volume 185 of *Astronomical Society of the Pacific Conference Series*, P. 82.

Scholz, A., V. Kostov, R. Jayawardhana, and K. Mužić
  2015. Rotation Periods of Young Brown Dwarfs: K2 Survey in Upper Scorpius. *ApJ*, 809:L29.

Seifahrt, A., R. Neuhäuser, and P. H. Hauschildt
  2007. Near-infrared integral-field spectroscopy of the companion to GQ Lupi. *A&A*, 463:309–313.

Seperuelo Duarte, E., S. H. P. Alencar, C. Batalha, and D. Lopes
  2008. Spectrophotometric analysis of the T Tauri star GQ Lupi A. *A&A*, 489:349–357.

Showman, A. P. and Y. Kaspi
  2013. Atmospheric Dynamics of Brown Dwarfs and Directly Imaged Giant Planets. *ApJ*, 776:85.

Snellen, I., R. de Kok, J. L. Birkby, B. Brandl, M. Brogi, C. Keller, M. Kenworthy, H. Schwarz, and R. Stuik
  2015. Combining high-dispersion spectroscopy with high contrast imaging: Probing rocky planets around our nearest neighbors. *A&A*, 576:A59.

Snellen, I. A. G., B. R. Brandl, R. J. de Kok, M. Brogi, J. Birkby, and H. Schwarz
    2014. Fast spin of the young extrasolar planet β Pictoris b. *Nature*, 509:63–65.

Song, I., G. Schneider, B. Zuckerman, J. Farihi, E. E. Becklin, M. S. Bessell,
    P. Lowrance, and B. A. Macintosh
    2006. HST NICMOS Imaging of the Planetary-mass Companion to the Young
    Brown Dwarf 2MASSW J1207334-393254. *ApJ*, 652:724–729.

Stamatellos, D.
    2014. The Formation of Low-Mass Stars and Brown Dwarfs. *Astrophysics and
    Space Science Proceedings*, 36:17.

Tachihara, K., K. Dobashi, A. Mizuno, H. Ogawa, and Y. Fukui
    1996. 13CO (J= 1–0) Observations of the Lupus Molecular Clouds. *PASJ*,
    48:489–502.

Uyama, T., J. Hashimoto, M. Kuzuhara, S. Mayama, E. Akiyama, T. Kudo,
    N. Kusakabe, L. Abe, W. Brandner, T. D. Brandt, J. C. Carson, S. Egner,
    M. Feldt, M. Goto, C. A. Grady, O. Guyon, Y. Hayano, M. Hayashi, S. S.
    Hayashi, T. Henning, K. W. Hodapp, M. Ishii, M. Iye, M. Janson, R. Kandori,
    G. R. Knapp, J. Kwon, T. Matsuo, M. W. Mcelwain, S. Miyama, J.-I. Morino,
    A. Moro-Martin, T. Nishimura, T.-S. Pyo, E. Serabyn, T. Suenaga, H. Suto,
    R. Suzuki, Y. H. Takahashi, M. Takami, N. Takato, H. Terada, C. Thalmann,
    E. L. Turner, M. Watanabe, J. Wisniewski, T. Yamada, H. Takami, T. Usuda,
    and M. Tamura
    2016. The SEEDS High Contrast Imaging Survey of Exoplanets around Young
    Stellar Objects. *ArXiv e-prints*.

Vorobyov, E. I. and S. Basu
    2012. Formation and Survivability of Massive Giant Planets and Brown Dwarfs
    on Wide Orbitsfootnotemark. In *Advances in Computational Astrophysics: Meth-
    ods, Tools, and Outcome*, R. Capuzzo-Dolcetta, M. Limongi, and A. Tornambè,
    eds., volume 453 of *Astronomical Society of the Pacific Conference Series*, P. 407.

Weise, P., R. Launhardt, J. Setiawan, and T. Henning
    2010. Rotational velocities of nearby young stars. *A&A*, 517:A88.

Wende, S., A. Reiners, and H.-G. Ludwig
    2009. 3D simulations of M star atmosphere velocities and their influence on
    molecular FeH lines. *A&A*, 508:1429–1442.

Zapatero Osorio, M. R., E. L. Martín, H. Bouy, R. Tata, R. Deshpande, and R. J. Wainscoat
2006. Spectroscopic Rotational Velocities of Brown Dwarfs. *ApJ*, 647:1405–1412.

Zhou, Y., D. Apai, G. H. Schneider, M. S. Marley, and A. P. Showman
2016. Discovery of Rotational Modulations in the Planetary-mass Companion 2M1207b: Intermediate Rotation Period and Heterogeneous Clouds in a Low Gravity Atmosphere. *ApJ*, 818:176.

Zhou, Y., G. J. Herczeg, A. L. Kraus, S. Metchev, and K. L. Cruz
2014. Accretion onto Planetary Mass Companions of Low-mass Young Stars. *ApJ*, 783:L17.

4 | Spin measurement of the substellar companion GSC 6214-210 b with CRIRES

In collaboration with:
Matteo Brogi, Ignas Snellen, Jayne Birkby, Remco de Kok
In preparation

The rotational velocities of exoplanets and brown dwarf companions are fundamental observables which affects their climate, atmospheric dynamics, and magnetic field, and may hold important clues to the formation process and the orbital history of these objects. We have measured the projected rotational velocity of the young, directly imaged, substellar companion GSC 06214-00210 b, which has a well-determined mass straddling the planet − brown dwarf boundary. Rotation period data are available in the literature for very low-mass stars and brown dwarfs, both in open clusters and in the field, but substellar companions present a unique challenge due to their close proximity to a bright host star. We combine spectral and spatial filtering to separate the signal of the companion from that of the host star by observing the target in the near-infrared with a high-dispersion slit spectrograph using adaptive optics. The companion spectrum is optimally extracted and cross-correlated with a template spectrum, and the rotational broadening is measured from the shape of the cross-correlation signal. We detect carbon monoxide with a signal-to-noise of 5.3 in the atmosphere of GSC 06214-00210 b and measure the projected rotational velocity to be $v \sin(i) = 21.5 \pm 3.5 \, \mathrm{km \, s^{-1}}$. That is similar to the $v \sin(i)$ measured for the exoplanet β Pictoris b, but significantly faster than that for GQ Lupi b.

4.1   Introduction

Climate and atmospheric dynamics can be strongly affected by the spin rate of a planet. A faster rotation period for the Earth would have a profound effect on ocean and wind circulation patterns and the redistribution of solar energy around the globe, leading to a greater temperature difference from equator to pole (Showman et al., 2013). The spin rate plays an equally important role in the case of gas giants.

Showman et al. (2015) discuss the effects of rotation on warm and hot Jupiters, and Showman and Kaspi (2013) focus on brown dwarfs and directly imaged planets, the former of which are generally fast rotators causing the large-scale flows to be rotationally dominated. Also the occurrence and strength of a magnetic field are closely linked to planet rotation (Parker, 1955; López-Morales et al., 2011).

It is clear that planets acquire their angular momenta during the early formation process, when they accrete the bulk of their masses. Unlike low-mass stars, that can lose a large fraction of their spin through magnetic breaking, planets are more likely to retain their angular momenta except through gravitational interactions. The details of how angular momentum is accreted are less clear. Generally, two formation processes are considered for giant planets: i) core accretion, where gas accretes onto planetary embryos of several Earth masses (Pollack et al., 1996; Laughlin et al., 2004; Hubickyj et al., 2005), and ii) disk fragmentation, where gas rapidly collapses on itself due to a disk gravitational instability in the outer protoplanetary disk (Boss, 1997, 2000). If core accretion and disk fragmentation result in differences in spin angular momenta, it is possible this will show up in studies of the spin of substellar companions as a function of mass and of orbital distance, which could be a proxy for different formation scenarios.

The solar system planets have a wide range of spin velocities which show an increasing trend with planetary mass (Hughes, 2003). The Earth and Mars rotate relatively slowly with spin rates of 24 to 25 hours and equatorial rotation velocities of $465 \, \mathrm{m\,s^{-1}}$ and $241 \, \mathrm{m\,s^{-1}}$, respectively. Neptune and Uranus rotate in 16 to 17 hours with velocities around $2.6 \, \mathrm{km\,s^{-1}}$, while Jupiter and Saturn rotate significantly faster in 10 to 11 hours with $12.6 \, \mathrm{km\,s^{-1}}$ and $9.9 \, \mathrm{km\,s^{-1}}$, respectively. Mercury and Venus have equatorial rotation velocities that fall below the spin − mass relation observed in the remaining planets, but this can be explained by the tidal interactions with the Sun that have significantly slowed them down. Also, the Earth has been slowed somewhat owing to tidal energy dissipation by the Moon. Surprisingly, Uranus does follow the trend while its obliquity is $\sim 98°$, pointing to a catastrophic event.

Two observational methods are available to measure the spin of an extrasolar body. The first makes use of temporal photometric variations caused by local variations in the surface brightness that can be monitored during rotation. In the case of substellar companions, this requires high-contrast direct imaging techniques to separate the starlight from that of the faint companion. It has been applied to the exoplanet 2M1207 b exhibiting flux modulations indicating a rotation period of 10.7 hours (Zhou et al., 2016). The second method, as used in this paper, combines high-dispersion spectroscopy with high-contrast imaging to separate the light from the companion from that of the star, and subsequently

the projected rotational velocity ($v\sin(i)$) is measured through the width of absorption lines in the thermal spectrum of the companion. Although this is not a direct measurement of the rotation period, since the viewing geometry is generally unknown, the method does not depend on the presence of surface brightness variations, it is more straightforward to interpret, and it can be performed in relatively short observing time - if the appropriate instrumentation is available. In this way, our group observed the exoplanet β Pictoris b with the Very Large Telescope (VLT) and the instrument the Cryogenic High-Resolution Infrared Echelle Spectrograph (CRIRES; Kaeufl et al., 2004), measuring it to have a $v\sin(i)$ of $25\,\mathrm{km\,s^{-1}}$ (Snellen et al., 2014). Just before CRIRES was taken off the telescope for a major upgrade, we were awarded time to conduct a small survey to measure the $v\sin(i)$ of three additional substellar companions to further investigate the spin properties of wide-orbit, young companions. Observations of GQ Lupi b are discussed in Schwarz et al. (2016, $v\sin(i) = 5.3\,\mathrm{km\,s^{-1}}$), and those of HIP 78530 b will be presented in a forthcoming paper. Here we describe the observations and results for GSC 06214-00210 b (hereafter GSC 6214 b), which has an age and a mass in between those of β Pictoris b and GQ Lupi b.

In Section 2 we characterise the GSC 6214 system, and in Section 3 we give the details of the observations. The data analysis is explained in Sections 4 and 5: Section 4 is the basic data reduction and the extraction of the companion spectrum, and Section 5 is the cross-correlation analysis which we employ to measure the rotational broadening of the molecular lines in the thermal spectrum of the companion. The results are presented and discussed in Section 6.

4.2 The GSC 06214-00210 system

GSC 6214 A is a pre-main-sequence, solar-type star in Upper Scorpius, which is a subgroup of the nearest OB association. Members of Upper Scorpius have a small age dispersion (Preibisch and Mamajek, 2008), with a typical age initially estimated by low-mass evolutionary models to be 5 Myr (Preibisch et al., 2002), and more recently revised to 11 Myr (Pecaut et al., 2012), based on isochrone fitting. The 16 M_J companion GSC 6214 b was discovered by Ireland et al. (2011) with adaptive optics imaging. It is seen to orbit at a projected distance of 320 au, and there is unambiguous evidence for a circumplanetary accretion disk (Bowler et al., 2011; Lachapelle et al., 2015; Zhou et al., 2014). The dust mass of this disk is constrained to less than 0.15 $\mathrm{M}_\oplus$ by observations from the Atacama Large Millimeter/submillimeter Array (ALMA; Bowler et al., 2015), and GSC 6214 b is therefore not expected to gain significant mass. More information about the system is given in Table 5.1.

Table 4.1: GSC 06214-00210 system properties

Property	GSC 6214 A[i]	GSC 6214 b[ii]
Teff [K]	4200 ± 150	2300 ± 200
Spectral type	$K7 \pm 0.5$	$M9\gamma \pm 0.5$
Mass	$0.9 \pm 0.1 \, \mathrm{M_\odot}$	$16 \pm 1.5 \, \mathrm{M}_J$
Surf. grav. $\log(g)$	4.0	
Distance [pc][iii]	145 ± 20	
Age [Myr][v]	11 ± 2	
Ang. sep. ["][ii]	2.17 ± 0.02	
ΔK [mag][ii]	5.74 ± 0.01	

[i] Bowler et al. (2011)
[ii] Lachapelle et al. (2015)
[iii] de Zeeuw et al. (1999)
[v] Pecaut et al. (2012)

4.3 Observations

We observed the GSC 6214 system on 29 May 2014 as part of the ESO programme 293.C-5012(A). The observations were carried out with the infrared high-dispersion spectrograph CRIRES (Kaeufl et al., 2004) at the Very Large Telescope on Cerro Paranal in Chile. We obtained a standard set of calibration frames and eight science exposures of 300 seconds each. We used the smallest slit width of $0.2''$ to maximise the spectral resolution, which is close to 90 000. The slit was aligned with the position angle of the companion ($PA = 175.2°$, Zhou et al., 2014), thus observing the host star and the companion simultaneously. With a K-band contrast ratio between the companion and the host star of 5.06×10^{-3} (Lachapelle et al., 2015), and an angular separation of $2.2''$, these are high contrast observations. We made use of the Multi Application Curvature Adaptive Optics system (MACAO, Arsenault et al., 2003) to both suppress the star light and maximise the throughput. The observations were carried out under clear sky conditions, at airmasses below 1.02, hence very close to zenith, and with seeing of $1''$. The telescope was nodded sequentially in an ABBA pattern along the slit direction between positions A and B, $10''$ apart, to allow accurate background subtraction. Additionally, a small random offset was introduced for each exposure to improve flatfielding and hot pixel corrections.

The CRIRES instrument has four Aladdin III InSB detectors each spanning 1024 x 512 pixels with physical separations between the detectors corresponding

to approximately 280 pixels. We observed at 2.3 μm targeting the ro-vibrational (2, 0) R branch of carbon monoxide, with the standard wavelength settings for order 24. Additional absorption from water vapour is also likely to be present at these wavelengths.

4.4   Data analysis

The basic data reduction was performed with recipes from the CRIRES pipeline version 2.3.2 and processed with the EsoRex tool version 3.10.2. The raw science frames were dark-subtracted, flatfielded, and corrected for known bad pixels and non-linearity effects. Furthermore, EsoRex was used to perform the background subtraction by combining the science frames in AB nodding pairs, and to optimally extract (Horne, 1986) a one-dimensional spectrum of the star GSC 6214 A from each of the four AB-combined frames. The remainder of the data analysis was carried out with custom-built Python scripts, unless specifically stated otherwise.
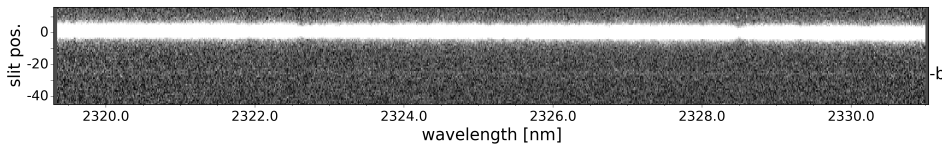
Figure 4.1: An example of a two-dimensional spectrum from detector 3, after the basic data reduction steps and cropped to the relevant slit positions. The bright band is the spectral trail of the star. Twenty-six pixels below, the faint trail of the companion can be seen (marked with b).

We cropped the combined frames in the spatial direction (i.e. along the slit) close to the positions of the stellar spectrum and the companion spectrum. The automatic bad pixel correction in the CRIRES pipeline is insufficient and therefore we visually identified remaining detector defects and cosmic rays using the programme *SAOImage DS9*. The bad pixels were corrected with cubic spline interpolation based on the four nearest neighbours within the same row. A few detector defects were severe enough that it was necessary to mask out entire columns from the subsequent data analysis. This was the case for 32 columns in the second detector, 65 columns in the fourth detector, as well as the four columns closest to the left and right edge of all detectors. Fig. 5.2 is one of the AB-combined frames from the third detector. The faint spectral trail of the companion is visible 26 pixels below the stellar spectral trail.

We opted to discard the first detector from the analysis, based on the combined

effects of a well-known non-linearity issue[1] causing a high noise level, and very little expected signal due to few CO lines in that part of the wavelength range. The fourth detector suffers from the same non-linear effects, but this was adequately corrected by the non-linearity procedure of the pipeline. Unfortunately, we have also had to discard the first and second AB-combined frames from all detectors, leaving only half of the data set. The first frame suffers from an unknown systematic issue across the entire wavelength range, which has caused severe non-linearity from row to row. The second frame was exposed as the target passed zenith, and the violent slewing of the telescope caused the companion not to be within the slit throughout the exposure.

4.4.1   Extraction of the companion spectrum

From the carefully cleaned frames, we performed an optimal extraction of the companion spectra with the IRAF procedure *apall*. The fitted trace of the stellar spectral trail was applied as a reference and manually offset to the position of the companion, which could easily be identified by summing together 100-500 wavelength bins. We found this to be well-matched by the pixel distance determined from the plate scale and the literature value for the angular separation. The background of scattered stellar light was ignored at this stage and was instead removed manually as described in section 4.4.3. We extracted a companion spectrum from each detector and AB-combined frame.

4.4.2   Wavelength calibration and the systemic velocity

We determined the wavelength solution in an iterative process of refining trial wavelength solutions based on cross-correlating the average observed stellar spectrum and a template spectrum which contained both stellar molecular lines and telluric lines. The Doppler shift of the stellar lines in the model was allowed to vary at every step of the iteration so that we could simultaneously measure the unknown radial velocity (RV) of the star.

   The wavelength calibration was performed separately for each detector. The change in the Doppler shift of the stellar lines due to the rotation and the orbital motion of the Earth is negligible over the course of the 40 minutes of the observations, and therefore it is sufficient to calibrate the average observed spectrum. We constructed template spectra for a range of Doppler shifts by multiplying a Doppler shifted PHOENIX model and a synthetic transmission spectrum from ESO SkyCalc. The details of the models are given in table 4.2. Both the telluric

---

[1]http://www.eso.org/sci/facilities/paranal/instruments/crires/doc/VLT-MAN-ESO-14500-3486_v93.pdf

model and the stellar model was convolved to a spectral resolution of 90 000, which is a typical value for the actual resolving power of CRIRES. This provided a visually good fit to the telluric lines, and although the fit of the stellar lines was imperfect, we found that it was sufficient for the wavelength calibration. Both the Doppler shifted Phoenix model and the telluric model were interpolated to a trial wavelength solution before they were multiplied and cross-correlated with the observed spectrum. The initial trial solution was taken from a previous CRIRES data set, published in Schwarz et al. (2016).

Table 4.2: The template spectra in the wavelength calibration routine were constructed from the following individual models

GSC 6214-210 A model: PHOENIX
Teff 4200 K   log(g) 4.0   solar metallicity http://phoenix.astro.physik.uni-goettingen.de Husser et al. (2013)
Sky transmission model: ESO SkyCalc
Airmass 1.0   PWV seasonal https://www.eso.org/observing/etc/skycalc Noll et al. (2012); Jones et al. (2013)

The final wavelength solution was determined in an iterative process of refining the trial solutions to maximise the cross-correlation coefficient while allowing the Doppler shift of the stellar lines to vary. This method is an adaptation of the iterative wavelength calibration in Brogi et al. (2016). Following Brogi et al. (2016), the trial wavelength solutions are quadratic fits to all possible combinations of five evenly spaced wavelength guesses for the first, the middle and the last pixel of the detector. This corresponds to a total of 125 trial solutions. For each iteration, we selected the provisional best wavelength solution based on the highest cross-correlation coefficient and let this solution form the central triplet of pixel-wavelength pairs in the following iteration, where the wavelength step size between guesses was refined. We found that for all detectors the cross-correlation coefficient improved with each iteration until a step size corresponding to 10% of a pixel (Fig. ??), and also at this step size the best radial velocity of the star converged to a single value (Fig. ??). Accordingly, we estimated that the accuracy of the final wavelength solution was 10% of a pixel, and applying the heliocentric correction of $-0.06 \, \mathrm{km \, s^{-1}}$, the systemic velocity of GSC 6214 A was measured to be $-5.3 \pm 0.1 \, \mathrm{km \, s^{-1}}$.
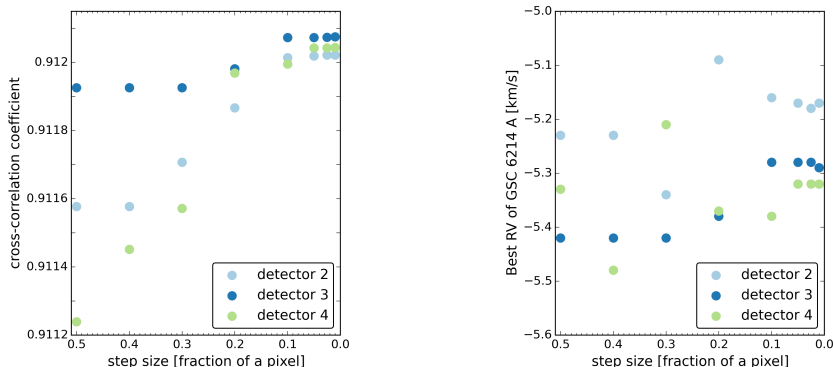
(A) The accuracy of the wavelength solutions continued to improve with iterations until a step size corresponding to 10% of a pixel.

(B) The measured RV-values for GSC 6214 A, corrected for the rotation and the orbit of the Earth.

Figure 4.2: The wavelength solution was determined in an iterative process of cross-correlating the observed stellar spectrum and a template spectrum. For each iteration the best wavelength solution (i.e. the one with the highest cross-correlation coefficient) from a set of 125 trial solutions was selected and the step size defining the grid of solutions was refined. The radial velocity of the star was measured at every iteration of the wavelength calibration by cross-correlating with template spectra where the stellar lines had a range of Doppler shifts relative to the stationary telluric lines.

4.4.3   Removing the stellar and telluric background

At the position of the companion, the flux is dominated by the companion itself with the stellar flux suppressed to a level of 20% of that of the companion. The observed stellar spectrum including telluric lines was scaled to this contrast ratio and subtracted.

For removing the telluric lines in the companion spectrum, we made use of the same telluric model which was applied in the template used for the wavelength calibration (Table 4.2). The telluric model was carefully fitted to the average observed stellar spectrum to adjust the line profiles to the instrumental profile. First, the observed stellar spectrum including telluric lines was flattened, i.e. the continuum gradient was removed by fitting the continuum with a polynomial and dividing with the fit. The telluric model and the stellar model (also as used for the wavelength calibration, Table 4.2) were both downsampled to the wavelength solution and the stellar model was Doppler shifted to the measured radial velocity of the star. Then, the stellar model was adjusted to the observed stellar spectrum by con-

volving with a broadening kernel determined with singular value decomposition (SVD; Rucinski, 1999), and the observed stellar spectrum was divided with this stellar fit, thus providing the observed telluric spectrum. Subsequently, the telluric model was adjusted to the observed telluric spectrum, again by convolving with an SVD broadening kernel. This resulted in a telluric model with the correct line profiles broadened by the instrument profile, which was then scaled to the mean level of the companion spectrum and subtracted. The influence of contamination from the Earth's atmosphere on the companion spectrum is very small for this data set. The final companion spectrum is shown in Fig. 4.4, and is the weighted average of the two frames with the weights determined from the cross-correlation analysis (Sec. 4.5.2).

4.5   Measuring the $v\sin(i)$

The thermal spectrum of the companion has absorption lines from molecules present in the companion atmosphere and when observed at the high spectral resolution of CRIRES, the molecular bands are resolved into individual lines. The rotation of the object causes a broadening of the spectral lines due to the redshifts of the receding half of the surface and the blueshifts of the approaching half. In other words, the broadening reveals the component of the spin velocity projected along the line of sight, and thus provides a minimum value for the objects rotational velocity. However, the extracted companion spectrum of GSC 6214 b has a low signal-to-noise (S/N), and it is not possible to measure the broadening of the individual lines directly. Instead, we combine the signal from all the spectral lines within the wavelength range by cross-correlating with a template spectrum. The cross-correlation function will have a peak if the relative positions of the spectral lines of the model match those of the observed spectrum, and by using models with a single trace gas the presence of specific gas molecules in the atmosphere can be unambiguously detected. Most importantly, the cross-correlation profile is highly sensitive to the shape of the spectral lines in the observed spectrum, and therefore the projected rotational velocity can be measured from the cross-correlation function.

4.5.1   The template spectra

At the high temperatures of a young object like GSC 6214 b, the most abundant trace gas molecules in the K-band are expected to be CO and H_2O (Barman et al., 2015; Moses et al., 2016). We modelled the thermal spectrum of GSC 6214 b with the single-trace gas and double-trace gas template spectra, which were gen-
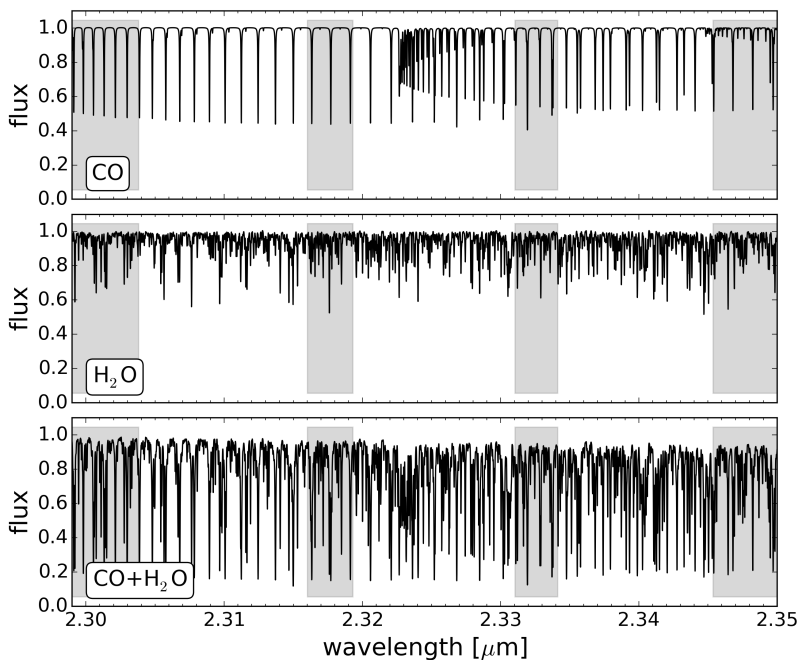
Figure 4.3: The template spectra which were used in the cross-correlation analysis. The top two panels show the models with either CO or H_2O as a single-trace gas, and the lower panel shows the model containing both CO and H_2O. The three models have temperatures that decrease with a constant lapse rate from 2150 K at 1 bar to 1100 K at 0.03 bar, and the T/p profiles are isothermal outside of this pressure range. The volume mixing ratios for CO and H_2O are 10^{-4} both in the single-trace gas and double-trace gas models. The gaps between the three detectors are shaded in grey.

erated for GQ Lupi b by Schwarz et al. (2016). These models employ the line lists from HITEMP 2010 (Rothman et al., 2010), and assume collision-induced absorption by hydrogen (Borysow et al., 2001; Borysow, 2002). The temperature-pressure profiles (T/p profiles) were parameterised the following way: They are isothermal at pressures higher than $p_0 = 1$ bar with a temperature of $T_0 = [1650\,\text{K},$ $1900\,\text{K}, 2150\,\text{K}]$, and the temperature decreases with a constant lapse rate (i.e. the rate of temperature change with log pressure) until it reaches $T_1 = [750\,\text{K}, 1100\,\text{K},$ $1450\,\text{K}, 1800\,\text{K}]$ at pressure $p_1 = [10^{-1.5}\,\text{bar}, 10^{-2.5}\,\text{bar}, 10^{-3.5}\,\text{bar}, 10^{-4.5}\,\text{bar}]$. The models are isothermal again at higher altitudes or equivalently lower pressures. Both CO and H_2O were tested with four different volume mixing ratios, VMR $= [10^{-5.5}, 10^{-5.0}, 10^{-4.5}, 10^{-4.0}]$. The model spectra were convolved to the spectral resolution of CRIRES, which we have measured to be $\sim 90\,000$, prior to cross-correlation. Fig. 4.3 illustrates the three example models from the T/p grid.

4.5.2 Cross-correlation analysis

We performed the cross-correlation individually per frame and detector, and the analysis was carried out for every template spectrum in the T/p grid described in Sec. 4.5.1. The model was Doppler-shifted over the range -250 to $250\,\mathrm{km\,s^{-1}}$, and the individual companion spectra were cross-correlated with the model for every RV step of $1.5\,\mathrm{km\,s^{-1}}$. We will refer to the cross-correlation function (CCF) from the companion spectrum and a template spectrum as the measured CCF. The designations for the different types of cross-correlation functions that are used in this paper are summarised in Table 4.3. The model has not been subjected to rotational broadening, so the absorption lines are relatively narrow with a width dominated by the instrumental profile, which we have applied to all the models. Assuming the molecule of the model is present in the companion atmosphere, the cross-correlation of the narrow-lined model with an observed spectrum with rotationally broadened lines will produce a cross-correlation signal centred on the radial velocity of the companion, and the shape of the signal will be closely related, though not identical, to the average line profile of the observed spectrum.

Table 4.3: Nomenclature for the cross-correlation functions

Designation	Spectrum 1 $\star$ Spectrum 2
measured CCF	companion spec. $\star$ model $v \sin(i) = 0$
broad meas. CCF	companion spec. $\star$ model $v \sin(i) \neq 0$
injected CCF	injected spec. $\star$ model $v \sin(i) = 0$
(narrow) auto-CF	model $v \sin(i) = 0 \star$ model $v \sin(i) = 0$
broad auto-CF	model $v \sin(i) \neq 0 \star$ model $v \sin(i) \neq 0$
model CCF	model $v \sin(i) = 0 \star$ model $v \sin(i) \neq 0$

CCF = cross-correlation function; auto-CF = auto-correlation function; spec. = spectrum; meas. = measured

In order to determine appropriate weighting of the frames and detectors, we resampled the model at the observed wavelengths and injected it into the measured companion spectrum:

$$\mathrm{inj\_spec.} = \mathrm{comp\_spec.} + \mathrm{model} * mean(\mathrm{comp\_spec.}) \qquad (4.1)$$

The injected spectrum was cross-correlated with the model spectrum, and the difference between this injected CCF and the measured CCF represents the expected cross-correlation signal from a given model, and it is sensitive to both the strength and the number of spectral lines for a given detector. Although this step is performed for each frame, the expected signal is unique to each model and detector,

and independent of the data quality. On the other hand, the measured CCF does contain information about the data quality, because it is sensitive to the S/N of the companion spectrum as obtained from the individual frames of a detector. Both effects are combined in a form of S/N weights:

$$w = \left(\frac{max(\text{injected CCF} - \text{measured CCF})}{std(\text{measured CCF})} \right)^2 \tag{4.2}$$

The weights were normalised and they constitute a set of detector weights and frame weights which were used both separately and together, depending on the context. In particular the weights were applied to the cross-correlation functions of the individual frames and detectors to construct the weighted averages of any cross-correlation functions considered in the remainder of this paper. The frame weights were also applied when combining the companion spectra from the individual frames to the final weighted average spectrum of GSC 6214 b, which is displayed in Fig. 4.4.

We fit the signal of the measured CCF with model CCFs, in order to measure the projected rotational velocity and the radial velocity of the companion. The model CCFs were constructed by cross-correlating the non-broadened model spectrum with rotationally broadened and shifted versions of the model itself. We tested projected rotational velocities in the range 0 to $60 \, \text{km s}^{-1}$ and Doppler shifts in the range -20 to $10 \, \text{km s}^{-1}$. For both parameters the step size was $0.5 \, \text{km s}^{-1}$. Thereafter, each of these model CCFs was offset (y-direction) and scaled with a least-squares fit to best match the measured companion CCF. Finally, we determined the best-fit model CCF, and by extension the best-fit $v \sin(i)$ and RV, through $\mathcal{X}^2$ minimisation, along with confidence intervals from rescaling the errors so $\bar{\mathcal{X}}^2 = 1$. The measured radial velocity was corrected to the heliocentric radial velocity, i.e. it was compensated for the relative radial velocity of the observer at the time of observation, caused by the spin rotation of Earth and the orbital motion around the Sun.

4.6   Results & Discussion

The final spectrum of the substellar companion GSC 6214 b is shown if Fig. 4.4, with the rotationally broadened CO model overplotted in red. The S/N of the spectrum in detectors 2, 3, and 4 are ~0.9, 1.1, and 1.5, respectively. This striking difference is mirrored in the spectrum of the host star, and in fact the continuum flux of the stellar spectral trail was seen to increase gradually from the shorter to the longer wavelengths. The cause of the wavelength dependence is unknown but must have an instrumental origin. It has no influence on the results: The detector
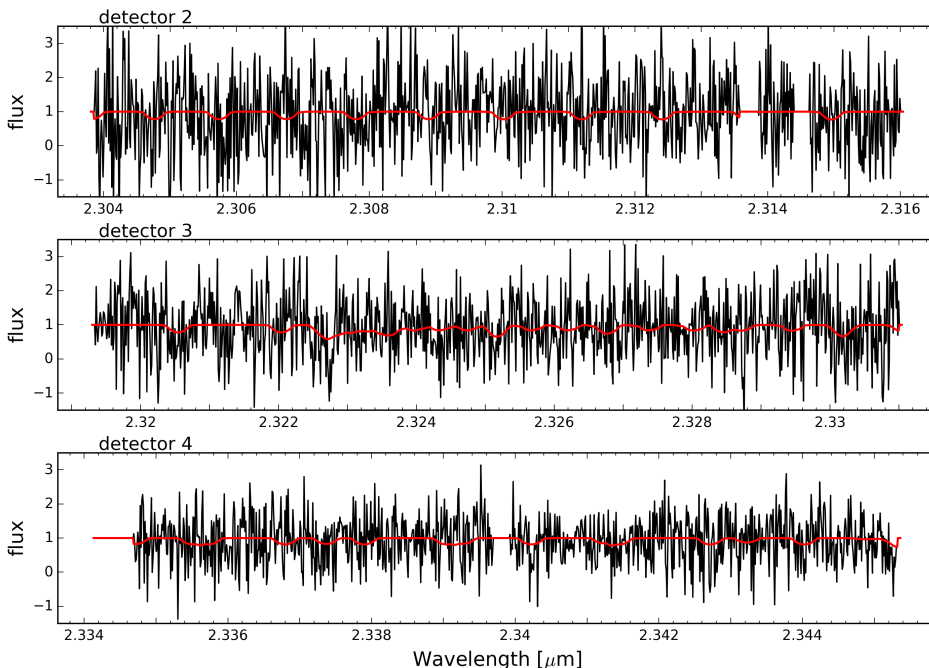
Figure 4.4: The thermal spectrum of GSC 6214 b (black). The individual frames were combined as a weighted average, where the weights were determined as part of the cross-correlation analysis, as described in Sec. 4.5.2. The red line is the CO model from the top panel of Fig. 4.3, convolved to the CRIRES resolution, rotationally broadened to match the measured $v\sin(i)$ of $21.5\,\mathrm{km\,s^{-1}}$, and Doppler shifted to match the expected radial velocity. Although the companion spectrum is dominated by noise, some of the more prominent CO lines are discernible in detectors 3 and 4.

weights in the cross-correlation analysis are sensitive to the S/N of the companion spectrum, as well as to the number and strength of lines for a given detector (Sec. 4.5.2). In general, due to the low S/N, the individual CO lines of the thermal spectrum are hidden within the noise, but hints of the most prominent absorption lines can be identified in detectors 3 and 4.

Subsequently, the presence of specific individual molecules is best revealed from cross-correlating with single-trace-gas model spectra. Fig. 4.3 shows the CO, H_2O, and CO+H_2O model spectra from Schwarz et al. (2016), which we have used in the cross-correlation analysis. The displayed models are representative of the tested model grid, and we find that at the low S/N of these observations, the results are insensitive to a wide range of T/p profiles. The example models share the same T/p profile and have a temperature that decreases from 2150 K at 1 bar

to 1100 K at 0.03 bar and is isothermal outside this pressure range.

We detect CO in the atmosphere of GSC 6214 b, but we cannot confirm the presence of H_2O from these observations. The measured cross-correlation function using the CO single-trace gas model is shown by the solid black line in Fig. 5.6. The lower panel is a magnification of the relevant region. The cross-correlation function shows a distinct and broadened CO signal centred around a radial velocity close to the systemic velocity. Cross-correlation using the double-trace gas model give rise to a similar, yet slightly weaker signal, and the H_2O model shows no hint of a signal.

The profile of the measured CO cross-correlation signal is broadened, and the narrow auto-correlation function of the CO model is a poor fit. The auto-CF is shown in Fig. 5.6 as the black dotted line. This is a clear indication that the absorption lines of the companion spectrum are rotationally broadened. We have fitted the measured CCF with model CCFs of varying $v \sin(i)$-values and Doppler shifts, as described in Sec. 4.5. The best-fit model CCF is determined from χ^2 minimisation, and it is shown as the red solid line in Fig. 5.6, and the shading indicates the 2σ confidence. We find that the projected rotational velocity of GSC 6214 b is $21.5 \pm 3.5 \, \mathrm{km \, s^{-1}}$, whereas a Doppler shift relative to the systemic velocity ($5.3 \, \mathrm{km \, s^{-1}}$, Sec. 4.4.2) was not unambiguously detected.

The significance of the CO detection cannot be deduced from the measured cross-correlation function of the companion spectrum and the CO model, because the narrow lines of the model are not a good match to the rotationally broadened lines present in the observed companion spectrum. Instead, we cross-correlated the companion spectrum with the model rotationally broadened by the best-fit $v \sin(i) = 21.5 \, \mathrm{km \, s^{-1}}$, and then adopted the S/N of this broad measured CCF:

$$\frac{S}{N} = \frac{max(\text{broad meas. CCF})}{std(\text{broad meas. CCF} - \text{broad auto-CF})} \tag{4.3}$$

The signal is the peak value of the broad measured CCF, and the noise is the standard deviation of the broad measured CCF minus the auto-correlation function of the rotationally broadened model. From this, we find that CO is detected in the atmosphere of GSC 6214 b with a S/N of 5.3.

The radii of directly-imaged planets cannot be measured directly as in the case of transiting planets, and have to be inferred from evolutionary models and/or connecting their effective temperature to their luminosity. In the case of GSC 6214 b, we estimate the current radius to be approximately $1.7 \pm 0.2 \, \mathrm{R_J}$ based on evolutionary models (Burrows et al., 2001), and thus the companion is expected to spin up to $37 \pm 7 \, \mathrm{km \, s^{-1}}$ when it ultimately contracts to the size of Jupiter. This implies that the rotation period of the sub-stellar companion is currently $\sim$9-10 hours, and is expected to decrease to $\sim$3-4 hours.
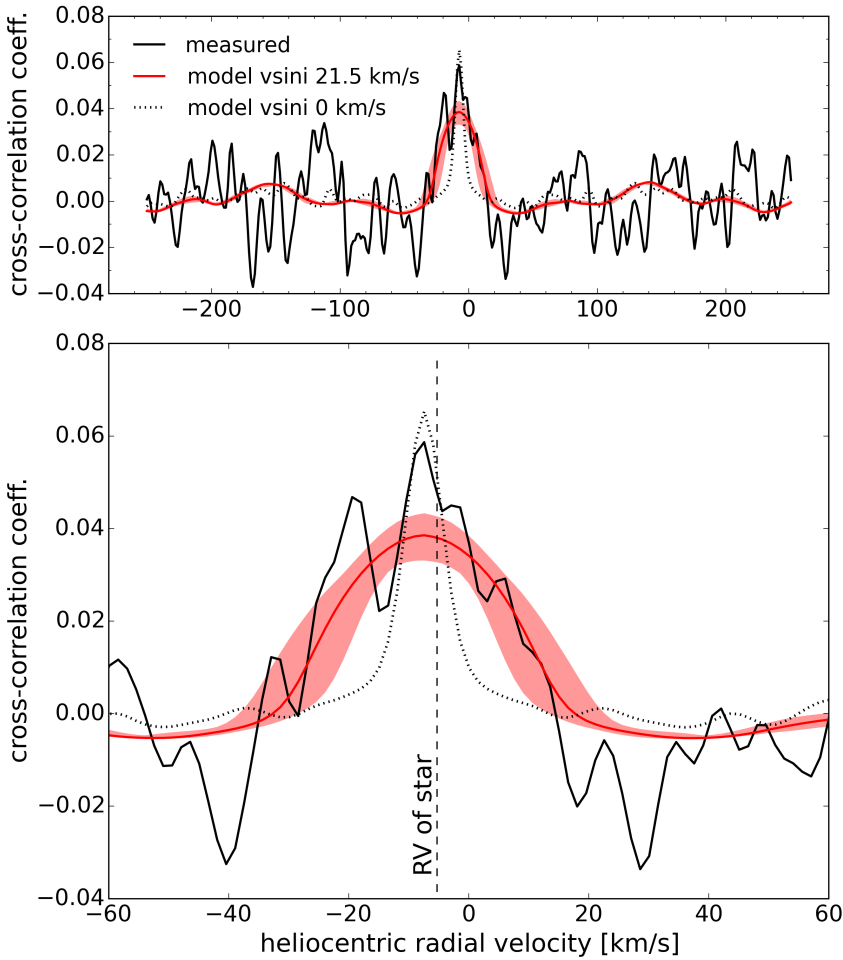
Figure 4.5: The cross-correlation function (CCF) from the CO model with narrow absorption lines and the observed companion spectrum (solid black line). The peak, centred at an RV close to that of the host star, shows that GSC 6214 b has CO in the atmosphere. The black dotted line is the auto-correlation function of the CO model, scaled and offset to best match the measured CCF. It can be seen that the measured CO signal is broader than the auto-correlation signal. We find that the measured CCF is well fit by a model CCF from the CO model and a rotationally broadened version of itself with a vsini of 21.5 km s^{-1}. This best fit model CCF is shown as the red solid line, and the shading indicates the 2σ confidence. As for the auto-correlation function, the broader model CCF has been scaled and offset with a least-square fit to the measured CCF. The lower panel is an enlarged version of the central radial velocities of the upper panel.

We measure the radial velocity, corrected for the heliocentric motion, of GSC 6214 b to be $-7.6 \pm 2.0\,\mathrm{km\,s^{-1}}$. This is consistent within the 2σ errorbars with the systemic velocity of the host star ($-5.3\,\mathrm{km\,s^{-1}}$), which was measured as part of the wavelength calibration routine in Sec. 4.4.2. The expected circular orbital velocity of GSC 6214 b is $1.6\,\mathrm{km\,s^{-1}}$ at the observed orbital distance of 320 au. Therefore, the RV measurement is well within the expected range. Unfortunately, the S/N of these observations are not sufficient to further constrain the orbit, like in the case of GQ Lupi b (Schwarz et al., 2016) and β Pictoris b (Snellen et al., 2014).

Only three other substellar companions have measurements of their spin rotation: β Pictoris b and 2M1207 b which are likely of planetary mass, and GQ Lupi b which has a highly uncertain masses, straddling the planet − brown dwarf boundary. β Pictoris b and GQ Lupi b both have $v\sin(i)$ measurements (Snellen et al., 2014; Schwarz et al., 2016) and are a part of the CRIRES survey that this work is based upon, and 2M1207 b has a measurement of the rotation period (Zhou et al., 2016) from which the equatorial rotation velocity can be inferred. Their rotational velocities (either $v\sin(i)$ or v_{eq}) are plotted as a function of mass in Fig. 4.6. The rotational velocity of GSC 6214 b falls in between those of β Pictoris b and 2M1207 b, and GQ Lupi b appears as an outlier with a rotational velocity 3 to 5 times slower than the others.

We can speculate that the initial angular momentum content of a substellar companion will depend on its specific formation scenario (e.g. core accretion versus disk fragmentation) and its total accreted mass. However, the observable - the spin velocity or rotation period - will also depend on its current state of evolution. E.g. the objects can still be accreting matter and angular momentum. Also, they will significantly spin-up to faster rotational velocities during their contraction and cooling phase. The sample of substellar companions with measured spin rates currently available is too small to disentangle these different processes. However, we see that the youngest object in the sample, GQ Lupi b (<5 Myr), indeed exhibits the slowest rotation pointing to an evolutionary effect. GSC 6214 b is of intermediate age (11 Myr) within the sample, and rotates significantly faster than GQ Lupi b, with a velocity that is comparable to the β Pictoris b and 2M1207 b measurements. However, GSC 6214 b is also more massive than those two, and in the light of the mass-spin relation as seen in our solar system, it may be expected that more massive planets rotate faster. Both GQ Lupi b and GSC 6214 b are actively accreting material (e.g. Zhou et al., 2014), but in the case of GSC 6214 b the dust mass of the accretion disk has been constrained by ALMA observations to less than $0.15\,\mathrm{M_{\oplus}}$ (Bowler et al., 2015), meaning that GSC 6214 b is not expected to gain significant mass or angular momentum from accretion. Of course,
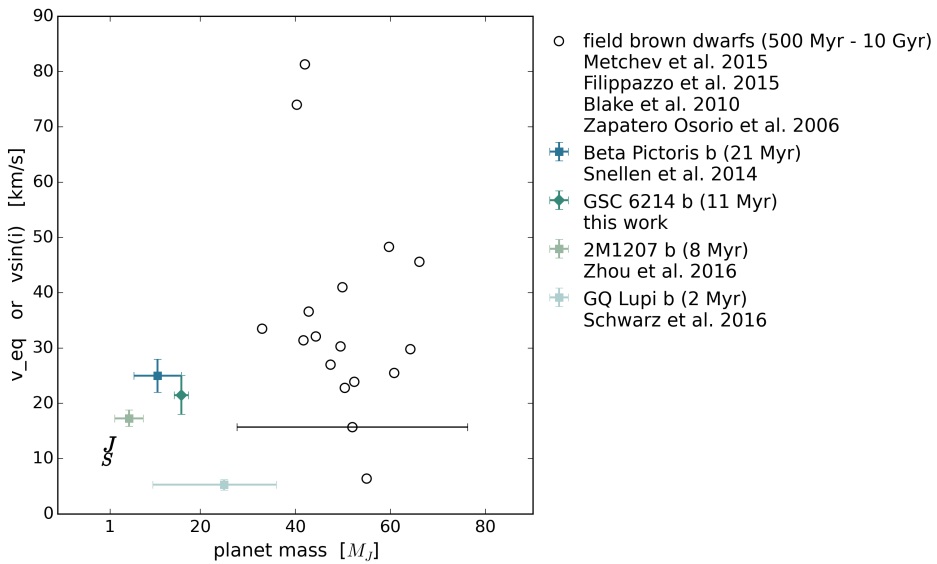
Figure 4.6: Spin as a function of mass for extrasolar substellar companions, together with Jupiter and Saturn, and a sample of field brown dwarfs. The solar system planets and 2M1207 b have equatorial rotation velocities and β Pictoris b, GQ Lupi b and GSC 6214 b have projected rotational velocities. For comparison, field brown dwarfs with estimated masses and either a rotational period measurement or $v \sin(i)$ measurement are shown as empty circles, with the typical uncertainty in mass indicated for a single object.

on an object to object basis, the obliquity can also play a major role, meaning that comparative analyses can only be conducted in a strict statistical way with a larger sample.

4.7 Conclusions

We successfully observed the substellar companion GSC 06214-00210b with the high-dispersion CRIRES spectrograph on ESO's Very Large Telescope at 2.3 µm targeting the carbon monoxide band. CO is detected at a S/N of 5.3 but H_2O is not seen. We measure a projected rotational velocity of $21.5 \pm 3.5 \,\mathrm{km\,s^{-1}}$ from fitting the shape of the CO cross-correlation signal with model cross-correlation functions with varying rotational broadening. The radial velocity of the companion is consistent with that of the star, as expected for the wide orbital separation of 320 au.

References

Arsenault, R., J. Alonso, H. Bonnet, J. Brynnel, B. Delabre, R. Donaldson, C. Dupuy, E. Fedrigo, J. Farinato, N. N. Hubin, L. Ivanescu, M. E. Kasper, J. Paufique, S. Rossi, S. Tordo, S. Stroebele, J.-L. Lizon, P. Gigan, F. Delplancke, A. Silber, M. Quattri, and R. Reiss
2003. MACAO-VLTI: An Adaptive Optics system for the ESO VLT interferometer. In *Adaptive Optical System Technologies II*, P. L. Wizinowich and D. Bonaccini, eds., volume 4839 of *Society of Photo-Optical Instrumentation Engineers (SPIE) Conference Series*, Pp. 174–185.

Barman, T. S., Q. M. Konopacky, B. Macintosh, and C. Marois
2015. Simultaneous Detection of Water, Methane, and Carbon Monoxide in the Atmosphere of Exoplanet HR8799b. *ApJ*, 804:61.

Blake, C. H., D. Charbonneau, and R. J. White
2010. The NIRSPEC Ultracool Dwarf Radial Velocity Survey. *ApJ*, 723:684–706.

Borysow, A.
2002. Collision-induced Absorption Coefficients of H_2 Pairs at Temperatures from 60 K to 1000 K. *A&A*, 390:779.

Borysow, A., U. G. Jørgensen, and Y. Fu
2001. High-temperature (1000-7000k) Collision-induced Absorption of H_2 Pairs Computed from the First Principles, with Application to Cool and Dense Stellar Atmospheres. *J. Quant. Spec. Radiat. Transf.*, 68(3):235.

Boss, A. P.
1997. Giant planet formation by gravitational instability. *Science*, 276:1836–1839.

Boss, A. P.
2000. Possible Rapid Gas Giant Planet Formation in the Solar Nebula and Other Protoplanetary Disks. *ApJ*, 536:L101–L104.

Bowler, B. P., S. M. Andrews, A. L. Kraus, M. J. Ireland, G. Herczeg, L. Ricci, J. Carpenter, and M. E. Brown
2015. An ALMA Constraint on the GSC 6214-210 B Circum-substellar Accretion Disk Mass. *ApJ*, 805:L17.

Bowler, B. P., M. C. Liu, A. L. Kraus, and A. W. Mann
  2014. Spectroscopic Confirmation of Young Planetary-mass Companions on
  Wide Orbits. *ApJ*, 784:65.

Bowler, B. P., M. C. Liu, A. L. Kraus, A. W. Mann, and M. J. Ireland
  2011. A Disk around the Planetary-mass Companion GSC 06214-00210 b:
  Clues about the Formation of Gas Giants on Wide Orbits. *ApJ*, 743:148.

Brogi, M., R. J. de Kok, S. Albrecht, I. A. G. Snellen, J. L. Birkby, and H. Schwarz
  2016. Rotation and Winds of Exoplanet HD 189733 b Measured with High-
  dispersion Transmission Spectroscopy. *ApJ*, 817:106.

Burrows, A., W. B. Hubbard, J. I. Lunine, and J. Liebert
  2001. The theory of brown dwarfs and extrasolar giant planets. *Reviews of
  Modern Physics*, 73:719–765.

de Zeeuw, P. T., R. Hoogerwerf, J. H. J. de Bruijne, A. G. A. Brown, and
  A. Blaauw
  1999. A HIPPARCOS Census of the Nearby OB Associations. *AJ*, 117:354–
  399.

Filippazzo, J. C., E. L. Rice, J. Faherty, K. L. Cruz, M. M. Van Gordon, and D. L.
  Looper
  2015. Fundamental Parameters and Spectral Energy Distributions of Young
  and Field Age Objects with Masses Spanning the Stellar to Planetary Regime.
  ApJ, 810:158.

Horne, K.
  1986. An optimal extraction algorithm for CCD spectroscopy. *PASP*, 98:609–
  617.

Hubickyj, O., P. Bodenheimer, and J. J. Lissauer
  2005. Accretion of the gaseous envelope of Jupiter around a 5 10 Earth-mass
  core. *Icarus*, 179:415–431.

Hughes, D. W.
  2003. Planetary spin. *Planet. Space Sci.*, 51:517–523.

Husser, T.-O., S. Wende-von Berg, S. Dreizler, D. Homeier, A. Reiners, T. Bar-
  man, and P. H. Hauschildt
  2013. A new extensive library of PHOENIX stellar atmospheres and synthetic
  spectra. *A&A*, 553:A6.

Ireland, M. J., A. Kraus, F. Martinache, N. Law, and L. A. Hillenbrand
    2011. Two Wide Planetary-mass Companions to Solar-type Stars in Upper Scorpius. *ApJ*, 726:113.

Jones, A., S. Noll, W. Kausch, C. Szyszka, and S. Kimeswenger
    2013. An advanced scattered moonlight model for Cerro Paranal. *A&A*, 560:A91.

Kaeufl, H.-U., P. Ballester, P. Biereichel, B. Delabre, R. Donaldson, R. Dorn, E. Fedrigo, G. Finger, G. Fischer, F. Franza, D. Gojak, G. Huster, Y. Jung, J.-L. Lizon, L. Mehrgan, M. Meyer, A. Moorwood, J.-F. Pirard, J. Paufique, E. Pozna, R. Siebenmorgen, A. Silber, J. Stegmeier, and S. Wegerer
    2004. CRIRES: a high-resolution infrared spectrograph for ESO's VLT. In *Ground-based Instrumentation for Astronomy*, A. F. M. Moorwood and M. Iye, eds., volume 5492 of *Society of Photo-Optical Instrumentation Engineers (SPIE) Conference Series*, Pp. 1218–1227.

Lachapelle, F.-R., D. Lafrenière, J. Gagné, R. Jayawardhana, M. Janson, C. Helling, and S. Witte
    2015. Characterization of Low-mass, Wide-separation Substellar Companions to Stars in Upper Scorpius: Near-infrared Photometry and Spectroscopy. *ApJ*, 802:61.

Laughlin, G., P. Bodenheimer, and F. C. Adams
    2004. The Core Accretion Model Predicts Few Jovian-Mass Planets Orbiting Red Dwarfs. *ApJ*, 612:L73–L76.

López-Morales, M., N. Gómez-Pérez, and T. Ruedas
    2011. Magnetic Fields in Earth-like Exoplanets and Implications for Habitability around M-dwarfs. *Origins of Life and Evolution of the Biosphere*, 41:533–537.

Metchev, S. A., A. Heinze, D. Apai, D. Flateau, J. Radigan, A. Burgasser, M. S. Marley, É. Artigau, P. Plavchan, and B. Goldman
    2015. Weather on Other Worlds. II. Survey Results: Spots are Ubiquitous on L and T Dwarfs. *ApJ*, 799:154.

Moses, J. I., M. S. Marley, K. Zahnle, M. R. Line, J. J. Fortney, T. S. Barman, C. Visscher, N. K. Lewis, and M. J. Wolff
    2016. On the Composition of Young, Directly Imaged Giant Planets. *ApJ*, 829:66.

Noll, S., W. Kausch, M. Barden, A. M. Jones, C. Szyszka, S. Kimeswenger, and J. Vinther
2012. An atmospheric radiation model for Cerro Paranal. I. The optical spectral range. *A&A*, 543:A92.

Parker, E. N.
1955. Hydromagnetic Dynamo Models. *ApJ*, 122:293.

Pecaut, M. J., E. E. Mamajek, and E. J. Bubar
2012. A Revised Age for Upper Scorpius and the Star Formation History among the F-type Members of the Scorpius-Centaurus OB Association. *ApJ*, 746:154.

Pollack, J. B., O. Hubickyj, P. Bodenheimer, J. J. Lissauer, M. Podolak, and Y. Greenzweig
1996. Formation of the Giant Planets by Concurrent Accretion of Solids and Gas. *Icarus*, 124:62–85.

Preibisch, T., A. G. A. Brown, T. Bridges, E. Guenther, and H. Zinnecker
2002. Exploring the Full Stellar Population of the Upper Scorpius OB Association. *AJ*, 124:404–416.

Preibisch, T. and E. Mamajek
2008. *The Nearest OB Association: Scorpius-Centaurus (Sco OB2)*, P. 235.

Rothman, L. S., I. E. Gordon, R. J. Barber, H. Dothe, R. R. Gamache, A. Goldman, V. I. Perevalov, S. A. Tashkun, and J. Tennyson
2010. HITEMP, the High-Temperature Molecular Spectroscopic Database. *J. Quant. Spec. Radiat. Transf.*, 111(15):2139.

Rucinski, S.
1999. Determination of Broadening Functions Using the Singular-Value Decomposition (SVD) Technique. In *IAU Colloq. 170: Precise Stellar Radial Velocities*, J. B. Hearnshaw and C. D. Scarfe, eds., volume 185 of *Astronomical Society of the Pacific Conference Series*, P. 82.

Schwarz, H., C. Ginski, R. J. de Kok, I. A. G. Snellen, M. Brogi, and J. L. Birkby
2016. The slow spin of the young substellar companion GQ Lupi b and its orbital configuration. *A&A*, 593:A74.

Showman, A. P. and Y. Kaspi
2013. Atmospheric Dynamics of Brown Dwarfs and Directly Imaged Giant Planets. *ApJ*, 776:85.

Showman, A. P., N. K. Lewis, and J. J. Fortney
   2015. 3D Atmospheric Circulation of Warm and Hot Jupiters. *ApJ*, 801:95.

Showman, A. P., R. D. Wordsworth, T. M. Merlis, and Y. Kaspi
   2013. *Atmospheric Circulation of Terrestrial Exoplanets*, Pp. 277–326.

Snellen, I. A. G., B. R. Brandl, R. J. de Kok, M. Brogi, J. Birkby, and H. Schwarz
   2014. Fast spin of the young extrasolar planet β Pictoris b. *Nature*, 509:63–65.

Zapatero Osorio, M. R., E. L. Martín, H. Bouy, R. Tata, R. Deshpande, and R. J. Wainscoat
   2006. Spectroscopic Rotational Velocities of Brown Dwarfs. *ApJ*, 647:1405–1412.

Zhou, Y., D. Apai, G. H. Schneider, M. S. Marley, and A. P. Showman
   2016. Discovery of Rotational Modulations in the Planetary-mass Companion 2M1207b: Intermediate Rotation Period and Heterogeneous Clouds in a Low Gravity Atmosphere. *ApJ*, 818:176.

Zhou, Y., G. J. Herczeg, A. L. Kraus, S. Metchev, and K. L. Cruz
   2014. Accretion onto Planetary Mass Companions of Low-mass Young Stars. *ApJ*, 783:L17.

5 | Spin measurements of young sub-stellar companions: The case of HIP 78530 b

In collaboration with:
Matteo Brogi, Jayne Birkby, Ignas Snellen, Remco de Kok
In preparation

The chapter descibes the observations and analyses of the fourth and final object of a small CRIRES survey with the aim to measure the spin of young sub-stellar companions. The target, HIP 78530 b is orbiting its host star at a projected distance of $\sim$700 au, and has an estimated mass of 23 M_J at an age of 11 Myr, which suggests the brown dwarf is currently in its deuterium burning phase. At the wavelength of 2.3 μm we detect both carbon monoxide and water, and measure a $v\sin(i)$ of $12^{+2}_{-1.5}$ km s^{-1} from the rotational broadening of the lines. We make a first attempt to conduct comparitive planetology and study the spin parameters of the sample as a whole. Although the observed sample is small, we do see a correlation of spin velocity with age, which we interpret as due to the youngest objects still accreting angular momentum and their spin up through subsequent cooling and contraction.

5.1 Introduction

A planet spin rate is a fundamental observable affecting its climate, atmospheric dynamics, and magnetic field. In addition, it may shed light on its formation process and evolution. Our team has performed a small survey aimed to determine the rotation velocities of young substellar companions. Central to these observations is the combination of high-dispersion spectroscopy and high contrast imaging through adaptive optics techniques (Snellen et al., 2015). High dispersion spectroscopy is required to measure the rotational broadening of the lines. Adaptive optics is needed to suppress the scattered light from the host star at the position of the companion. In a pilot study (Snellen et al., 2014) we tested this technique on the directly imaged exoplanet β Pictoris b using the Cryogenic High-Resolution

Infrared Echelle Spectrograph (CRIRES; Kaeufl et al., 2004) on the Very Large Telescope (VLT). Subsequently, three more substellar companions were observed with CRIRES before it was taken off the telescope in July 2014 for a major upgrade. The upgraded instrument, CRIRES+ (Follert et al., 2014), will among other things be cross-dispersed resulting in an increase in instantaneous wavelength coverage by an order of magnitude. We observed the substellar companions GQ Lupi b, GSC 6214-210 b, and HIP 78530 b. They have estimated masses in the range 10-25 M_J, ages between 1 and 20 Myr, and projected orbital distances between 10 and 700 au.

This chapter describes the observations and analyses of the final target, HIP 78530 b. In Section 5.2 we characterise the HIP 78530 system, and in Section 5.3 we give the details of the observations. Sections 5.4 and 5.5 describe the data analyses, and the results are presented in Section 5.6. In Section 5.7 we conduct a comparative study from the survey. The conclusions are summarised in Section 5.8.

5.2   The HIP 78530 system

The HIP 78530 system (or alternatively HD 143567) is located in Upper Scorpius which is the youngest subgroup of the nearest OB association to the Earth. The primary is a bright (K = 6.9) blue B-type star on or near the main-sequence, with an estimated mass of 2.5 $M_\odot$ and an effective temperature of 10 500 K. The typical age of an Upper Scorpius member has been determined from isochrone fitting to 11 Myr (Pecaut et al., 2012), although a previous estimate from low-mass evolutionary models set the age to 5 Myr (Preibisch et al., 2002). Regardless, the intrinsic age dispersion of the subgroup is found to be small, on the order of a few million years (Preibisch and Mamajek, 2008; Pecaut et al., 2012).

The substellar companion HIP 78530 b was discovered by Lafrenière et al. (2011) as part of a direct imaging search in Upper Scorpius with the Gemini North Telescope. It is located 4.5″ to the south-east of the host star, corresponding to a projected separation of 710 au at 157 pc. The companion had in fact been detected previously by Kouwenhoven et al. (2005, 2007), yet it was not possible from their data to distinguish between a background star and a companion. Lafrenière et al. (2011) observed the object with both photometry and medium-resolution spectroscopy in the near-infrared (NIR) and made use of a 2-year baseline to confirm the companion nature. They determined the spectral type (M8) and estimated the effective temperature (2800 K) and mass (23 M_J) from comparison with synthetic spectra. However, Bailey et al. (2013) matched the 1 to 4 μm colours to a spectral type M3±2, thus questioning if the object is perhaps a background low-mass star,

rather than a brown dwarf companion. This concern was laid to rest by Lachapelle et al. (2015). They extended the available photometric data to include the Y-band and obtained medium resolution spectroscopy in the 0.9 to 1.15 μm range. This allowed them to extend the baseline of the archival data by one year, increasing the significance of the companion claim to 10σ. Moreover, the new spectra were fully consistent with the spectral type, mass and effective temperature reported by Lafrenière et al. (2011).

The mass and age of HIP 78530 b suggest that it is in a quasi-stable deuterium burning phase. Although the system is young, there is no observational evidence of circumstellar or circum-substellar disk material (Bailey et al., 2013). The combination of a B-type star and a brown dwarf companion is unusual, as is the extremely wide orbit. The existence of such a system blurs the distinction between planetary systems and stellar binaries and is a challenge to current formation theories.

Table 5.1: HIP 78530 system properties. Alternative identifier HD 143567 Ab.

Property	HIP 78530 A	HIP 78530 b
Spectral type	B9V[i]	M8 $\pm$ 1[ii]
Teff [K]	~ 10500[iii]	2800 ± 200[ii]
Mass	$\sim 2.5\ \mathrm{M_\odot}$[iv]	$23 \pm 4\ \mathrm{M_J}$[v]
P.A. [deg][ii]		140.3 ± 0.1
Ang. sep. ["][ii]	4.533 ± 0.006	
ΔK [mag][ii]	7.26 ± 0.04	
Distance [pc][vi]	156.7 ± 13	
v_{sys} [km/s][vii]	-9.0 ± 4.4	
Age [Myr][viii]	11 ± 2	

[i] Houk and Smith-Moore (1988)
[ii] Lafrenière et al. (2011)
[iii] From the spectral type, based on the temperature scale of Sherry et al. (2004)
[iv] From the models of D'Antona and Mazzitelli (1997)
[v] From the models of Baraffe et al. (1998, 2002); Burrows et al. (1997)
[vi] From the parallax of van Leeuwen (2007)
[vii] Gontcharov (2006)
[viii] Pecaut et al. (2012)

5.3   Observations

We observed the HIP 78530 system for two nights in 2014, on May 29 and June 20, as part of the ESO programme 293.C-5012(A). The observations were carried out with the high-dispersion spectrograph CRIRES at the VLT on Cerro Paranal in Chile. The first night, seeing was reported to be below the requirement of 1″, and as a result the target was observed again in June. Both nights we obtained a standard set of calibration frames and 18 science exposures of 120 seconds each. The target was observed in the K-band, centered on 2.3 μm with the standard wavelength settings for order 24. The CRIRES instrument has four Aladdin III InSB detectors (1024 x 512 pixels) which are separated by physical gaps corresponding to approximately 280 pixels. We excluded the first detector from the the data analysis, because there were very few CO lines within the wavelength range, and the detector suffered from a well-known non-linearity issue[1].

In order to maximise the spectral resolution, we applied the smallest choice of slit width (0.2″), and from our analysis of the stellar spectra, we find we have achieved a typical resolving power of 90 000. CRIRES is a long-slit spectrograph, and we aligned the slit with the position angle of the companion ($P.A. = 140.3°$, Lafrenière et al., 2011), thus observing the host star and the companion simultaneously. The companion is spatially resolved from the primary with an angular separation of 4.5″(Lafrenière et al., 2011), however, the K-band contrast ratio is 1.25×10^{-3}, and the high contrast requires the use of excellent adaptive optics. We made use of the Multi Application Curvature Adaptive Optics system (MACAO, Arsenault et al., 2003) which has the effect of both suppressing the star light and maximising the throughput.

For the major part, the observations were carried out under clear sky conditions, although on the second night there were thin cirrus clouds present for part of the observations. The airmasses were low (1.1 to 1.2), but the seeing varied considerably during both observing nights (see Table 5.2). The telescope was operated in a nodding mode, i.e. the pointing was changed sequentially by 10″ along the slit direction in a classical ABBA pattern between two positions, A and B, to allow accurate background subtraction. A small random jitter was added to each nod to improve flatfielding and hot pixel corrections.

Table 5.2: Details for the observing nights

	2014-05-29	2014-06-20
total time [min][i]	46	46
# of exposures[ii]	18	18
DIT [s][iii]	120	120
NDIT[iv]	1	1
airmass	1.1-1.2	1.1
sky conditions	clear	clear & thin cirrus
seeing [”][v]	0.9–2.95	0.5–2.85
FWHM star [”][vi]	0.23–0.33	0.19–0.31

[i] total observing time for the science exposures
[ii] total number of exposures
[iii] detector integration time
[iv] number of integrations per nod
[v] seeing range as reported in the observing log
[vi] range of measured full-width-half-maxima of the stellar profiles along the slit from the (AO-corrected) AB-combined frames

5.4   Data analysis

5.4.1   Basic data reduction

The two nights were treated individually, yet in the exact same way. The basic data reduction was performed with recipes from the CRIRES pipeline version 2.3.2 and processed with the EsoRex tool version 3.10.2. The pipeline performed dark-subtraction, flatfielding, and corrected for known bad pixels and non-linearity effects. Furthermore, EsoRex was used to combine the science frames in AB nodding pairs, thus performing a background subtraction. This resulted in a total of 9 two-dimensional spectra per night which were the starting point of the remaining analysis. The one-dimensional spectra of the star HIP 78530 A were also extracted with EsoRex from the two-dimensional AB-combined frames, applying the option of optimal extraction (Horne, 1986).

The two-dimensional spectra had the wavelength bins along the x-axis and the slit position along the y-axis. The frames were aligned in the spatial direction using the centroid of the stellar spectral trail as the reference. We cut out the rows further

---

[1]http://www.eso.org/sci/facilities/paranal/instruments/crires/doc/VLT-MAN-ESO-14500-3486_v93.pdf
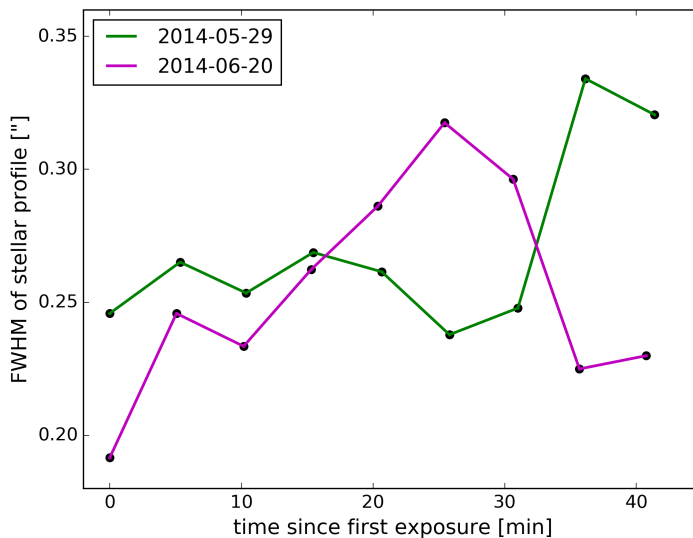
Figure 5.1: The full-width-half-maximum (FWHM) of the stellar profile along the slit direction is a proxy for the seeing, although the values will be smaller, because the two-dimensional spectra are AO-corrected. We measured the FWHM of the individual frames with a Lorentzian fit to the average stellar profile and applied this as the weights when constructing a weighted average two-dimensional spectrum for each night.

away from the stellar centroid than 100 pixels, corresponding to $\sim 8.6''$. Despite the build-in bad pixel correction of the CRIRES pipeline, the frames suffered from multiple dead pixels, hot pixels and cosmic ray hits. At distances more than $2''$ from the stellar centroid we identified bad pixels as 5σ outliers, and set their values to zero which was the mean value for pixels sufficiently far from the star to not contain scattered stellar light. The central rows $< 2''$ from the stellar centroid were not corrected for bad pixels prior to combining the frames, but instead the average frame were inspected for bad pixels.

The 9 frames were combined with a weighted average, where the weights were related to the seeing. As a seeing proxy, we made use of the full-width-half-maximum (FWHM) of the stellar point spread function. For each frame, the FWHM was determined from a Lorentzian fit to the average stellar profile along the slit direction, and it was applied as the weight of the given frame. The fitted FWHM values for both nights are shown in Fig. 5.1. It can be seen that the seeing varied considerably during both nights, but that the nights were similar on average.

The average two-dimensional spectrum was visually identified with the pro-

gramme DS9 and then corrected with cubic spline interpolation using the four nearest neighbours in the row. Strictly speaking, this was not necessary in order to extract the spectrum of the companion, but it has the advantage that the spectral trail is clearly visible in the average two-dimensional spectrum (Fig. 5.2A). To help guide the eye to the faint trail of the companion, the location is indicated with the letter 'b' on the right-hand axes.

The one-dimensional stellar spectra were treated in a similar manner. Bad pixels were visually identified and corrected with cubic spline interpolation from neighbouring pixels, and the frames were combined to a weighted average using the same weights as for the two-dimensional case.

5.4.2   Extraction of spectra for each slit position

We optimally extracted a spectrum for each slit position from the average two-dimensional spectrum (Fig. 5.2A), performing the procedure individually for the three detectors. This was done by creating a map of the stellar profiles along the slit (Fig. 5.2B) and then for each slit position we extracted a spectrum as a weighted average of the closest ± 10 slit positions with the weights determined from the profile map. The map was constructed by fitting the curvature in the stellar continuum for each of the 21 most central rows. We will refer to the extracted spectra collectively as the spatial spectra. An example from the first night, detector 4, is displayed in Fig. 5.2C. The peak intensity of the spectral trail of this detector shifts by 10 pixels in the spatial direction from one end of the detector to the other (Fig. 5.2A and 5.2B), but following the optimal extraction, the tilt is fully corrected (5.2C).

The stellar spectrum of a B-type star such as HIP 78530 A is featureless in the near infrared, but the observed stellar spectrum contains telluric lines. It is described how we extracted the one-dimensional stellar spectrum in Sec. 5.4.1, and we made use of this as a reference spectrum to remove the telluric contamination from the spatial spectra, including at the position of the companion. The reference spectrum was scaled to the flux level of the given slit position and subtracted from the spatial spectrum, followed by a normalisation. The resulting residual spatial spectra are shown in Fig. 5.2D.

The location of the companion spectrum on the detectors fall halfway between two rows of pixels, and in the following cross-correlation analysis we used the average spectrum of those two rows in the one-dimensional treatment, from which we determine the projected rotational velocity ($v \sin(i)$) of the companion. The final thermal spectrum from combining the two nights is displayed in Fig. 5.6. It is described in Sec. 5.5.2 how the weights of the two different nights were determined.

As a starting point for the wavelength solution we made use of a previous solution from the data analysis of GSC 6214-210 (Chapter 3), which was observed on
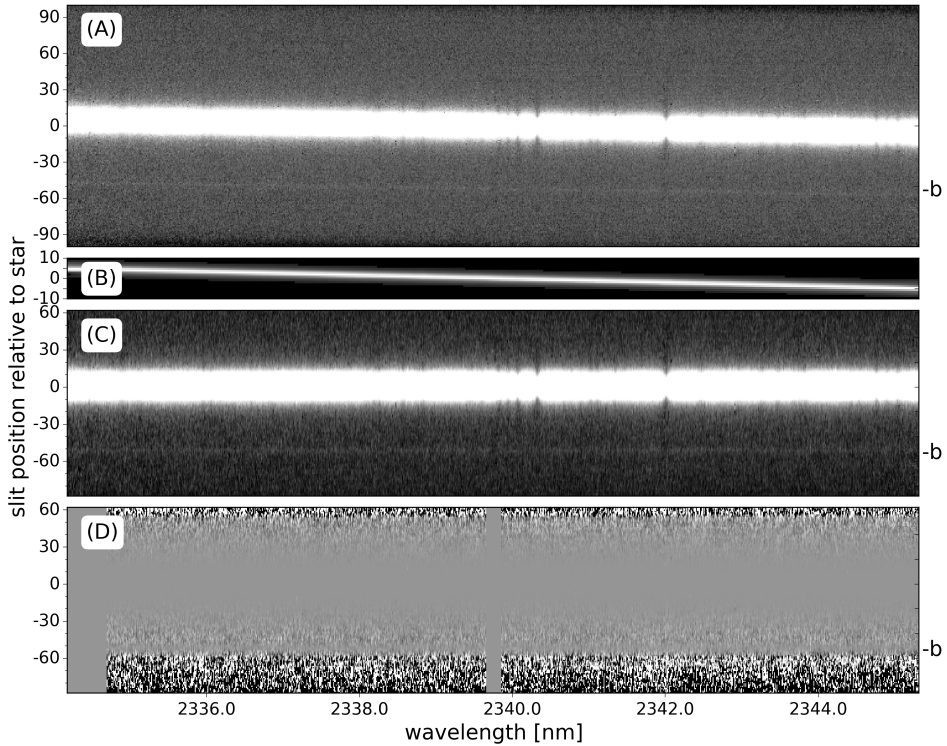
Figure 5.2: Illustration of the data analysis steps from detector 4 as observed on 2014-05-29. The *y*-axes depicts the slit position relative to the average centroid of the stellar profile. The companion position is indicated by a 'b' on the right-hand axes. The greyscales were adjusted individually for each array with an IRAF-like z-scale algorithm. *Top to bottom:* (A) The average two-dimensional spectrum, where the individual AB-combined frames were weighted by the FWHM of the stellar profile as given in Fig. 5.1. (B) A map of the stellar profiles made by fitting the continuum of each of the central rows. (C) The spatial spectra, extracted by applying the stellar profile map as weights for each slit position. Each row corresponds to an optimally extracted spectrum for the given slit position. (D) The residual spatial spectra after removing the scaled stellar spectrum, dominated by telluric lines.

the same night as one of the two nights of the HIP 78530 data set. The wavelength solution was updated for both nights through cross-correlating with a template telluric spectrum. The template spectrum was a sky transmission model from ESO SkyCalc[2] with the airmass set to 1.1 and the precipitable water vapor set to the seasonal average for the Cerro Paranal observing site.

---

[2]https://www.eso.org/observing/etc/skycalc

5.5   Cross-correlation analysis

The cross-correlation analysis we applied to the HIP 78530 data set followed the procedures of Chapters 2 and 3, incorporating the best elements from each of the two slightly different approaches. The concept is that although the companion spectrum is observed with a low S/N, molecules can be uniquely identified by cross-correlating with template spectra, and the rotational broadening can be measured from the shape of the cross-correlation signal. This works because the cross-correlation function (CCF) collects the signal from all of the molecular lines within the wavelength range, and because the shape of the CCF is sensitive to the average shape of the individual molecular lines. The cross-correlation signal also reveals the radial velocity (RV) of the companion.

For consistency we used the same three models which were applied in the cross-correlation analyses of GQ Lupi b (Chapter 2) and GSC 6214-210 b (Chapter 3). These are: a CO model, a H_2O model, and a model containing both CO and H_2O. Fig. 2 in Chapter 3 illustrates the three models for the same wavelength coverage which was used in this work, and the details of the models are given in Sec. 5.1. The model spectrum was convolved to the spectral resolution of CRIRES (90 000), then Doppler shifted over the range $-200\,\mathrm{km\,s^{-1}}$ to $200\,\mathrm{km\,s^{-1}}$ in steps of $1.5\,\mathrm{km\,s^{-1}}$, and cross-correlated with the residual spatial spectra. The cross-correlation was performed separately for each night and each detector.

5.5.1   Molecular detection maps

In an analogous manner to Sec. 5.2 of Chapter 2, we cross-correlated the entire array of residual spatial spectra with a model, producing what we will call a 'molecular detection map'. A row in the map corresponds to the CCF for the spectrum of a particular slit position, and the map thus provides an illustration of the strength of the cross-correlation as a function of slit position and radial velocity. If the molecule(s) in the model is present in the observed spectrum of the companion, this will give rise to an intensity peak at the known angular separation from the star and at a radial velocity which is consistent with the systemic velocity. Performing the cross-correlations for the entire array provides a means to investigate the strength of spurious signals.

5.5.2   Measuring the companion $v\sin(i)$ and RV

As described in Sec. 5.4.2, we have defined the companion spectrum as the average of the two rows of the residual spatial spectrum array which contain significant flux from the companion. We will refer to the CCF from the companion spectrum

and one of the models, as a *measured CCF*. We followed the procedures of Sec.
5.2 in Chapter 3, as well as the nomenclature for the cross-correlation functions
as given in Table 2 of Chapter 3. In particular, we applied the same approach to
determine the relative weights of the two nights and of the detectors. The principle
is to inject the model spectrum into the companion spectrum, and then retrieving
it through the cross-correlation with the same model. Subtracting the *measured
CCF* from the *injected CCF* provides an estimate of the expected cross-correlation
signal. The weights are then determined as the ratio of the signal estimate to the
standard deviation of the *measured CCF* of the given night and detector (eq. 2,
Chapter 3). The weights take several factors into account: the strength and number
of lines of a given detector, and the data quality of the given night and detector.
The weights were normalised and applied when combining the data or the CCFs
from the two nights and the three detectors. For example when combining the
molecular detection maps, the applied weights were determined from injecting
the appropriate model. The weights from the CO model was applied to combine
the companion spectra of the two nights into the final thermal spectrum as shown
in Fig. 5.3.

The projected rotational velocity and the radial velocity of the companion were
determined by fitting *model CCFs* to the signal of the *measured CCF*. The *model
CCFs* were constructed by cross-correlating the model with a rotationally broad-
ened and Doppler shifted version of itself. We tested $v \sin(i)$ values in the range
$0 \, \mathrm{km \, s^{-1}}$ to $60 \, \mathrm{km \, s^{-1}}$ and Doppler shifts in the range $-20 \, \mathrm{km \, s^{-1}}$ to $10 \, \mathrm{km \, s^{-1}}$,
both with step sizes of $0.5 \, \mathrm{km \, s^{-1}}$. The *model CCFs* were scaled and offset (*y*-
direction) with a least squares fit to the *measured CCF*. The best fit $v \sin(i)$ and
RV values were determined with $\mathcal{X}^2$ minimisation, and the confidence intervals
were determined from rescaling the errors so $\bar{\mathcal{X}}^2 = 1$. All radial velocities in the
results are given in the heliocentric frame.

5.6   Results

We have measured the high-dispersion $2.3 \, \mu\mathrm{m}$ thermal spectrum of the substellar
companion HIP 78530 b. The spectrum is shown in Fig. 5.3. We achieved a S/N
of the spectrum of 1.8 in detector 2, and 2.2 in detectors 3 and 4. In general, the
individual molecular lines of the thermal spectrum are hidden within the noise,
yet hints of the most prominent CO absorption lines can be seen in detectors 3
and 4. A particularly recognisable feature is the CO band-head in detector 3 at
$\sim 2322.6 \, \mathrm{nm}$.

The presence of CO in the atmosphere of HIP 78530 b is confirmed by the
cross-correlation analysis, and we also detect H_2O. Fig. 5.4 displays the molecule
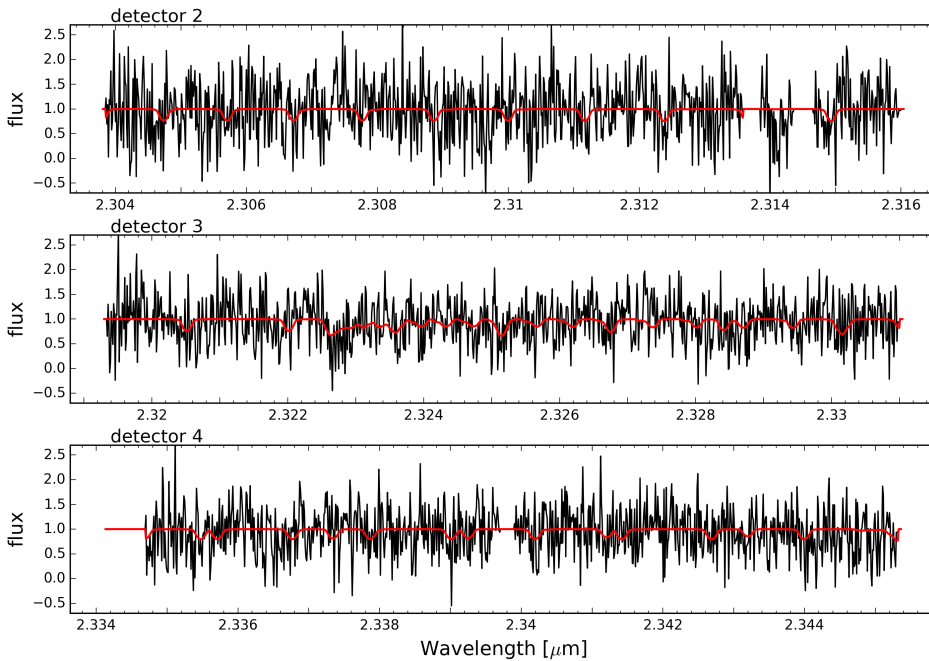
Figure 5.3: The thermal spectrum of HIP 78530 b (black). The individual observing nights were combined as a weighted average, where the weights were determined as part of the cross-correlation analysis. The red line is the CO model, convolved to the CRIRES spectral resolution, rotationally broadened to match the measured $v \sin(i)$ of $12 \, \mathrm{km \, s^{-1}}$, and Doppler shifted to match the systemic velocity of $-9 \, \mathrm{km \, s^{-1}}$.

detection maps for the three models: Single-trace-gas models with CO or H_2O, and a model containing traces of both molecules. The residual spatial spectra (Fig. 5.2D) were cross-correlated with the models, so that each row of the molecule detection map is the CCF for a given position along the slit of the spectrograph. A strong signal is seen at the expected distance from the star and at a radial velocity corresponding to the systemic velocity for both the CO and CO+H_2O model. They have peak S/N values of 5.4 and 6.2, respectively. The H_2O model gives rise to a weaker signal with a peak S/N of 3.8. The water detection is seen more clearly in Fig. 5.5, which is the same as Fig. 5.4 which is a zoom-in focusing on the parameter space close to the expected position of the companion. Although the water cross-correlation signal is weak, it is located at the expected position and radial velocity.

The peak S/N values were detemined as the peak value divided through the standard deviation of the full molecular detection map in Fig. 5.4, exempting a

small region around the expected position and radial velocity. The peak S/N values underestimate the significance of the detections, because the signal is intrinsically broad, and therefore is spread over several pixels in the radial velocity direction. We used the same approach as in Chapter 3, and estimated the S/N of the molecular detections as the peak value of the CCF between the observed spectrum and the best fit rotationally broadened model, divided with the standard deviation of the difference between that same *broad measured CCF* and the auto-correlation function of the rotationally broadened model. From this we find that CO is detected with a S/N of 9.8, H_2O with one of 3.5 and the $CO+H_2O$ model is detected with a S/N of 9.4.

Already from Fig. 5.5 it can be seen that the cross-correlation signal is broadened, not only from CO, but also water. We measure the rotational broadening from the cross-correlation between the CO model and the extracted companion spectrum as given in Fig. 5.3. The resulting one-dimensional cross-correlation function is shown in Fig. 5.6. The $v \sin(i)$ and radial velocity is determined by fitting this *measured CCF* with *model CCFs*, minimising the $\mathcal{X}^2$, as described in Section 5.5.2. We find that the best fit *model CCF* has a **$v \sin(i)$ of $12^{+2.0}_{-1.5}$ km s^{-1}** and an **RV of -9.5 ± 1.0 km s^{-1}**. The $v \sin(i)$ measurement is intermediate compared to the few existing measurements for other sub-stellar companions. The comparison is further discussed in Sec. 5.7. The measured radial velocity is fully consistent with the systemic velocity (9 km s^{-1}), as expected for a companion orbiting $\sim$710 au from the central star. The expected circular orbital velocity at the observed orbital distance of HIP 78530 b is 1.8 km s^{-1}.

The orientation of the spin axis of HIP 78530 b is unknown, and therefore the measured projected rotational velocity can only be considered a lower limit on the equatorial rotation velocity. Assuming the object is viewed edge-on, the measured spin velocity corresponds to a rotational period of 26 hours, where we have applied an estimated radius of 2.5 R_J. The radius estimate is based on the effective temperature and luminosity as measured by Lachapelle et al. (2015), and checked against brown dwarfs cooling models by Burrows et al. (2001). The radius should be quasi-stationary for a few million years, yet eventually the intensity of the deuterium burning will diminish, and the radius will contract towards 1 R_J, causing the brown dwarf to spin-up to a rotational velocity of 30 ± 7 km s^{-1}.
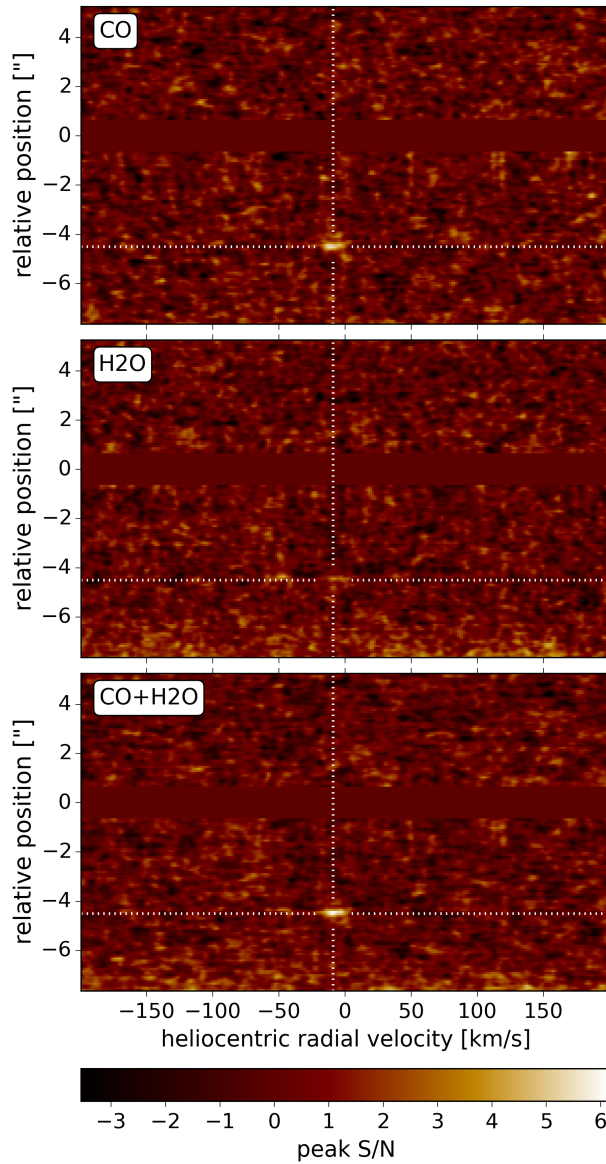
Figure 5.4: Molecule detection maps for the CO, H_2O and CO+H_2O models. The colour scale indicates the strength of the cross-correlation as a function of radial velocity and slit position relative to the host star. The expected position of the planet is indicated by the white dotted lines, corresponding to the systemic velocity and the known angular separation of the companion. The companion is detected for all three models. See also Fig. 5.5 for the enlarged images centered on the companion signals.

Figure 5.5: Same as Fig. 5.4, but centered around the planet signals and enlarged to show the details. The peak S/N values are 5.4 for CO, 3.8 for H_2O, and 6.2 for the CO+H_2O model. The pe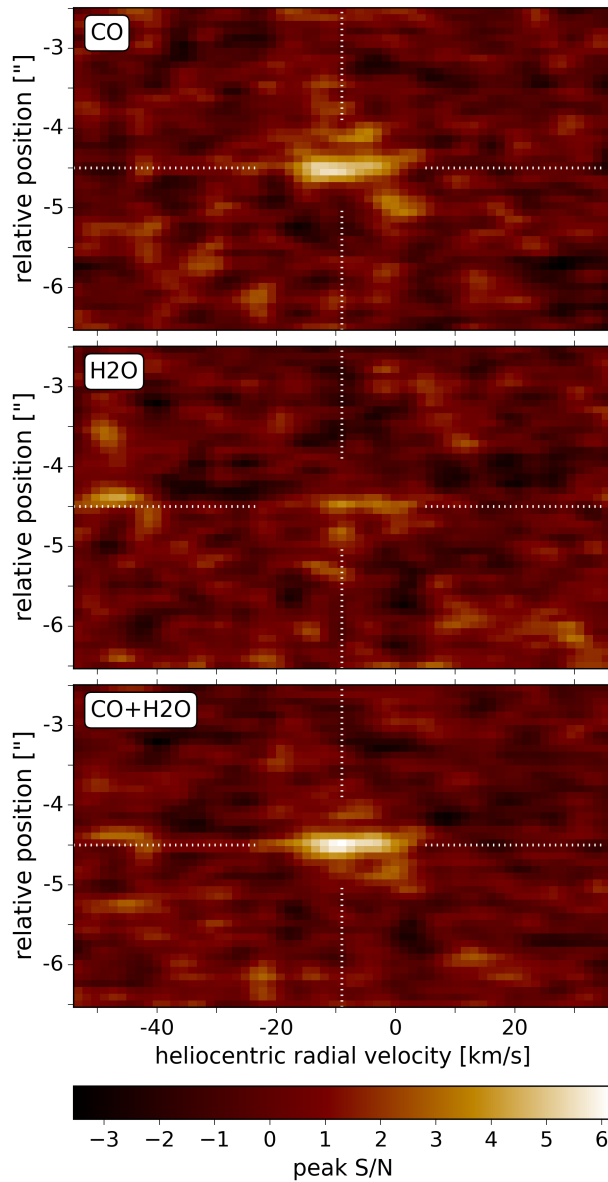ak S/N values underestimate the significance of the molecular detections, since this is the cross-correlation with the unbroadened models.
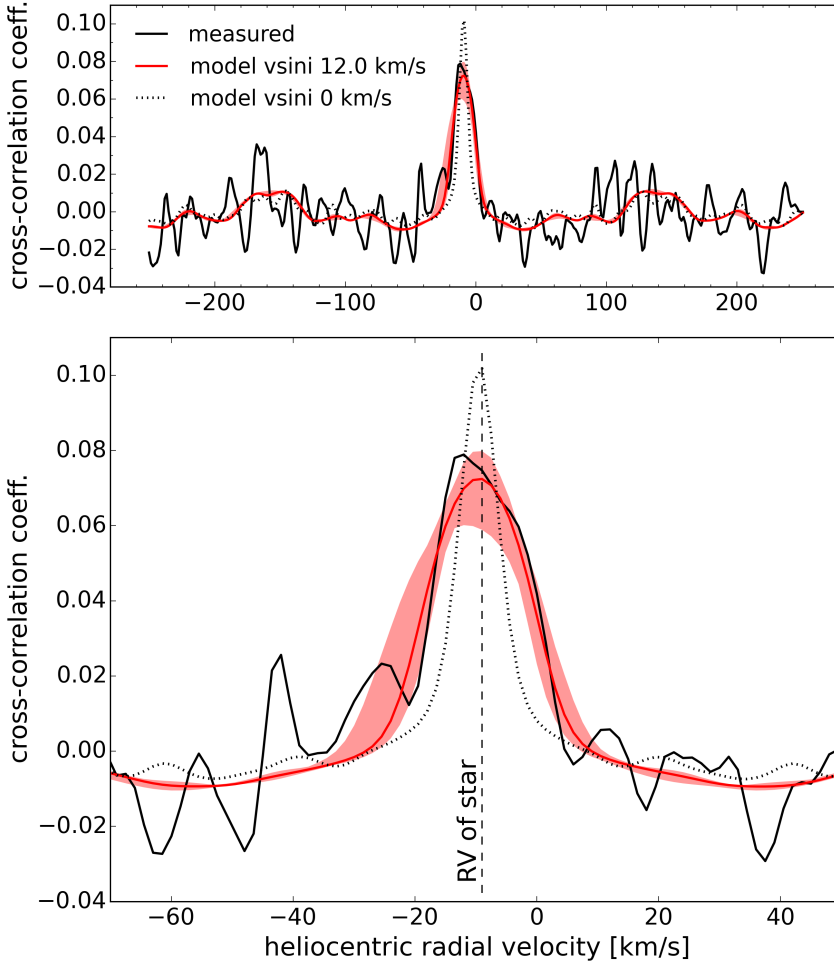
Figure 5.6: The measured cross-correlation function (CCF) from the unbroadened CO model and the observed companion spectrum (solid black line). The CO signal is centered roughly on the radial velocity of the host star ($-9 \, \mathrm{km \, s^{-1}}$), and the best fit model CCF (solid red line) has a rotational broadening of $12 \, \mathrm{km \, s^{-1}}$. The red shading indicates the 2σ confidence. The auto-correlation function of the unbroadened model is plotted for comparison as the dotted black line. The lower panel is an enlarged version of the central radial velocities of the upper panel.

5.7   Towards a comparative study of exoplanet spin

Only a handful of substellar companions have a measurement of their spin: Two exoplanets, and including this work, three low-mass brown dwarfs. The five objects are listed in Table 5.7 with a collection of properties which are relevant to a comparative study of their spin. Four of these objects were observed as part of the same CRIRES survey that this work is based upon. These are β Pictoris b which has a $v \sin(i)$ of $25 \, \text{km s}^{-1}$, GSC 6214-210 b with $v \sin(i) = 21.5 \, \text{km s}^{-1}$, HIP 78530 b with $v \sin(i) = 12 \, \text{km s}^{-1}$, and GQ Lupi b with $v \sin(i) = 5.3 \, \text{km s}^{-1}$. The fifth object is 2M1207 b, for which Zhou et al. (2016) measured the rotation period to be 10.7 hours from the rotational modulations in the combined lightcurve of the host star and the companion. This corresponds to an equatorial rotation velocity (v_{eq}) of $17.3 \, \text{km s}^{-1}$ when applying a radius estimate based on the planet cooling models from Burrows et al. (2001). It is important to realise that the $v \sin(i)$ measurements are lower limits of the equatorial rotation velocities, and that the inclinations are unknown, meaning that for the individual object v_{eq} could be significantly larger than the measured $v \sin(i)$. It is still meaningfull to compare the measured spins to one another, keeping in mind that the small sample size comes with some limitations.

The five objects show a wide range of spin velocities ($v \sin(i)$ or v_{eq}), ranging from $5 \, \text{km s}^{-1}$ to $25 \, \text{km s}^{-1}$. We have investigated the correlation of the spin velocities with their masses, ages and orbital semi-major axes, as well as the correlation of the specific angular momentum with the same three properties. The results are shown in the six panels of Fig. 5.7. The specific angular momentum is calculated based on the $v \sin(i)$ measurement and the estimated radii. We note that the unknown inclinations are not included in the errorbars of the specific angular momenta, which are instead dominated by the uncertainties in the radii.

The first row of Fig. 5.7 shows the spin velocity and the specific angular momentum, both as a function of mass. There is no clear trend with mass, based on these five objects. This stands in contrast to the solar system planets which have a clear trend: The more massive planets spin faster (Hughes, 2003). The spin velocities of the substellar companions are plotted together with the solar system planets in Fig. 5.8. From this we see that β Pictoris b and 2M1207 b, and possibly also GSC 6214-210 b, are roughly consistent with the Solar System trend, although they fall slightly below an extrapolation of the solar system planets. This can be explained by the young ages of the objects, as they are expected to spin up as they cool and contract, which will result in spin velocities in better agreement with the observed solar system correlation.

It is interesting that the three objects which are best matched to the Solar

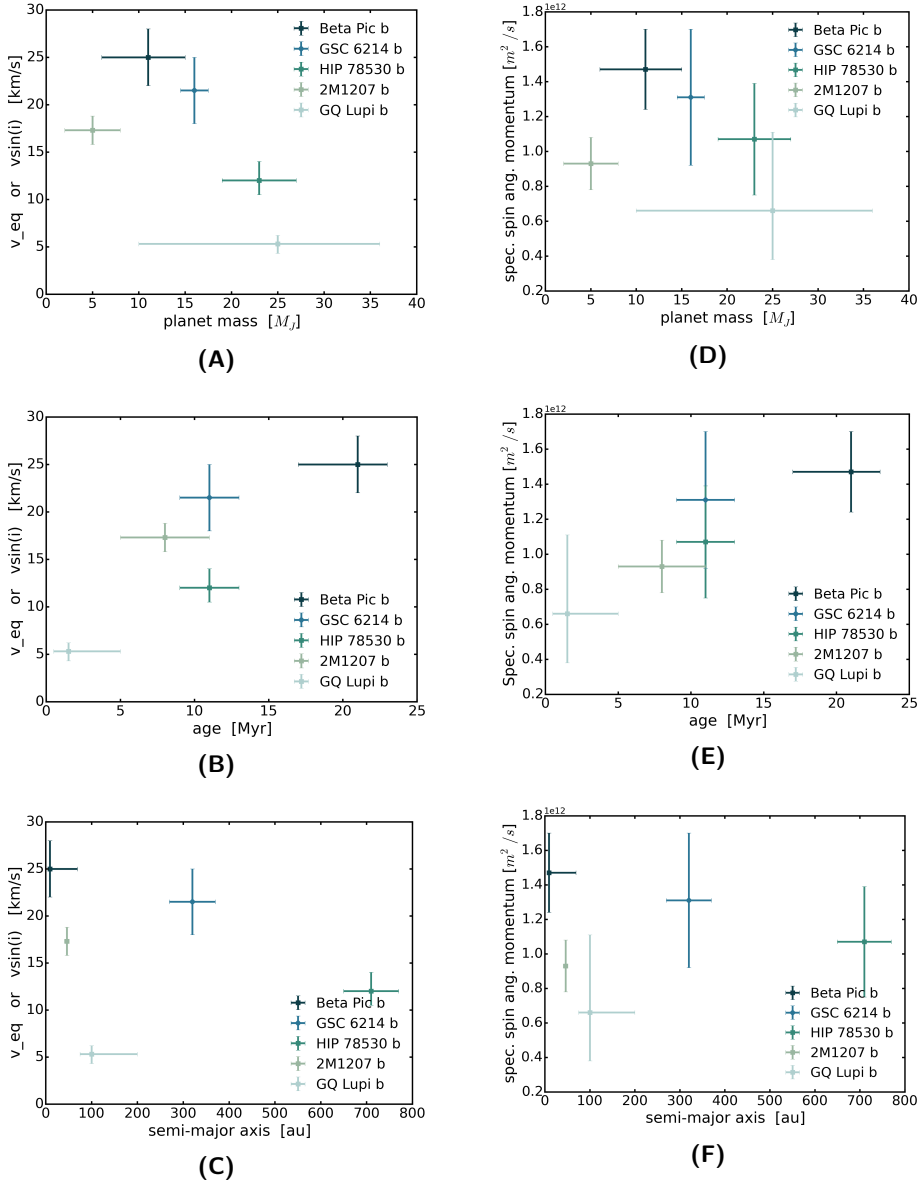**Figure 5.7:** Comparison of substellar companions with a spin measurement. The left column shows the projected rotational velocity as a function of mass, age and semi-major axis, except in the case of 2M1207 b which has an equatorial rotation velocity derived from the rotation period. The right column is the same for the specific angular momentum derived from the spin velocity and the estimated radii of the objects.

Table 5.3: Properties of substellar companions with spin measurements.

	β Pictoris b	2M1207 b	GQ Lupi b	GSC 6214 b	HIP 78530 b
spectral type	L1 $\pm$ 1.5[i]	L5[ii]	L1.5[ii]	M9 $\pm$ 0.5[iii]	M8 $\pm$ 1[iv]
mass [M$_J$]	11 $\pm$ 5[v]	5 $\pm$ 3[vi]	25^{+11}_{-15}[vii]	16 $\pm$ 1.5[iii]	23 $\pm$ 4[iv]
Teff [K]	1600^{+50}_{-25}[viii]	1230 $\pm$ 310[ix]	2650 $\pm$ 100[x]	2300 $\pm$ 200[iii]	2800 $\pm$ 200[iv]
radius [R$_J$]	1.65 $\pm$ 0.06[viii]	1.5 $\pm$ 0.1[xviii]	3.5 $\pm$ 1.5[x]	1.7 $\pm$ 0.2[xviii]	2.5 $\pm$ 0.3[xviii]
semi-major axis [au]	9^{+4}_{-3}[xi]	46 $\pm$ 5[ix]	100^{+100}_{-25}[xii]	320 $\pm$ 50[iii]	710 $\pm$ 60[iv]
age [Myr]	21 $\pm$ 4[xiii]	8 $\pm$ 3[ix]	$1.5^{+3.5}_{-1}$[xii]	11 $\pm$ 2[xiv]	11 $\pm$ 2[xiv]
$v \sin(i)$ [km s^{-1}]	25 $\pm$ 3[v]	-	$5.3^{+0.9}_{1}$[xii]	21.5 $\pm$ 3.5[xvi]	$12^{+2}_{-1.5}$[xvii]
v_{eq} [km s^{-1}]	-	17.3 $\pm$ 1.5[xv]	-	-	-

[i] Bonnefoy et al. (2014) [ii] Faherty et al. (2009) [iii] Lachapelle et al. (2015)
[iv] Lafrenière et al. (2011) [v] Snellen et al. (2014) [vi] Ducourant et al. (2008)
[vii] Ginski et al. (2014) [viii] Currie et al. (2013) [ix] Song et al. (2006) [x] Seifahrt et al. (2007)
[xi] Lecavelier des Etangs and Vidal-Madjar (2016) [xii] Schwarz et al. (2016) [xiii] Binks and Jeffries (2014)
[xiv] Pecaut et al. (2012) [xv] Zhou et al. (2016) [xvi] Schwarz et al. in prep [xvii] This work
[xviii] From planet / brown dwarf cooling models (Burrows et al., 2001), and / or luminosity and temperature.

System trend are also the ones with the lowest masses. However, the spin-evolution of planets and brown dwarfs is expected to be a complicated function of both age and mass, and in particular very young objects (age $\leqslant 100$ Myr), such as the ones in this sample. Their spin will be very sensitive to their age, due to the mass-dependent evolution of the radius as the objects cool and contract. The sensitivity to age is evident from Figures 5.7C and 5.7D: Both the spin velocity and the specific spin angular momentum correlates with age.

It is possible we are also seeing an effect with mass. GSC 6214-210 b and HIP 78530 b are both located in Upper Scorpius, which is reported to have a small instrinsic age dispersion (Preibisch and Mamajek, 2008; Pecaut et al., 2012). Therefore the two substellar companions are likely to have approximately the same age, yet they spin with different rotational velocities. Assuming that this is not a simple effect of the viewing geometry, we can speculate that HIP 78530 b rotates more slowly because it is the more massive of the two. With a mass of 23 M_J and an age of 11 Myr, HIP 78530 b is expected to be in a deuterium burning phase, which inflates the radius, temporarily preventing the brown dwarf from contracting and spinning up. We may thus be seeing the beginnings of mass-dependent evolutionary tracks. Assuming no external influences, the spin angular momentum evolution of giant planets can be divided into three phases: The first one is dominated by accretion, and this is followed by a period dominated by contraction and a rapid spin-up, and finally a quasi-stable phase when the contraction has slowed down significantly.

In the case of brown dwarfs, the situation is a little more complicated. As mentioned above the more massive brown dwarfs (< 18 M_J) will be influenced significantly by deuterium burning, which will temporarily slow the contraction. Following this deuterium burning stage the brown dwarf will rapidly contract (Burrows et al., 2001). In the final phase, the more massive brown dwarfs may also be affected by magnetic braking from winds (Reiners and Basri, 2008), so if the Solar System trend holds for old wide-orbit exoplanets and brown dwarfs, the spin versus mass relation could have a turn-off point. In Chapter 3, we speculated that GQ Lupi b is in the phase dominated by accretion, and it may therefore yet gain a significant amount of spin angular momentum. This is supported by observational evidence of ungoing accretion (Seifahrt et al., 2007; Zhou et al., 2014). GSC 6214-210 b, HIP 78530 b and possibly also 2M1207 b are more likely to be in the contraction phase. There is observational evidence for ongoing accretion on GSC 6214-210 b, but ALMA observations constrained the mass accretion rate and found it to be unlikely that the object will still gain a significant amount of mass. β Pictoris b is the oldest, and with a mass of only 11 M_J, the contraction will already have slowed significantly, although it will remain in the contraction phase for another

$\sim 100\,\mathrm{Myr}$.

In the end it is expected that all these sub-stellar objects will contract to a ra-
dius within 30% of that of Jupiter. Speculating, in the future, when we have gained
enough knowledge about the spin evolution of sub-stellar companions, it may be
possible to invert the problem and determine the ages of companions through their
spin state - although this does require knowledge of the viewing angle of the planet,
which could be obtained by combining $v\sin(i)$ measurements with photometric
monitoring to determine the rotation period. If this could be done with sufficient
accuracy, one can identify the precise stage of the early star formation process dur-
ing which the planet is formed.

The two bottom panels of Fig. 5.7 show the $v\sin(i)$ as function of orbital semi-
major axis. Although no trends are seen for these five planets, such diagrams can
in the future maybe be used to differentiate between different formation processes.
E.g. those substellar companions seen at the largest orbital distances are more likely
to have formed through gravitational instability, while those at shorter distances
through core accretion. This may, if sufficient objects are observed, show up as a
bi-modal distribution in planet spin and/or specific spin angular momentum.

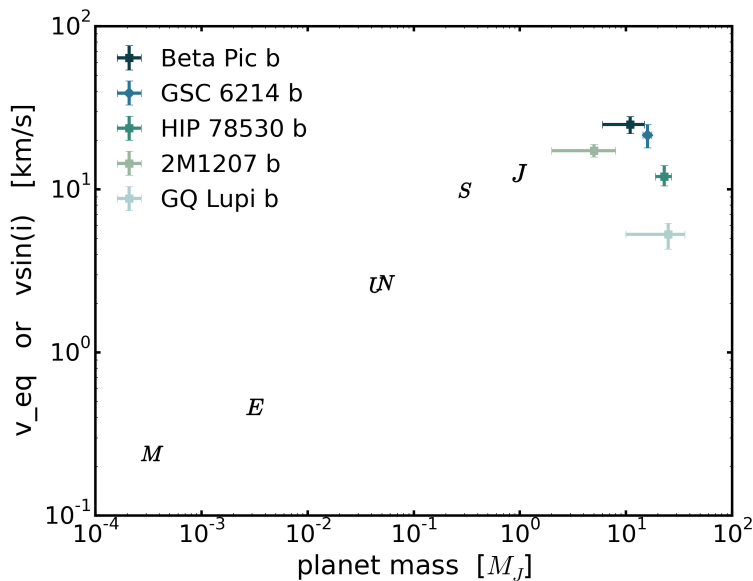
Figure 5.8: The equatorial rotation velocity (2M1207 b) or the projected rotational velocity
(the remaining 4) for the sub-stellar companions which have a measurement of one of these
quantities. For comparison, the equatorial rotation velocities of the solar system planets are
also shown, with the exception of Mercury and Venus which have spins dominated by tidal
interactions with the Sun.

5.8   Conclusions

In this chapter we described the CRIRES observations and analysis of the sub-stellar companion, HIP 78530 b, which show a projected spin velocity of $12^{+2.0}_{-1.5}$ km s^{-1} from the rotational broadening of its carbon monoxide lines. This is well within the range of the observed $v\sin(i)$ values of the other objects in the sample. Although the observed sample is small, these are the first substellar companions for wich the $v\sin(i)$ is measured (in addition to $P_{\rm rot}$ for 2M1207 b; Zhou et al., 2016). We see a correlation of spin velocity with age, which we interpret as due to the youngest objects still accreting angular momentum and their spin up through subsequent cooling and contraction. We also note that HIP 78530 b rotates slower than GSC 6214-210 which is expected to have the same age since they are both located in the Upper Scorpius group. Although this could simply be a projection effect, it could also be related to the higher mass of HIP 78530 b, implying it is currently in its deuterium burning phase - slowing its cooling and contraction and subsequent spin-up. The major upgrade of the CRIRES instrument (CRIRES+; Follert et al., 2014), which will come online in 2018, with an increase in instanta-neous wavelength coverage of an order of magnitude, will mean that in principle the $v\sin(i)$ of *all* directly imaged exoplanets can be measured. This will be funda-mental in disentangling mass, age, and possibly orbital separation effects linked to formation and evolutionary processes.

References

Arsenault, R., J. Alonso, H. Bonnet, J. Brynnel, B. Delabre, R. Donaldson, C. Dupuy, E. Fedrigo, J. Farinato, N. N. Hubin, L. Ivanescu, M. E. Kasper, J. Paufique, S. Rossi, S. Tordo, S. Stroebele, J.-L. Lizon, P. Gigan, F. Delplancke, A. Silber, M. Quattri, and R. Reiss
2003. MACAO-VLTI: An Adaptive Optics system for the ESO VLT interferometer. In *Adaptive Optical System Technologies II*, P. L. Wizinowich and D. Bonaccini, eds., volume 4839 of *Society of Photo-Optical Instrumentation Engineers (SPIE) Conference Series*, Pp. 174–185.

Bailey, V., P. M. Hinz, T. Currie, K. Y. L. Su, S. Esposito, J. M. Hill, W. F. Hoffmann, T. Jones, J. Kim, J. Leisenring, M. Meyer, R. Murray-Clay, M. J. Nelson, E. Pinna, A. Puglisi, G. Rieke, T. Rodigas, A. Skemer, M. F. Skrutskie, V. Vaitheeswaran, and J. C. Wilson
2013. A Thermal Infrared Imaging Study of Very Low Mass, Wide-separation Brown Dwarf Companions to Upper Scorpius Stars: Constraining Circumstellar Environments. *ApJ*, 767:31.

Baraffe, I., G. Chabrier, F. Allard, and P. H. Hauschildt
1998. Evolutionary models for solar metallicity low-mass stars: mass-magnitude relationships and color-magnitude diagrams. *A&A*, 337:403–412.

Baraffe, I., G. Chabrier, F. Allard, and P. H. Hauschildt
2002. Evolutionary models for low-mass stars and brown dwarfs: Uncertainties and limits at very young ages. *A&A*, 382:563–572.

Binks, A. S. and R. D. Jeffries
2014. A lithium depletion boundary age of 21 Myr for the Beta Pictoris moving group. *MNRAS*, 438:L11–L15.

Bonnefoy, M., G.-D. Marleau, R. Galicher, H. Beust, A.-M. Lagrange, J.-L. Baudino, G. Chauvin, S. Borgniet, N. Meunier, J. Rameau, A. Boccaletti, A. Cumming, C. Helling, D. Homeier, F. Allard, and P. Delorme
2014. Physical and orbital properties of β Pictoris b. *A&A*, 567:L9.

Burrows, A., W. B. Hubbard, J. I. Lunine, and J. Liebert
2001. The theory of brown dwarfs and extrasolar giant planets. *Reviews of Modern Physics*, 73:719–765.

Burrows, A., M. Marley, W. B. Hubbard, J. I. Lunine, T. Guillot, D. Saumon, R. Freedman, D. Sudarsky, and C. Sharp
1997. A Nongray Theory of Extrasolar Giant Planets and Brown Dwarfs. *ApJ*, 491:856–875.

Currie, T., A. Burrows, N. Madhusudhan, M. Fukagawa, J. H. Girard, R. Dawson, R. Murray-Clay, S. Kenyon, M. Kuchner, S. Matsumura, R. Jayawardhana, J. Chambers, and B. Bromley
2013. A Combined Very Large Telescope and Gemini Study of the Atmosphere of the Directly Imaged Planet, β Pictoris b. *ApJ*, 776:15.

D'Antona, F. and I. Mazzitelli
1997. Evolution of low mass stars. *Mem. Soc. Astron. Italiana*, 68:807.

Ducourant, C., R. Teixeira, G. Chauvin, G. Daigne, J.-F. Le Campion, I. Song, and B. Zuckerman
2008. An accurate distance to 2M1207Ab. *A&A*, 477:L1–L4.

Faherty, J. K., A. J. Burgasser, K. L. Cruz, M. M. Shara, F. M. Walter, and C. R. Gelino
2009. The Brown Dwarf Kinematics Project I. Proper Motions and Tangential Velocities for a Large Sample of Late-Type M, L, and T Dwarfs. *AJ*, 137:1–18.

Follert, R., R. J. Dorn, E. Oliva, J. L. Lizon, A. Hatzes, N. Piskunov, A. Reiners, U. Seemann, E. Stempels, U. Heiter, T. Marquart, M. Lockhart, G. Anglada-Escude, T. Löwinger, D. Baade, J. Grunhut, P. Bristow, B. Klein, Y. Jung, D. J. Ives, F. Kerber, E. Pozna, J. Paufique, H. U. Kaeufl, L. Origlia, E. Valenti, D. Gojak, M. Hilker, L. Pasquini, A. Smette, and J. Smoker
2014. CRIRES+: a cross-dispersed high-resolution infrared spectrograph for the ESO VLT. In *Ground-based and Airborne Instrumentation for Astronomy V*, volume 9147 of *Proc. SPIE*, P. 914719.

Ginski, C., T. O. B. Schmidt, M. Mugrauer, R. Neuhäuser, N. Vogt, R. Errmann, and A. Berndt
2014. Astrometric follow-up observations of directly imaged sub-stellar companions to young stars and brown dwarfs. *MNRAS*, 444:2280–2302.

Gontcharov, G. A.
2006. Pulkovo Compilation of Radial Velocities for 35 495 Hipparcos stars in a common system. *Astronomy Letters*, 32:759–771.

Horne, K.
1986. An optimal extraction algorithm for CCD spectroscopy. *PASP*, 98:609–617.

Houk, N. and M. Smith-Moore
1988. *Michigan Catalogue of Two-dimensional Spectral Types for the HD Stars. Volume 4, Declinations –26.0 to –12.0.*

Hughes, D. W.
2003. Planetary spin. *Planet. Space Sci.*, 51:517–523.

Kaeufl, H.-U., P. Ballester, P. Biereichel, B. Delabre, R. Donaldson, R. Dorn, E. Fedrigo, G. Finger, G. Fischer, F. Franza, D. Gojak, G. Huster, Y. Jung, J.-L. Lizon, L. Mehrgan, M. Meyer, A. Moorwood, J.-F. Pirard, J. Paufique, E. Pozna, R. Siebenmorgen, A. Silber, J. Stegmeier, and S. Wegerer
2004. CRIRES: a high-resolution infrared spectrograph for ESO's VLT. In *Ground-based Instrumentation for Astronomy*, A. F. M. Moorwood and M. Iye, eds., volume 5492 of *Society of Photo-Optical Instrumentation Engineers (SPIE) Conference Series*, Pp. 1218–1227.

Kouwenhoven, M. B. N., A. G. A. Brown, S. F. Portegies Zwart, and L. Kaper
2007. The primordial binary population. II.. Recovering the binary population for intermediate mass stars in Scorpius OB2. *A&A*, 474:77–104.

Kouwenhoven, M. B. N., A. G. A. Brown, H. Zinnecker, L. Kaper, and S. F. Portegies Zwart
2005. The primordial binary population. I. A near-infrared adaptive optics search for close visual companions to A star members of Scorpius OB2. *A&A*, 430:137–154.

Lachapelle, F.-R., D. Lafrenière, J. Gagné, R. Jayawardhana, M. Janson, C. Helling, and S. Witte
2015. Characterization of Low-mass, Wide-separation Substellar Companions to Stars in Upper Scorpius: Near-infrared Photometry and Spectroscopy. *ApJ*, 802:61.

Lafrenière, D., R. Jayawardhana, M. Janson, C. Helling, S. Witte, and P. Hauschildt
2011. Discovery of an $\sim 23\ \mathrm{M}_{Jup}$ Brown Dwarf Orbiting ~ 700 AU from the Massive Star HIP 78530 in Upper Scorpius. *ApJ*, 730:42.

Lecavelier des Etangs, A. and A. Vidal-Madjar
2016. The orbit of beta Pictoris b as a transiting planet. *A&A*, 588:A60.

Pecaut, M. J., E. E. Mamajek, and E. J. Bubar
  2012. A Revised Age for Upper Scorpius and the Star Formation History among the F-type Members of the Scorpius-Centaurus OB Association. *ApJ*, 746:154.

Preibisch, T., A. G. A. Brown, T. Bridges, E. Guenther, and H. Zinnecker
  2002. Exploring the Full Stellar Population of the Upper Scorpius OB Association. *AJ*, 124:404–416.

Preibisch, T. and E. Mamajek
  2008. *The Nearest OB Association: Scorpius-Centaurus (Sco OB2)*, P. 235.

Reiners, A. and G. Basri
  2008. Chromospheric Activity, Rotation, and Rotational Braking in M and L Dwarfs. *ApJ*, 684:1390–1403.

Schwarz, H., C. Ginski, R. J. de Kok, I. A. G. Snellen, M. Brogi, and J. L. Birkby
  2016. The slow spin of the young substellar companion GQ Lupi b and its orbital configuration. *A&A*, 593:A74.

Seifahrt, A., R. Neuhäuser, and P. H. Hauschildt
  2007. Near-infrared integral-field spectroscopy of the companion to GQ Lupi. *A&A*, 463:309–313.

Sherry, W. H., F. M. Walter, and S. J. Wolk
  2004. Photometric Identification of the Low-Mass Population of Orion OB1b. I. The σ Orionis Cluster. *AJ*, 128:2316–2330.

Snellen, I., R. de Kok, J. L. Birkby, B. Brandl, M. Brogi, C. Keller, M. Kenworthy, H. Schwarz, and R. Stuik
  2015. Combining high-dispersion spectroscopy with high contrast imaging: Probing rocky planets around our nearest neighbors. *A&A*, 576:A59.

Snellen, I. A. G., B. R. Brandl, R. J. de Kok, M. Brogi, J. Birkby, and H. Schwarz
  2014. Fast spin of the young extrasolar planet β Pictoris b. *Nature*, 509:63–65.

Song, I., G. Schneider, B. Zuckerman, J. Farihi, E. E. Becklin, M. S. Bessell, P. Lowrance, and B. A. Macintosh
  2006. HST NICMOS Imaging of the Planetary-mass Companion to the Young Brown Dwarf 2MASSW J1207334-393254. *ApJ*, 652:724–729.

van Leeuwen, F.
  2007. Validation of the new Hipparcos reduction. *A&A*, 474:653–664.

Zhou, Y., D. Apai, G. H. Schneider, M. S. Marley, and A. P. Showman
    2016. Discovery of Rotational Modulations in the Planetary-mass Companion
    2M1207b: Intermediate Rotation Period and Heterogeneous Clouds in a Low
    Gravity Atmosphere. *ApJ*, 818:176.

Zhou, Y., G. J. Herczeg, A. L. Kraus, S. Metchev, and K. L. Cruz
    2014. Accretion onto Planetary Mass Companions of Low-mass Young Stars.
    ApJ, 783:L17.

Samenvatting

Iets minder dan twintig jaar geleden werd de eerste planeet in een baan rond een andere ster dan onze eigen zon ontdekt. Het bestaan van zulke vreemde werelden werd lang aangenomen, maar we hadden geen idee dat het in de melkweg bruist van de planetenstelsels. Ze worden exoplaneten genoemd, een afkorting van extrasolaire planeten, om aan te geven dat ze zich buiten het zonnestelsel bevinden. In de jaren sinds die eerste ontdekking zijn duizenden exoplaneten gevonden door middel van een aantal verschillende waarneemtechnieken, en nieuwe methoden zijn ontwikkeld om hun banen, samenstellingen en atmosferen te onderzoeken.

De studie van exoplaneten is een zoektocht om onze plaats in het heelal te begrijpen. Hoe uniek is het zonnestelsel? Hoe buitengewoon is de Aarde? Is leven op Aarde een ondoorgrondelijk toeval, of wemelt het van het leven in de melkweg? Een van de grootste verassingen tot dusver is de verbazingwekkende verscheidenheid ind samenstellingen en banen van de ontdekte exoplaneten geweest. Er zijn planeten die in een Aardse dag een baan om hun ster voltooien, en anderen die er juist duizenden Aardse jaren over doen om een enkele baan te voltooien. Hoewel sommige systemen meerdere planeten of zelfs meerdere sterren hebben, bestaan anderen naar ons beste weten uit een enkele ster en planeet. De diversiteit aan exoplaneten vormt een uitdaging voor de onstaanstheorieën die ontwikkeld zijn voor het zonnestelsel, en elke moderne theorie moet streven naar een verklaring voor de gehele waargenomen variëteit aan planetenstelsels.

Dit proefschrift behandelt twee verschillende typen gasreus-exoplaneten, die twee tegenovergestelde uitersten in baantype vertegenwoordigen: hete Jupiters en jonge gasreuzen in wijde omloopbanen. Een hete Jupiter is een gasreus met een massa vergelijkbaar met die van Jupiter, maar met een omlooptijd van minder dan vijf dagen. De nabijheid tot de ster leidt tot zeer hoge temperaturen, en veel van deze planeten blijken een veel grotere straal te hebben dan die van Jupiter, ondanks de vergelijkbare massas. De wijdebaan gasreuzen daarentegen bevinden zich over het algemeen op een afstand van hun ster van tientallen tot honderden keren de afstand van de Aarde tot de Zon. Deze exoplaneten zijn ontdekt met directe waar-

nemingen, wat inhoudt dat de ster en de planeet als twee verschillende objecten te zien zijn in astronomische waarnemingen. Dit is mogelijk vanwege de wijde baan, en zelfs dan nog alleen als de gasreus extreem heet is. De afstand tot de ster is te groot om de planeetatmosfeer significant op te warmen, maar als het stelsel jong is - tot een paar honderd miljoen jaar - zal de planeet nog zijn ontstaanswarmte hebben. Hoewel momenteel alleen jonge exoplaneten direct waargenomen kunnen worden, biedt dit ook een unieke mogelijkheid om planeten in de vroegste stadia van hun leven te bestuderen.

Het bestuderen van exoplaneet-atmosferen

Afhankelijk van hoe een exoplaneet is ontdekt kunnen sommige van de fundamentele fysieke eigenschappen, zoals de massa en straal, direct vanuit de detectie worden geschat. Echter, detectie is slechts de eerste stap in het begrijpen van de fysieke eigenschappen van een exoplaneet. Het karakteriseren van de planeet-atmosfeer volgt daarop. Dit kan de chemische samenstelling van de atmosfeer aantonen, en, zoals dit proefschrift laat zien, de temperatuur en de rotatie van de planeet. Uiteindelijk willen we bewijs vinden voor biologische activiteit door de detectie van biosignatuurgassen in de atmosfeer - zoals moleculair zuurstof in de atmosfeer van de Aarde.

De planeetdetectiemethodes zijn vooral indirect, wat betekent dat het licht van de ster en de planeet vermengd zijn, en de aanwezigheid van de planeet wordt afgeleid uit het licht van de ster. Voor het karakteriseren van de atmosfeer is het noodzakelijk om het licht van de planeet van dat van de ster te scheiden. Dit kan op verschillende manieren gedaan worden. De meest succesvolle methoden tot dusver worden toegepast bij exoplaneten met planeetovergangen. Dit zijn exoplaneten waarbij de baan bij toeval zodanig georiënteerd is dat de planeet vanaf de Aarde gezien voor de ster langs beweegt. De methodes zijn gebaseerd op hoe de bijdrage van de planeet aan het waargenomen licht (ster + planeet) periodiek verandert. De planeet verdwijnt achter de ster, komt weer tevoorschijn waarbij vanaf de Aarde gezien geleidelijk de bijdrage van de dag- en nachtkant verandert, en wanneer dan de planeetovergang voor de ster plaatsvindt wordt een deel van het sterlicht gefilterd door de planeetatmosfeer, waarbij het een soort vingerafdruk achterlaat in het waargenomen licht. In het geval van de direct waargenomen planeten met wijde baan kan het licht van de planeet direct in andere pixels dan die van de ster worden gescheiden, hoewel er onvermijdelijk verstrooid sterlicht op de positie van de planeet terecht zal komen. In dit proef schrift combineer ik de bovenstaande methoden met infraroodspectroscopie met hoge resolutie. Dit geeft een extra filtermechanisme omdat het spectrum van de ster anders is dan dat van de planeet.

De verticale temperatuurstructur van een hete Jupiter

Een belangrijk aspect van alle exoplaneetatmosferen is hoe de temperatuur verandert met de hoogte. Over het algemeen dringt de straling van de ster diep door in de atmosfeer van de planeet, waarbij het deze van onderaf verwarmt. Dit zorgt ervoor dat de temperatuur met toenemende hoogte afneemt. Echter, sterke optische- of UV-absorbeerders in de bovenlagen van de atmosfeer kunnen er voor zorgen dat in een bepaalde laag of regio in de atmosfeer de temperatuur in plaats daarvan stijgt met toenemende hoogte. De temperatuur is geïnverteerd. Zulke temperatuurinversies zijn veelvoorkomend bij de planeten in het zonne stelsel. Jupiter en de andere reuzenplaneten hebben thermische inversies die door CH_4-geïnduceerde nevel veroorzaakt worden, terwijl O_3 de inversie in de stratosfeer van de Aarde veroorzaakt.

Thermische inversies zouden ook algemeen aanwezig kunnen zijn in de atmosferen van hete Jupiters. Er zijn claims geweest van inversielagen in atmosferen van verschillende hete Jupiters, vooral gebaseerd op waarnemingen met de Spitzer ruimtetelescoop. Hoewel deze claims intrigerend zijn, is duidelijk geworden dat ze ook controversieel en vatbaar voor meerdere interpretaties zijn. In hoofdstuk 2 presenteer ik de resultaten van hoge-dispersie spectroscopische waarnemingen in het nabij-infrarood van de beroemde hete Jupiter HD 209458 b. Deze exoplaneet werd lang beschouwd als de gouden standaard voor een hete Jupiter met een thermische inversie; wij hebben echter bewijs gevonden tegen een sterke thermische inversie. Onze waarnemingen kunnen het beste uitgelegd worden met een temperatuur die nauwelijks verandert met de hoogte.

Een eerste studie van de rotatie van exoplaneten

De Aarde draait om zijn eigen as, en dit bepaalt de lengte van dag en nacht. De rotatie beïnvloedt het klimaat, de atmosfeerdynamica en het magnetisch veld van een planeet. Daarom is het kunnen meten van de rotatieperiode van exoplaneten van groot belang. Tevens kan het licht werpen op het vormingsproces en de evolutie.

Twee vormingsprocessen worden vooral beschouwd voor reuzeplaneten: i) kernaccretie en ii) schijffragmentatie. Van Jupiter en Saturnus wordt algemeen aangenomen dat ze door kernaccretie zijn gevormd. In dit type vormingsmodellen valt gas in op vaste planeetembryos van enkele tot tien Aardmassas die op een afstand van vergelijkbaar met die van Jupiter zijn ontstaan. De ontdekking van extrasolaire

reuzenplaneten met extreem wijde banen heeft ertoe geleid dat de schijffragmen-
tatietheorie nieuw leven is ingeblazen, omdat het kernaccretiemodel moeite heeft
het bestaan van planeten zo ver weg van de ster te verklaren. Deze theorie stelt dat
(exo)reuzenplaneten kunnen ontstaan als een gravitatie-instabiliteit in de schijf die
op zichzelf instort in de buitenregio van de planetaire schijf. De planetaire rotatie is
vooral een gevolg van accretie van impulsmoment tijdens het ontstaan, en als kern-
accretie en gravitationele instabiliteit in verschillende impulsmomenten resulteren
is het mogelijk dat dit zichtbaar wordt in onderzoek naar de rotatie van substellaire
begeleiders als een functie van de massa of baanafstand van de ster.

Ons team heeft een kleine studie uitgevoerd met het doel om de rotatiesnelhe-
den van jonge, wijdbaanse exoplaneten te bepalen. De waarnemingen combineren
hoge-resolutie spectroscopie met hoog-contrast waarnemingen, en deze baanbre-
kende techniek heeft geleid tot de eerste metingen van de rotatie van exo-planeten.
In de praktijk meten we de geprojecteerde rotatiesnelheid. Dit betekent de com-
ponent van de rotatiesnelheid langs de zichtlijn, en de snelheden zijn dus de on-
dergrens. In hoofdstukken 3, 4 en 5 presenteer ik de resultaten van drie individuele
objecten, en in hoofdstuk 5 bestudeer ik ook de hele steekproef. Ik onderzoek de
rotatie als een functie van de massa, baanafstand en leeftijd. Hoewel de bestudeer-
de steekproef klein is zien we wel een correlatie tussen de rotatiesnelheid en de
leeftijd, die we interpreteren als gevolg van het nog steeds accreteren van materiaal
en impulsmoment door de jongste objecten, en de als gevolg van daaropvolgende
koeling en samentrekking toenemende rotatie.

Summary

A little more than two decades ago, the first planet orbiting a different star than our own Sun was discovered. The existence of such foreign worlds had long been assumed, but little did we know that the Galaxy is, in fact, brimming with planetary systems. They are called exoplanets, which is short for extrasolar planets, to highlight that they are located outside of the Solar System. In the years since that first discovery, thousands of exoplanets have been discovered using several different observational techniques, and new methods have been developed to study their orbits, their composition and their atmospheres.

The study of exoplanets is a quest to understand our place in the universe. How unique is the Solar System? How extraordinary is Earth? Is life on Earth an unfathomable coincidence, or is the Milky Way teeming with life? One of the biggest surprises so far has been the amazing variety in the composition and orbits of the discovered exoplanets. There are planets orbiting their stars in the span of a single day on Earth, and yet others take thousands of Earth-years to complete a single orbit. While some systems have multiple planets or even multiple stars, others consist to the best of our knowledge of a single star and planet. The diversity of exoplanets presents a challenge to the theories of formation designed to match the Solar System, and any modern theories must strive to explain the full observed range of architectures of planetary systems.

This thesis deals with two different types of gas-giant exoplanets, representing the opposite extremes in terms of the orbits: Hot Jupiters and young, wide-orbit gas giants. A hot Jupiter is a gas giant with a mass similar to that of Jupiter, but it has an orbital period of fewer than five days. The proximity to the star leads to soaring temperatures, and many of these planets have been found to have much larger radii than Jupiter in spite of the similar masses. The wide-orbit gas giants, on the other hand, typically have distances to their star that are tens or hundreds of times further than the distance between Sun and Earth. These exoplanets have been detected with direct imaging, meaning the star and the planet appear as two separate objects in astronomical images. This is possible because of the wide orbit,

and yet, only if the gas giant is extremely hot. The distance from the star is too large to heat the planet atmosphere significantly, but if the system is young - up to a couple of hundred million years - the planet will still be hot from the formation. Although direct imaging is currently limited to young exoplanets, this also provides a unique opportunity to study planets at the earliest stages of their lives.

Observing exoplanet atmospheres

Depending on how an exoplanet is discovered, some of the basic physical properties, such as the mass and radius, can be estimated directly from the detection. However, detection is only the first step in understanding the physical properties of an exoplanet. The characterisation of its atmosphere is the next. It can reveal the chemical composition of the atmosphere, and as is shown in this thesis, the temperature structure and the rotation of the planet. Ultimately, we want to find evidence for biological activity through the detection of biomarker gases in the atmosphere – such as molecular oxygen in the atmosphere of Earth.

The planet detection methods are mostly indirect, meaning that the light from the star and the planet are mingled, and the presence of the planet is inferred from the light of the star. For atmospheric characterisation, it is necessary to separate the planet light from that of the star. This can be done in several ways. The most successful methods so far are applied to transiting exoplanets. These are exoplanets where the orbit by chance is oriented such that the planet passes in front of the star as seen from Earth. The methods are based on how the contribution from the planet to the observed light (star+planet) changes periodically. The planet disappears behind the star, emerges again, gradually changing the amounts of day-side and night-side as viewed from Earth, and then when the planet transits in front of the star, a part of the stellar light is filtered through the planetary atmosphere, leaving a sort of fingerprint in the observed light. In the case of the directly imaged, wide-orbit exoplanets, the light from the planet can be separated directly to different pixels than those of the star, although starlight will inevitably scatter to the position of the planet as well. In this thesis, I combine the methods mentioned above with high-resolution infra-red spectroscopy. This provides an additional filtering mechanism because the spectrum of the star is different from that of the planet.

The vertical temperature structure of a hot Jupiter

An important aspect of any exoplanet atmosphere is how the temperature changes with altitude. Generally, the radiation from the star penetrates deeply into the

atmosphere of the planet, heating it from below. This causes the temperature to drop with increasing altitude. However, strong optical or UV absorbers in the upper layers of the atmosphere can result in a layer or region in the atmosphere where the temperature instead *increases* with altitude. The temperature is *inverted*. Such temperature inversions are common among Solar System planets. Jupiter, along with the other giant planets, has thermal inversions caused by CH_4-induced hazes, while O_3 causes the inversion in Earth's stratosphere.

Thermal inversions may be commonly present in hot Jupiter atmospheres as well. There have been claims of inversion layers in several hot Jupiter atmospheres, mostly based on observations with the Spitzer Space Telescope. While these claims are intriguing, they have also proven controversial and prone to degeneracies. In Chapter 2, I present the results from high-dispersion near-infrared spectroscopic observations of the famous hot Jupiter, HD 209458 b. This exoplanet was long considered the gold standard for a hot Jupiter with a thermal inversion; however, we found evidence *against* a strong thermal inversion. Our observations are best explained by a temperature which hardly changes with altitude.

A first survey of the rotation of exoplanets

The Earth rotates around its own axis and this determines the length of night and day. The rotation influences the climate, the atmospheric dynamics, and the magnetic field of a planet. Therefore, the ability to measure the rotation period for exoplanets is of great importance. Besides, it may shed light on the formation process and evolution.

Two formation processes are typically considered for giant planets: i) core accretion and ii) disk fragmentation. Jupiter and Saturn are commonly accepted to have formed through core accretion. In this class of formation models, gas accretes onto solid planetary embryos of several to ten Earth masses that may have formed at distances comparable to that of Jupiter. The discovery of extrasolar giant planets with extremely wide orbits led to the reinvigoration of the disk fragmentation hypothesis because the core accretion scenario struggles to explain the existence of planets so far from the star. This theory states that giant (exo)planets may form as a disk gravitational instability that collapses on itself in the outer protoplanetary disk. Planetary rotation is predominantly a result of accretion of angular momentum during the formation, and if core accretion and gravitational instability result in differences in spin angular momentum, it is possible this will show up in studies of the rotation of substellar companions as a function of mass or orbital distance from the star.

Our team has performed a small survey aimed to determine the rotation ve-

locities of young, wide-orbit exoplanets. The observations combine high-resolution spectroscopy with high-contrast imaging, and this ground-breaking technique has resulted in the first measurements of the rotation of exoplanets. In practice, what we measure is the *projected* rotational velocity. This means the component of the rotation velocity along the line-of-sight, and the velocities are as such minimum values. In Chapters 3, 4, and 5, I present the results from three individual objects, and in Chapter 5 I also study the rotation of the sample as a whole. I investigate the rotation as a function of mass, orbital distance and age. Although the observed sample is small, we do see a correlation of rotation velocity with age, which we interpret as due to the youngest objects still accreting material and angular momentum and their spin up through subsequent cooling and contraction.

Curriculum Vitae

I was born on June 11, 1986, in Hørsholm, Denmark. I was always fascinated by the night sky, but it was an astronomy course at Espergærde Gymnasium during my pre-university education that sparked the fire. Still, I was reluctant to choose astronomy as a career path. It was not before I experienced the night sky in its full, dark glory in the Australian outback that I realised that I had no choice but to follow my heart and study the Universe.

I enrolled in the Physics program at Copenhagen University in 2006 and obtained a Bachelor of Science degree in astronomy in 2010. My studies continued at Lund University where I completed a Master of Science degree in astrophysics in 2012. My master's thesis was about the photometric characterisation of a newly built Earthshine Telescope on Mauna Loa, Hawaii. The research project was a collaboration between the instrument department at Lund Observatory and the Danish Meteorological Institute (DMI), and I was supervised by Torben Andersen from Lund Observatory, and Peter Thejll and Hans Gleisner from DMI.

I accepted a PhD position at Leiden University, beginning September 2012, under the supervision of Prof.dr. Ignas Snellen. It was his work on characterising exoplanet atmospheres with high-dispersion spectroscopy which inspired me to aim for a career studying exoplanets. The original focus of my research was on hot Jupiter atmospheres, but gradually I shifted towards directly imaged planets, with a special interest in their formation and dynamical evolution. I developed a method for measuring the rotational velocity and the radial velocity of these planets and I set up a framework for how such measurements can be used to infer clues about the formation and early history of wide-orbit giant planets.

In 2016, I was awarded a Morrison Fellowship at the University of California Santa Cruz. I moved to California to begin my new Postdoc life in January 2017.

List of publications

Peer-reviewed publications

- *A framework to combine low- and high-resolution Spectroscopy for the Atmospheres of Transiting Exoplanets*
  Brogi, M., Line, M., Bean, J., Desert, J.-M. & **Schwarz, H.**
  ApJ, 839, L2 (2017)

- *Discovery of water at high spectral resolution in the atmosphere of 51 Peg b*
  Birkby, J. L., de Kok, R. J., Brogi, M., **Schwarz, H** & Snellen, I. A. G.
  AJ 153, 138 (2017)

- *The slow spin of the young sub-stellar companion GQ Lupi b and its orbital configuration*
  Schwarz, H., Ginski, C., de Kok, R. J., Snellen, I. A. G., Brogi, M. & Birkby, J.L.
  A&A 593, A74 (2016)

- *Rotation and winds of exoplanet HD 189733 b measured with high-dispersion transmission spectroscopy*
  Brogi, M., de Kok, R. J., Albrecht, S., Snellen, I. A. G., Birkby, J. L. & **Schwarz, H.** ApJ 817, 106 (2016)

- *Evidence against a strong thermal inversion in HD 209458 b from high-dispersion spectroscopy*
  Schwarz, H., Brogi, M., de Kok, R. J., Birkby, J. L. & Snellen, I. A. G
  A&A 576, A111 (2015)

- *Combining high-dispersion spectroscopy (HDS) with high contrast imaging (HCI): Probing rocky planets around our nearest neighbors*
  Snellen, I. A. G., de Kok, R. J., Birkby, J. L., Brandl, B., Brogi, M., Keller, C., Kenworthy, M., **Schwarz, H.** & Stuik, R.
  A&A 576, A59 (2015)

- *A search for TiO in the optical high-resolution transmission spectrum of HD 209458b: Hindrance due to inaccuracies in the line database*
  Hoeijmakers, H. J, de Kok, R. J., Snellen, I. A. G., Brogi, M., Birkby, J. L. & **Schwarz, H.**
  A&A 575, A20 (2015)

- *Fast spin of the young extrasolar planet beta Pictoris b*
  Snellen, I. A. G., Brandl, B., de Kok, R. J., Brogi, M., Birkby, J. L. & **Schwarz, H.**
  Nature 509, 63-65 (2014)

- *Carbon monoxide and water vapor in the atmosphere of the non-transiting exoplanet HD 179949 b*
  Brogi, M., de Kok, R. J., Birkby, J. L., **Schwarz, H.** & Snellen, I. A. G.
  A&A 565, A124 (2014)

- *Identifying new opportunities for exoplanet characterisation at high spectral resolution*
  de Kok, R. J., Birkby, J. L., Brogi, M., **Schwarz, H.**, Albrecht, S., de Mooij, E. J. W. & Snellen, I. A. G.
  A&A 561, A150 (2014)

- *The colour of the dark side of the Moon*
  Thejll, P., Flynn, C., Gleisner, H., Andersen, T., Ulla, A., O-Petersen, M., Darudi, A. & **Schwarz, H.**
  A&A 563, A38 (2014)

- *Detection of water absorption in the day side atmosphere of HD 189733 b using ground-based high-resolution spectroscopy at 3.2 micron*
  Birkby, J. L., de Kok, R. J., Brogi, M., de Mooij, E. J. W., **Schwarz, H.**, Albrecht, S. & Snellen, I. A. G.
  MNRAS 436, L35 (2013)

Conference proceedings

- *Molecules on the night-side of a non-transiting Hot Jupiter*
  de Kok, R. J., Brogi, M., Birkby, J. L., **Schwarz, H.** & Snellen, I. A. G.
  ESS 3, 111.16 (2015)

- *Measuring the spin of the directly imaged sub-stellar companion GQ Lupi b*
  Schwarz, H., Brogi, M., de Kok, R. J., Birkby, J. L. & Snellen, I. A. G.
  ESS 3, 104.14 (2015)

- *Detecting water at high spectral resolution in hot Jupiter atmospheres*
  Birkby, J., Snellen, I., de Kok, R., Brogi, M., **Schwarz, H.**, Albrecht, S. &
  de Mooij, E.
  AAS 223, 230.04 (2014)

- *Exploring the atmosphere of HD 189733b at high spectral resolution*
  de Kok, R., Birkby, J., Brogi, M., Snellen, I., Albrecht, S., de Mooij, E. &
  Schwarz, H.
  DPS 45, 105.02 (2013)

- *Probing hot Jupiter atmospheres with ground-based high-resolution spectroscopy*
  Schwarz, H., Brogi, M., Birkby, J. L., de Kok, R. J., Snellen, I. A. G.,
  de Mooij, E. J. W. & Albrecht, S.
  EPSC 8, 44 (2013)

- *First results from new Earthshine telescope on Mauna Loa*
  Thejll, P., Flynn, C., **Schwarz, H.**, Gleisner, H., Owner-Petersen, M., Darudi, A.
  & Andersen, T.
  EGUGA 14, 4975 (2012)

Other publications

- *Characterising exoplanet atmospheres with high-resolution spectroscopy*
  Birkby, J., de Kok, R., Brogi, M., **Schwarz, H.**, Albrecht, S., de Mooij, E.
  & Snellen, I.
  Msngr 154, 57 (2013)

Acknowledgements

This thesis was made possible through the friendship, guidance and support from many different people, and not every deserving soul has made it onto this page. You have my thanks, all the same.

I am grateful to my uncle Regnar, who used to take me to the Tycho Brahe Planetarium when I was a child, and to Mogens Nørgaard Olesen, my inspiring high-school astronomy teacher. Both played a key role in helping me find my path.

During my years at the Sterrewacht, I was fortunate to be in a vibrant research group, and I have learned much from my PhD partners in crime, Matteo, Emanuele, Jens, Andrew, Geert-Jan & Sebastiaan: 'Thank you for the group meetings, the journal clubs and the things inbetween.' A special thank you goes to Jayne: 'You always went above and beyond, guiding me through the academic jungle'.

To the computer help desk: 'Only now that I am without you, do I fully appreciate your brilliance and speedy response times.' To Evelijn Gerstel: 'Your support in financial matters was of great value to me.' To Xander Tielens: 'Thank you for your guidance and words of wisdom.'

To the friends I met in Leiden: 'Every single one of you belong on this list, and I thank you for the fun times full of laughter, the lunch breaks, and the educational moments that occasionally crept in.' To my physics friends, Brian & Tom: 'Thanks for the shared beers and your willingness to always listen.' To my Danish astronomy-friends, Eva, Ann-Sofie & Eistrup: 'Thanks for being my Danish venting system - and for everything else.' To Leah: 'Thanks for the home-cooked meals and excellent company.' To Steven: 'Thanks for our many conversations and for translating the summary of this thesis to Dutch in record time'. To Jeroen, Marijke & Mason: 'Thanks for our amazing solar eclipse journey to the Faroe Islands.' To Ricardo: 'Thanks for the hug and the chocolates on a day when that what exactly what I needed.' To David: 'Thanks for so often understanding exactly how I felt." — All of you kept me afloat.

Finally, to my family: 'Jeres kærlighed og støtte har bragt mig hertil, og jeg er jer evigt taknemmelig.